

## **INFORMATION TO USERS**

This manuscript has been reproduced from the microfilm master. UMI films the text directly from the original or copy submitted. Thus, some thesis and dissertation copies are in typewriter face, while others may be from any type of computer printer.

**The quality of this reproduction is dependent upon the quality of the copy submitted.** Broken or indistinct print, colored or poor quality illustrations and photographs, print bleedthrough, substandard margins, and improper alignment can adversely affect reproduction.

In the unlikely event that the author did not send UMI a complete manuscript and there are missing pages, these will be noted. Also, if unauthorized copyright material had to be removed, a note will indicate the deletion.

Oversize materials (e.g., maps, drawings, charts) are reproduced by sectioning the original, beginning at the upper left-hand corner and continuing from left to right in equal sections with small overlaps.

Photographs included in the original manuscript have been reproduced xerographically in this copy. Higher quality 6" x 9" black and white photographic prints are available for any photographs or illustrations appearing in this copy for an additional charge. Contact UMI directly to order.

ProQuest Information and Learning  
300 North Zeeb Road, Ann Arbor, MI 48106-1346 USA  
800-521-0600

**UMI<sup>®</sup>**



**Quantifying Single Oil-Particle Interactions in Aqueous Media**

by

**David Eric Aston**

**A dissertation submitted in partial fulfillment of the  
requirements for the degree of**

**Doctor of Philosophy**

**University of Washington**

**2001**

**Program Authorized to Offer Degree: Department of Chemical Engineering**

UMI Number: 3013925

Copyright 2001 by  
Aston, David Eric

All rights reserved.

UMI<sup>®</sup>

---

UMI Microform 3013925

Copyright 2001 by Bell & Howell Information and Learning Company.  
All rights reserved. This microform edition is protected against  
unauthorized copying under Title 17, United States Code.

---

Bell & Howell Information and Learning Company  
300 North Zeeb Road  
P.O. Box 1346  
Ann Arbor, MI 48106-1346

**©Copyright 2001**

**David Eric Aston**

In presenting this dissertation in partial fulfillment of the requirements for the Doctoral degree at the University of Washington, I agree that the Library shall make its copies freely available for inspection. I further agree that extensive copying of the dissertation is allowable only for scholarly purposes, consistent with "fair use" as prescribed in the U.S. Copyright Law. Requests for copying or reproduction of this dissertation may be referred to Bell and Howell Information and Learning, 300 North Zeeb Road, P.O. Box 1346, Ann Arbor, MI 48106-1346, to whom the author has granted "the right to reproduce and sell (a) copies of the manuscript in microform and/or (b) printed copies of the manuscript made from microform."

Signature *Eui Cho*

Date 18 May 2001

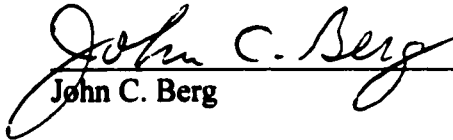
University of Washington  
Graduate School

This is to certify that I have examined this copy of a doctoral dissertation by

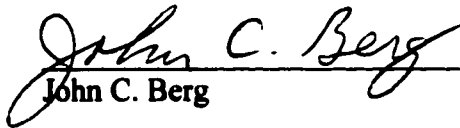
David Eric Aston

and have found that it is complete and satisfactory in all respects,  
and that any and all revisions required by the final  
examining committee have been made.

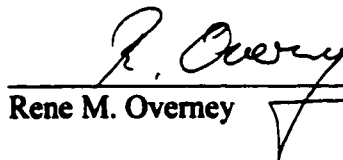
Chair of Supervisory Committee:

  
\_\_\_\_\_  
John C. Berg

Reading Committee:

  
\_\_\_\_\_  
John C. Berg

  
\_\_\_\_\_  
Samuel C. Fain

  
\_\_\_\_\_  
Rene M. Overney

Date: 18 May 2001

University of Washington

Abstract

**QUANTIFYING SINGLE OIL-PARTICLE INTERACTIONS IN AQUEOUS MEDIA**

by David Eric Aston

Chairperson of the Supervisory Committee:

Professor John C. Berg

Department of Chemical Engineering

Detailed knowledge about the single-pair interactions between a rigid micro-particle and a liquid drop or air bubble immersed in some fluid is one way to predict and/or design the ensemble behavior of mixed colloidal materials, emulsions and other hybrid dispersions, from a kind of first-principles approach. The invention of the atomic force microscope (AFM) has made it possible to accomplish the direct measurement of forces from the interaction of a colloidal particle with a solid object, bubble or droplet. However, there are several fundamental difficulties with a compliant sample that must be addressed before colloidal microscopy can be applied quantitatively to academic studies and practical applications. The purpose of this work is to develop a general method for approaching AFM investigations of highly deformable fluid interfaces and to demonstrate its usefulness in specific areas of interest.

These studies are the first to quantify film drainage and rupture times of aqueous films with AFM between a rigid micro-particle (toner) and an oil drop under dynamic conditions similar to paper recycling. It is also shown that electrosteric stabilization of the oil/water interface due to adsorbing cationic polyelectrolytes may be reversed via lipophilic surfactant addition to the oil. Other investigations of more idealized systems show the necessity of detailed AFM experiments to determine unknown interaction parameters for hydrophobically-driven phenomena. The so-called electrolyte titration is developed to control the net attraction between a hydrophobized-silica sphere and plate, revealing a characteristic curve of probe snap-in distance with concentration that allows accurate fitting of multiple surface forces parameters. From this knowledge, a theoretical force analysis of a sphere deforming a curved fluid interface

**is developed and tested on an oil drop with a polystyrene sphere in water. Fluid interface (FI)-AFM is then adapted to reveal the complexities of the hydrodynamics in a spherically wrapping thin film and of the effects of changing interfacial tension with ionic surfactants.**

## TABLE OF CONTENTS

LIST OF FIGURES.....	iii
LIST OF TABLES .....	v
CHAPTER 1: INTRODUCTION.....	1
1.1 Background .....	1
1.2 Atomic Force Microscopy Techniques .....	2
1.3 Document Layout.....	5
CHAPTER 2: BACKGROUND AND LITERATURE REVIEW .....	7
2.1 Rigid Micro-Particle Interactions with Air Bubbles and Oil Drops.....	7
2.2 The Hydrophobic Interaction .....	10
2.3 Theoretical Considerations for Deformable Interfaces .....	14
2.4 Dynamic Force Analysis.....	17
2.4.1 Mechanical Restoring Forces .....	19
2.4.2 Hydrodynamic Lubrication Forces.....	20
2.4.3 Surface Forces .....	22
CHAPTER 3: SINGLE-PARTICLE OIL AGGLOMERATION WITH AFM.....	24
3.1 Summary .....	24
3.2 Background .....	24
3.3 Experimental Methods .....	25
3.4 Results and Discussion.....	28
3.5 Conclusions .....	33
CHAPTER 4: LONG-RANGE ATTRACTIONS BETWEEN SILANATED SILICA EXAMINED BY AFM ELECTROLYTE TITRATIONS.....	35
4.1 Summary .....	35
4.2 Background .....	35
4.3 Experimental Methods .....	36
4.4 Results .....	40
4.5 Discussion .....	48
4.6 Conclusions .....	52
CHAPTER 5: QUANTITATIVE AFM FOR FLUID INTERFACES.....	53
5.1 Summary .....	53
5.2 Background .....	53
5.3 Experimental Methods .....	54
5.4 Results and Discussion.....	56
5.5 Conclusions .....	67
CHAPTER 6: MICRO-HYDRODYNAMICS OF THIN WRAPPING FILMS IN AFM.....	69
6.1 Summary .....	69
6.2 Background .....	69
6.3 Experimental Methods .....	71
6.4 Results and Discussion.....	75
6.5 Conclusions .....	81
CHAPTER 7: DYNAMIC INTERFACIAL TENSIONS WITH FI-AFM 83	
7.1 Summary .....	83
7.2 Background and Experimental Methods.....	83
7.3 Results and Discussion.....	84

7.4 Conclusions and Recommendations .....	88
<b>CHAPTER 8: CONCLUSIONS AND RECOMMENDATIONS .....</b>	<b>89</b>
8.1 Overview of Results.....	89
8.2 Recommendations for Future Work.....	91
<b>LIST OF REFERENCES .....</b>	<b>95</b>
<b>APPENDIX A: FORCE CONSTANT CALIBRATION OF AFM CANTILEVERS .....</b>	<b>104</b>
<b>APPENDIX B: EXACT SOLUTIONS TO THE POISSON-BOLTZMANN EQUATION FOR CONSTANT POTENTIAL SURFACES .....</b>	<b>106</b>
B.1 Background .....	106
B.2 Overview of Program Subroutines.....	106
B.2.1 Main Program Code for Poisson-Boltzmann Equation .....	106
B.2.2 Function Program Codes for Solving Surface Potential.....	111
B.2.3 Elliptical Functions.....	113
<b>APPENDIX C: DETERMINING DROP PROFILE DEFORMATION DUE TO AN IMPINGING SPHERE.....</b>	<b>114</b>
C.1 The 4 <sup>th</sup> Order Runge-Kutta Procedure for the Young-Laplace Equation.....	114
C.2 The MATLAB Program Code for Parameterized Young-Laplace Equation.....	117
C.2.1 Main Program Code for Calculating Drop Profile .....	118
C.2.2 Function Program Code for Calculating Pressure.....	120
C.2.3 Function Program Codes for Calculating 4 <sup>th</sup> Order Runge-Kutta Estimators .....	120
<b>APPENDIX D: VISUAL BASIC PROGRAM FOR CALCULATING DROP PROFILES DEFORMED BY A RIGID SPHERE .....</b>	<b>121</b>
D.1 Drop Profiles and Force vs. Vertical Drop Deformation .....	121
D.2 Overview of Program and Subroutines.....	121
D.2.1 Main Program Code .....	122
D.2.2 The Pressure Distribution.....	130
D.2.3 Subroutines for 4 <sup>th</sup> -Order Runge-Kutta Procedure.....	132
D.2.4 Subroutines for Parameterized Young-Laplace Equation.....	133

## LIST OF FIGURES

Figure 1.1: Schematic of atomic force microscope (AFM) probing .....	2
Figure 1.2: Force vs. distance diagram for AFM .....	3
Figure 3.1: Schematic of AFM oil droplet probing with liquid cell.....	26
Figure 3.2: Generic force curves of polymer sphere interactions with oil-aqueous interfaces ...	28
Figure 3.3: Toner sphere (100 $\mu\text{m}$ ) in water.....	28
Figure 3.4: Inverse lighting contrast of toner in water .....	29
Figure 3.5: Toner sphere in 0.1 wt% aqueous cationic starch .....	29
Figure 3.6: Oil-toner interaction normalized by sphere radius.....	30
Figure 3.7: Toner engulfment in oil/surfactant under water.....	32
Figure 3.8: Toner (A) approaches oil/surfactant in 0.1 wt% cationic starch .....	32
Figure 4.1: Contact AFM image 400x400 $\text{nm}^2$ of cleaned quartz plate.....	37
Figure 4.2: Contact AFM image 400x400 $\text{nm}^2$ of OTES-quartz plate.....	39
Figure 4.3: Profiles of theoretical snap-in distance for given $\psi_{1o}$ with fixed $\psi_{2o}$ for hydrophobic silica.....	41
Figure 4.4: Profiles of theoretical snap-in distance for given $\psi_{1o}$ with fixed $\psi_{2o}$ for hydrophobic silica.....	41
Figure 4.5: Parametric study of hydrophobic decay length $\lambda$ predicting snap-in distance.....	42
Figure 4.6: Complimentary parametric study (Fig. 4.5) of hydrophobic pre-factor $C_1$ .....	42
Figure 4.7: Force-separation profiles for silanated glass sphere and plate.....	43
Figure 4.8: Electrolyte titration shows snap-in distances and pull-off forces versus $\text{NaNO}_3$ concentration.....	44
Figure 4.9: Parametric study for correlation domain size, $L$ , with fixed pre-exponential factor	46
Figure 4.10: Parametric study on charge correlation strength $C_2$ with fixed $L$ .....	46
Figure 4.11: Total interaction force-field gradients.....	47
Figure 4.12: Snap-in vs. concentration data profile for $\text{NaNO}_3$ titration.....	47
Figure 5.1: FI-AFM schematic: sphere-drop (or bubble) geometry for the Young-Laplace equation.....	55
Figure 5.2: Computed force-distance profile expected from FI-AFM with a polystyrene sphere and n-hexadecane droplet in water .....	57
Figure 5.3: Theoretical DLVO force profile for hexadecane-polystyrene interaction in water for true separation .....	58

<b>Figure 5.4: Experimental data for a polystyrene sphere pushing against an n-hexadecane droplet in 0.1 mM NaNO<sub>3</sub> .....</b>	<b>59</b>
<b>Figure 5.5: Drop apex profiles calculated for axisymmetric deformation by a sphere.....</b>	<b>61</b>
<b>Figure 5.6: FI-AFM profiles for hexadecane-polystyrene interaction in aqueous NaNO<sub>3</sub> solutions.....</b>	<b>62</b>
<b>Figure 5.7: Theoretical F(z) curves for electrolyte titrations at 0.5 and 2 μm/s.....</b>	<b>63</b>
<b>Figure 5.8: Effective drop stiffness (<math>k_{eff}</math>) of n-hexadecane measured for relative interfacial tension decrease.....</b>	<b>66</b>
<b>Figure 6.1: FI-AFM geometric setup: a microsphere interacting by force F axisymmetrically with a drop or bubble across the film of thickness D(r) .....</b>	<b>74</b>
<b>Figure 6.2: Glass sphere interacting with hexadecane in 7 mM SDS solution fitted with the Reynolds equation .....</b>	<b>76</b>
<b>Figure 6.3: Glass sphere interacting with mica in water fitted with the Reynolds equation.....</b>	<b>76</b>
<b>Figure 6.4: Glass sphere interacting with hexadecane in 7 mM SDS .....</b>	<b>77</b>
<b>Figure 6.5: Hexadecane/glass sphere interaction fitted using Eq. 6.2.....</b>	<b>77</b>
<b>Figure 6.6: Hexadecane/glass sphere interaction in 7 mM SDS fitted using Eq. 6.2.....</b>	<b>78</b>
<b>Figure 6.7: Hydrodynamic pull-off measured between a large glass sphere (<math>R_s = 50 \mu\text{m}</math>) and hexadecane in 7 mM SDS solution increases with maximum loading.....</b>	<b>79</b>
<b>Figure 6.8: Hydrodynamic pull-off forces between a smaller glass sphere (<math>R_s = 15 \mu\text{m}</math>) and hexadecane in 7 mM SDS solution scale roughly with <math>R_s</math> .....</b>	<b>79</b>
<b>Figure 6.9: OTES-coated glass sphere (<math>R_s = 4 \mu\text{m}</math>) interacting with hexadecane in water .....</b>	<b>80</b>
<b>Figure 6.10: OTES-glass sphere (<math>R_s = 4 \mu\text{m}</math>) interacting with hexadecane in 7 mM SDS is much more stable to film rupture .....</b>	<b>81</b>
<b>Figure 7.1: FI-AFM of a polystyrene sphere pushing against n-hexadecane in aqueous solutions of SDS. Drop stiffness decreases with increasing SDS.....</b>	<b>84</b>
<b>Figure 7.2: Glass sphere (<math>R_s = 4 \mu\text{m}</math>) against hexadecane in aqueous SDS solutions.....</b>	<b>85</b>
<b>Figure 7.3: F(z) profiles predicted for various interfacial tensions, <math>\sigma</math>, (legend) from the Young-Laplace equation.....</b>	<b>86</b>
<b>Figure 7.4: Dynamic FI-AFM effects with a hexadecane drop stiffness in 10 mM SDS using a polystyrene probe.....</b>	<b>87</b>
<b>Figure A.1: Linear fit of added tip mass to an AFM cantilever as a function of the scaled resonance frequency .....</b>	<b>104</b>

## LIST OF TABLES

<b>Table 3.1: AFM interaction measurements: reported intervals show 90% confidence.....</b>	<b>31</b>
<b>Table 3.2: Comparison of snap-in force from AFM with static advancing oil contact angle under water or 0.1 wt% aqueous cationic starch.....</b>	<b>33</b>
<b>Table 4.1: Dimensional data taken from cross-sectional traces of Fig. 4.1. Values of <math>\Delta</math> are measured between the markers of each profile.....</b>	<b>38</b>
<b>Table 4.2: Dimensional data taken from cross-sectional traces of Fig. 4.2. Values of <math>\Delta</math> are measured between the markers of each profile.....</b>	<b>39</b>
<b>Table 4.3: AFM snap-in distances and pull-off forces from force profiles of hydrophobized glass plate and sphere under electrolyte: 95% confidence intervals reported.....</b>	<b>43</b>

## **CHAPTER 1:**

### **INTRODUCTION**

#### **1.1 Background**

The colloidal interactions of rigid micro-particles with deformable fluid interfaces are not well understood fundamentally and are accessible for study only in very limited configurations under restrictive and ideal environments, most often through some indirect means. The increasing interest in solid-fluid interactions is attested to by the scientific literature, but it is driven by the need to describe accurately various “soft” colloidal behavior for process design, i.e., noncontacting interactions. Air flotation—used for years in mineral separation and printed-paper recycling—and oil-assisted agglomeration may be optimized for other applications such as soil remediation, plastics recycling, or semiconductor polishing. The ability to predict the stability of mixed colloidal systems is equally valuable when considering the quality of paints, cosmetics, and foods, for instance, or strictly as a scientific endeavor for understanding the world around us.

The present work seeks to develop a quantitative method for measuring the forces of interaction between a single, micron-sized particle and a fluid interface, specifically an oil droplet (or air bubble) submerged in water. Earlier endeavors in this field reported apparently long-ranged attractions between various silica spheres and air bubbles in water.<sup>1-3</sup> They linked the observations to a hydrophobic (effect) force, but none had adequate means of determining the bubble deformation to yield the true strength and range of the measured forces. Not long after, the first AFM experiments with oil drops showed proof-of-principle force-distance curves;<sup>4,5</sup> but they also awaited a thorough analysis of the interfacial deformation to provide a justifiable framework for understanding the data quantitatively.

Ongoing efforts have proceeded to gather more abundant experimental data on apparent oil-drop stiffness related to interfacial tension,<sup>6</sup> micro-tensiometry for water contact angles (or surface tensions) with microspheres,<sup>7,8</sup> and semi-quantitative measures of stability.<sup>9</sup> In order to advance AFM studies of fluid interfaces, either a new instrument design is required that can directly measure the separation and/or interfacial profile, or a theoretical model of drop (or

bubble) deformation for a given pressure field must be developed. Only by one of these two methods may truly quantitative force-separation profiles be constructed from the interactions of a rigid body with a deforming interface, leading to definitive knowledge about the absolute strength and range of measured forces and the possibility of fine-tuning colloidal behavior of fluid dispersions with a more fundamental approach.

This research develops the methods for measuring and understanding the behavior of an oil drop deformed by a pressing microsphere so that existing commercial AFM units may be used to obtain force profiles for unambiguous interpretation and comparison with theoretical models.

## 1.2 Atomic Force Microscopy Techniques

The atomic force microscope (AFM) is the ideal candidate for measuring true colloid-scale interactions. The AFM is well suited for detecting and controlling forces directly between a microsphere and another particle or extended surface with the sensitivity to register an individual chemical-bond rupture (picoNewtons). Many different designs are commercially available, but they all have the same basic operating principles for imaging and force profiling.

The adjacent drawing (Fig. 1.1) depicts the central AFM mechanism which typically uses a three-dimensional piezo-electric tube scanner to provide relative sample-probe positioning on a scale of microns ( $\mu\text{m}$ ) to Ångstroms ( $\text{Å}$ ). Any force acting at the probe apex, e.g., sharp cone, pyramidal tip, or sphere, deflects the flexible cantilever. The vertical (and sometimes torsional) displacement is monitored by a reflecting laser and intercepting position-sensitive photodetector (PSPD).

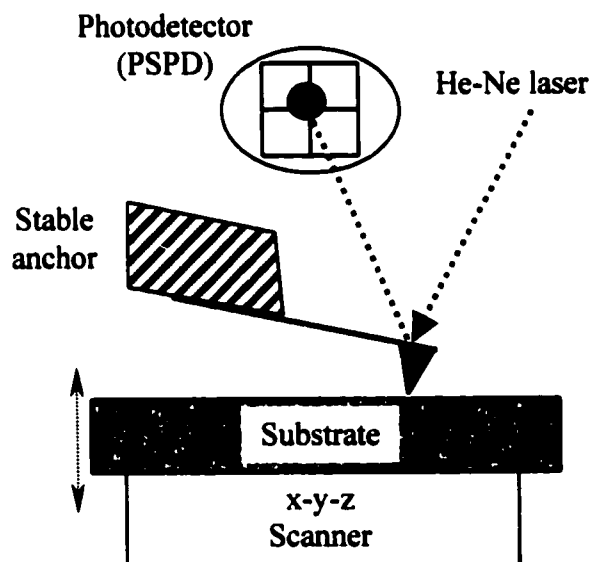
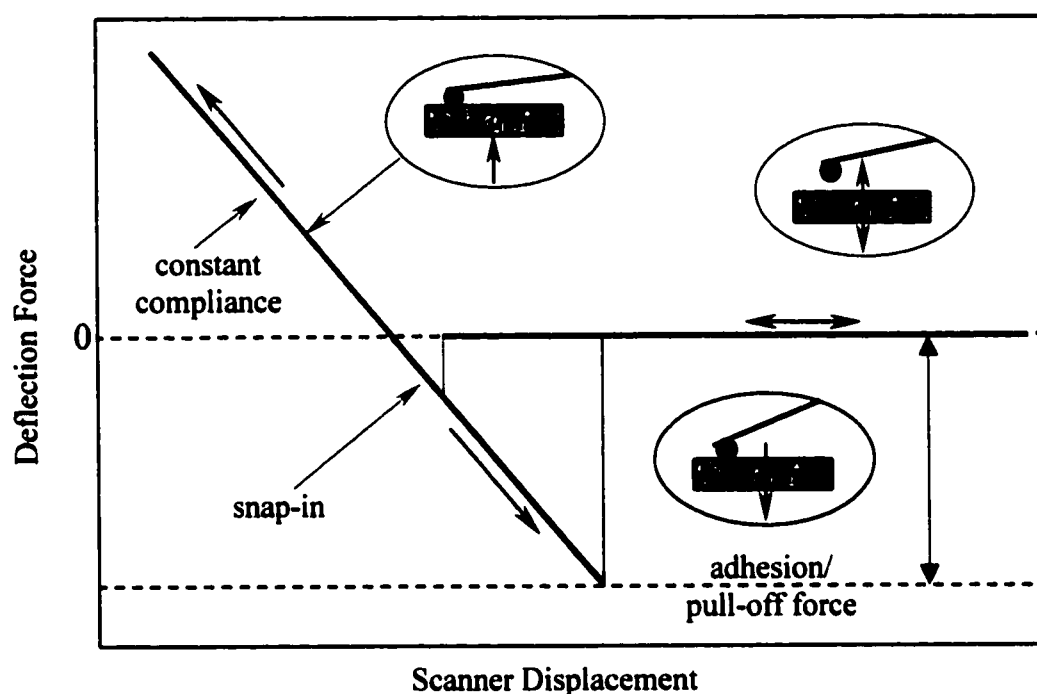


Figure 1.1: Schematic of atomic force microscope (AFM) probing.

The PSPD signal is directly proportional to the interaction force for small equilibrium deflections. For simple contact imaging, the probe is lightly dragged over a substrate to follow

the surface contours (i.e., scanning or rastering). The vertical scanner displacement necessary to maintain a constant cantilever deflection is mapped into an image which corresponds to the topography, which may exceed Å-resolution in all three spatial dimensions. This topographic imaging is the most common use of AFM, though there are numerous other applications for mapping local properties:<sup>10</sup> elasticity, plasticity, viscoelasticity, surface energy, chemical functionality, friction, magnetic and electric domains, etc.

Aside from imaging, the AFM is also used to measure the interaction force,  $F$ , as a function of vertical sample displacement,  $z$ , also known as force spectroscopy. It is from these



**Figure 1.2:** Force vs. distance diagram for AFM shows approach and withdrawal of a microsphere from a rigid surface in air along with cantilever orientation relative to substrate.

$F(z)$  data that profiles of force vs. actual sample-probe separation are constructed for comparison with other systems and with theoretical force curves. A very simplistic force diagram (Fig. 1.2) shows the typical characteristics of probing a rigid surface in air: 1) attractive snap-in to contact due mostly to capillary and van der Waals forces, 2) linear compliance for a rigid substrate, and 3) large pull-off force hysteresis related to adhesion. This ideal picture is complicated for real samples that are physically altered through contact (mechanical deformation or reconstruction),

or for interactions in fluid media when the electrostatic double-layers, hydrodynamics, or other colloidal phenomena become important.

Current methodologies for acquiring force profiles have a number of critical deficiencies that must be addressed in order to investigate oil-particle behavior with an AFM:

1. Determining the separation between sphere and oil droplet.
2. Interpreting the contribution of the ill-defined hydrophobic interaction.
3. Understanding the importance of hydrodynamic drainage in wrapping films.
4. Quantifying equilibrium forces from transient interactions, i.e., snap-in.

The aspiration is that all of these may be suitably addressed and answered; however, there are several fundamental and technical limitations that will restrict the ultimate success of these investigations.

First, standard atomic force microscopy (also AFM) is incapable of measuring the oil-particle separation independently, so it must be inferred from  $F(z)$  data. Careful mathematical description of the oil/water interfacial deformation caused by an impinging sphere allows the true separation to be determined through modeling. The drop profile is described by the Young-Laplace equation (Eq. 1.1), which states that the pressure drop,  $\Delta P$ , across the interface is proportional to the local curvature,  $\kappa$ , where the appropriate scaling constant is the interfacial tension,  $\sigma$ :

$$\Delta P = \sigma \kappa. \quad (1.1)$$

The drop curvature is ultimately expressed as a function of spatial coordinates for the interface. The pressure field is integrated over the interacting surface to compute the net force equivalent to what is measured with AFM. Knowledge of the drop profile evolution is also crucial for determining unknown equilibrium interaction parameters. The difficulty is further increased when dynamic or transient measurements are involved, whether purposefully induced or naturally precipitated by attractive forces, causing rapid deflections of the interface and the AFM cantilever.<sup>1</sup> Besides a classic snap-in caused by capillarity or DLVO (Derjaguin-Landau-Verwey-Overbeek) forces,<sup>11</sup> i.e., the sum of van der Waals and electrostatic double-layer

interactions, another common culprit is the so-called hydrophobic attraction,<sup>12</sup> which is often stronger and of longer range than DLVO forces.

While the following chapters illuminate the role of the hydrophobic force in oil-particle interactions and add to the extant body of knowledge, a truly fundamental understanding of its mechanism is likely far off and awaits further study by the scientific community. These investigations, also, aim to clarify the many aspects of conducting direct force measurements with drops, and bubbles by analogy, as well as to study several system parameters used to control and predict the behavior of dispersed colloidal materials: electrostatic screening, interfacial tension, hydrophobicity, and hydrodynamic film drainage.

### **1.3 Document Layout**

Chapter 2 reviews the scientific literature and addresses in depth the topics of measuring forces between solid particles and fluid interfaces (Section 2.1), the hydrophobic interaction (Section 2.2), theoretical considerations for deformable interfaces (Section 2.3), and a dynamic force analysis (Section 2.4) proposed to deconvolute equilibrium surface forces from transient cantilever deflections. Relevant experiments delving into the first three areas are discussed further in subsequent chapters and are also available in published forms.

Chapter 3 discusses our earlier and more qualitative work that first employed AFM force-profiling to investigations of oil/water interfacial behavior as it related to an oil-assisted fiber-toner separation process for the recycling of toner-printed papers.<sup>5,13</sup> We show, via direct measurement using an unfused toner particle, that cationic starch electrostatically adsorbs to and stabilizes the interface against oil-toner coalescence, and that the addition of a commercial, oil-soluble surfactant reverses this effect.

Chapter 4 describes a parametric study of the solid-aqueous-solid interactions between hydrophobized silica in a sphere-plate geometry for standard AFM force-profiling.<sup>14</sup> Through the addition of salt to the water medium, i.e., an electrolyte titration, the electrostatic component(s) of the interaction are gradually reduced, establishing a useful procedure for determining the hydrophobic interaction parameters of the system. Our results suggest that the extraordinary strength and range of the so-called “hydrophobic force” may often be mistakenly interpreted from less than thorough experimentation, and that observed long-range attractions can be the net effect of two or more phenomena.

Chapter 5 presents the theoretical analysis required for a quantitative AFM measurement of force as a function of actual sphere-drop separation.<sup>15</sup> We discover that the changing curvature of a drop, or bubble, during a fluid interface-atomic force microscopy (FI-AFM) experiment leads to nonlinear interfacial deformation. Numerical deconvolution of interfacial deformation from sphere-drop separation are necessary to obtain useful interaction profiles from the raw  $F(z)$  data.

Chapter 6 shows the increased complexity of hydrodynamics in thin films draining between a rigid sphere and deforming droplet.<sup>16</sup> Direct force measurements show two hydrodynamic regimes in FI-AFM experiments. For thicker films (that is, large sphere-drop separation), the hydrodynamic repulsion is well-described by Reynolds theory for no-slip lubrication. But very thin, wrapping films (viz., small separation) exhibit a much stronger repulsion.

Chapter 7 makes a deeper inquiry into static and dynamic interfacial tension measurements on the micro-scale with FI-AFM. The effects of addition and migration of surfactants, specifically ionic ones, may be quantified by measured changes in forced drop deformations as a function of the magnitude and rate of interfacial displacement. Further detailed refinements of this micro-interfacial tensiometry are discussed by way of recommendations for future work to make this procedure an independent analytical technique.

The major conclusions from this collective body of work are listed in Chapter 8 with recommendations for future research. Appendices follow up on the details of AFM cantilever calibration (Appendix A) and various programs to calculate electrostatic double-layer forces (Appendix B) and drop, or bubble, deformations from AFM force profiling (Appendices C & D).

## CHAPTER 2:

### BACKGROUND AND LITERATURE REVIEW

#### 2.1 Rigid Micro-Particle Interactions with Air Bubbles and Oil Drops

Understanding the interactions of colloid particles with air bubbles and oil droplets dispersed in aqueous dispersions is of great fundamental interest to pulp and paper, mineral, petroleum, and microelectronics industries, to name a few. The knowledge gained from direct observation of single pair interactions is useful for application to processes like printing and plastics recycling, paint and pigment formulation, or semiconductor polishing and cleaning. The proliferation of the atomic force microscope (AFM) has made it feasible and routine to measure equilibrium forces between a colloidal particle and an extended surface, or even a second particle, under fluid.<sup>17</sup> Air bubbles of a few hundred microns in diameter were first studied interacting with silica microspheres,<sup>1-3</sup> and later oil droplets in water were examined with both silica<sup>4,6</sup> and polymer<sup>5,13,15</sup> microspheres under various conditions. Only a few publications over the last few years report AFM measurements of bubbles, drops and films<sup>18</sup> with colloid probes, largely due to the complexity of manipulating or monitoring a highly deformable interface.

Until recently, no work had appropriately described the relation between a measured force and the actual separation between sphere and fluid interface in an AFM experiment.<sup>15,16</sup> Because there is currently no way to control or measure how much the interface deforms when probed on the nanoscale, experiments are limited to providing qualitative or semi-quantitative data at best. H.-J. Butt first showed that AFM was suited for mediating interactions between microspheres and fluid interfaces for the purpose of measuring equilibrium and kinetic forces.<sup>1</sup> While an air bubble under water repelled an approaching glass sphere monotonically (as expected from electrostatics and a negative Hamaker constant), Butt observed a dynamic jump into contact (i.e., snap-in) for spheres made hydrophobic by dichlorodimethylsilane treatment. Both hydrophilic and hydrophobic spheres snapped in when approaching a water drop in air because of capillarity if not an attraction from long-range. Arguably, the most significant contribution from this work was the insight of deconvoluting the transient cantilever deflection (and perhaps interfacial deformation) of snap-in to reconstruct a more traditional force vs.

separation profile to compare with theoretical, equilibrium surface forces. More details of this concept will be addressed in Section 2.4; however, practical application of this technique still awaits further foundational developments.

Similar experiments showed that the addition of sodium dodecyl sulfate (SDS), which adsorbs to the bubble but not significantly to the silica sphere,<sup>19</sup> above the critical micelle concentration (CMC) results in a monotonically repulsive force profile.<sup>2</sup> Below the CMC, film rupture and wetting is induced at some applied load. A silica sphere coated with octadecyltrichlorosilane (OTS) as well as an untreated sphere showed long-range attractions without any measurable repulsion preceding it. However, Fielden *et al.* continued with the silica/water/air system and reported reasonably good agreement with DLVO theory at large separations for cleaned, dehydroxylated (weakly hydrophobic) and OTS-coated spheres in  $10^{-4}$  M and  $10^{-2}$  M NaCl.<sup>3</sup> They noted with particular interest that the measured adhesion, actually a meniscus detachment force, was dependent on the maximum load during approach. This essentially means that higher mechanical potential energy caused a higher degree of immersion and a longer three-phase interline. For sufficiently low loads, the detachment or pull-off force was too small to support meniscus formation, presumably requiring some critical force to rupture the draining film first. The evidence of a smaller, non-capillary pull-off might be explained by a stable, perhaps meta-stable, thin film configuration, a potential well that the probing sphere must overcome to separate itself further from the air bubble. Then, it is also possible that the electrolyte concentration could affect the pull-off force by shifting the potential minimum or altering the surface tension, both of which are likely minor effects.

Other studies looked at the effects of SDS and dodecyltrimethylammonium bromide (DTAB) adsorption on the “hydrophobic” attraction of OTS-silica to the air/water interface.<sup>9</sup> The strong adsorption of SDS to the bubble (but not the silica) maintained the expected monotonic repulsion and decay length with changing ion concentration. Significant SDS adsorbed to the hydrophobic sphere, reduced the attraction (3.7 mM SDS), and eventually recovered a monotonic repulsion at 8.6 mM SDS. In comparison, DTAB adsorbs to silica causing, first, a long-range attraction by reversing the surface charge and increasing the hydrophobicity (0.1-5 mM). Above 6 mM, DTAB adsorbs significantly to the bubble, returning the system to an electrostatically stabilized condition. For the OTS-silica sphere, increasing DTAB likewise reduced the attraction and adhesion. Recognizing the technical hurdles and experimental difficulties involved in the quantitative measurement of force profiles at fluid

interfaces, more recent work by Butt and coworkers has focused on micro-tensiometry with AFM for advancing and receding contact angle measurements.<sup>7-9,20,21</sup>

The first single-particle AFM measurements with a liquid-liquid interface were published by Basu and Sharma, who observed a glass sphere coated with crude oil impinging on mica and glass plates in aqueous electrolytes.<sup>22</sup> The interaction was repulsive for mica in 0.01 M NaCl to a separation of a few nanometers, below which the aqueous film became unstable. The probe snap-in to glass occurred abruptly at 25 nm, clearly a non-DLVO attraction. In both cases, the mechanical instability and liquid bridging of the crude oil might have been the primary causes of deviant snap-in distances. Aveyard *et al.* designed a unique liquid surface forces apparatus to measure force and separation optically between a drop and a flat fluid interface: surfactant stabilized dodecane/water/dodecane films.<sup>23</sup> The drop could easily be replaced by a microsphere in this instrument, but the resolution is poor compared to AFM, which can be similarly adapted.

AFM examination of silica against an n-decane droplet in water<sup>4</sup> was a logical extension of the earlier air bubble experiments. This system is stabilized against coalescence with SDS for making equilibrium measurements. A more detailed study followed comparing the effects of electrolyte and SDS concentrations on contact angle, interfacial tension, and droplet compliance.<sup>6</sup> Weak interactions at large separations correlated well with Debye length,  $\kappa^{-1}$ , for electrostatic screening. The addition of SDS eliminated particle engulfment at all investigated loads, essentially weakening the interface so that it retreated in compliance with a stable thin film.

Recent interests in the interactions of oil/water interfaces concern the recycling of toner-printed office waste by oil-assisted agglomeration,<sup>5,13,24,25</sup> very similar to air-flotation or separation by frothing. Unfused toner ink particles were used to probe a drop of n-hexadecane submerged in water and cationic starch dispersions of concentrations typical in repulped paper slurries for recycling. We obtained force curves with AFM that helped to quantify the ease and strength of particle attachment through *induction times* and *pull-off forces*, both indicators of wetting.<sup>5</sup> Cationic starch adlayers at the oil/water and toner/water interfaces electrosterically stabilized the system against oil-toner coalescence, effectively halting particle aggregation essential for separating toner waste from reusable paper fibers.<sup>25</sup> We have also shown that

lipophilic surfactant blends formulated as agglomerating agents reverse this stabilization by imbibing the starch adlayers into the oil phase, allowing coalescence to proceed unhindered.<sup>13</sup>

## 2.2 The Hydrophobic Interaction

Almost by definition, an alkane oil is hydrophobic, as made apparent by its immiscibility in water. Therefore, the large body of literature attesting to the occurrence of one or more hydrophobically-driven interparticle phenomena begs the question of the existence of a “hydrophobic” interaction when an AFM probe approaches an oil drop in water. Some recent studies on colloidal particles interacting with oil droplets in aqueous solutions (mentioned above) show the occurrence of long-range attractions in several instances. While a number of mechanisms may plausibly explain the results, final conclusions cannot be drawn without giving due note to the still ill-defined hydrophobic force. The oil and polymer spheres (toner and polystyrene) are both strongly hydrophobic as defined by immiscibility and high contact angle with water, respectively; thus, the observation of attractions unexplained by van der Waals or double-layer forces are suspected to be related to a hydrophobic effect. Since the deconvolution of surface forces from AFM data is not generally straightforward, and many observed interactions are still not fundamentally understood, it is essential to have a thorough knowledge of the literature concerning force spectroscopy of hydrophobic surfaces.<sup>14</sup>

The long-range attraction observed between hydrophobic (non-polar) materials in aqueous media has long been exploited in separations and so-called “self-assembly” processes. This “hydrophobic” effect, apart from well-characterized DLVO forces, is often a major contributor in commonly studied phenomena like flocculation in colloids, surfactant structuring into micelles, vesicles, and lamella, and adsorption.<sup>26</sup> There appears at present to be no established theory that completely explains the collective results in a unified manner. Though a single explanation would be desirable, the most reasonable arguments suggest there may be several “hydrophobic effects,” distinctly different mechanisms for long-range non-DLVO interactions.<sup>27-30</sup>

Attractive forces with a 1-2 nm decay length are observed between all kinds of hydrophobic surfaces in aqueous media, but significantly “longer-range” attractions are often measured that seem to be influenced more by surface structure or mobility rather than macroscopic hydrophobicity.<sup>27</sup> In retrospect, this justifies the fairly common, empirical usage of

a single- or double-exponential function added to the classical DLVO theory to fit “hydrophobic” forces.<sup>31</sup> At least two non-DLVO interactions appear to be required in order to reconcile the collective findings to date. A current list of possible mechanisms include solvent structuring (the self-association of water being the most common),<sup>12,32</sup> dipolar-van der Waals and electrostatic correlation forces,<sup>33-37</sup> submicroscopic bridging bubbles,<sup>38,39</sup> cavitation,<sup>40-42</sup> bridging macromolecules,<sup>31</sup> and contact region capillary condensates.<sup>43</sup>

Systematic investigations have used the surface forces apparatus (SFA) and AFM along with other custom devices for measuring interaction forces and force gradients between carefully prepared hydrophobic surfaces. They are of four basic kinds: adsorbed surfactant (including self-assembled monolayers, or SAMs), LB films, chemically modified substrates, and solid polymers.<sup>28</sup> The strength of hydrophobic attractions shows a general correlation with wettability as measured by the contact angle,  $\theta$ , of water, and perhaps other liquids as well.<sup>12,29,41,44,45</sup> Non-wetting ( $\theta > 90^\circ$ ) and weakly hydrophobic surfaces ( $\sim 40-60^\circ < \theta < 90^\circ$ ) show increased attraction with larger contact angle, while more hydrophilic surfaces behave according to DLVO theory and have short-range, repulsive hydration forces increasing to  $\theta = 0^\circ$ . The range of non-DLVO attraction also seems to depend on the surface preparation independently of contact angle, suggesting links to partial surface coverage and patchiness<sup>46</sup> or surface group mobility.<sup>47</sup> The interaction range correlates as follows<sup>28</sup> with several noted exceptions:<sup>34,44,48,49</sup> LB techniques ( $>100$  nm)  $\geq$  chemical modification (50-100 nm)  $\geq$  surfactant adsorption  $\geq$  solid polymers ( $<30$  nm). Large hysteresis in advancing and receding contact angles is an indicator of patchiness or surface rearrangement. The range of the hydrophobic attraction seems to scale with the hysteresis magnitude and may be relatively insensitive to the degree of maximum hydrophobicity.<sup>46,47</sup>

There is significant evidence for water (solvent) structuring affected by surface wettability where the chemical potential difference between bulk water and surface water equilibrates by establishing a density gradient,<sup>12</sup> but it is difficult to argue for an influence reaching hundreds of molecular lengths without significant additives. It is this argument that suggests solvent structure is perhaps the most likely candidate for the shorter hydrophobic, or even a more general solvophobic, attraction decaying on a scale more comparable to the size of the medium molecule. Recent findings also suggested that reducing water chemical potential, e.g., reducing dielectric constant or solvent bulk density, through large increases in electrolyte

concentration increases the hydrophobic attraction without significantly changing surface wettability or water surface tension.<sup>50</sup> Non-aqueous solvent addition lowers the surface tension, decreasing the contact angle and showing decreases in the long-range attraction that do not necessarily disappear in the absence of water.<sup>29,37,41,45</sup> While this is not yet a closed case, it makes the other proposed “hydrophobic” mechanisms seem more reasonable for the longer-range interactions.

Many researchers have shown some apparent connection between electrostatics and the hydrophobic effect other than that predicted by conventional electrostatic double-layer theory. Craig *et al.* recently discussed the disparate results on the role of electrolytes in hydrophobic interactions<sup>28</sup> finding that the long-range attraction increases,<sup>41,50</sup> decreases,<sup>31,33,37,48,49,51-54</sup> and remains unchanged<sup>46,55-58</sup> with increasing electrolyte concentrations for a variety of systems. The majority of these examinations have been conducted on LB films or adsorbed surfactant monolayers whose very structure and coverage can be altered with changes in electrolyte concentration, directly altering surface charge density and/or wettability and leading to interpretative ambiguity as to the real cause of force variation.

Correlations or fluctuations of surface charge or dipole domains, closely related to van der Waals dispersion interactions, are at least qualitatively feasible arguments for attractions between similar or dissimilar surfaces over a range that scales with domain size, spacing, and the Debye length.<sup>33-37</sup> Evidence for an electrostatic origin of the “longer-range” hydrophobic effect presented by Kékicheff and Spalla is somewhat obscured by the effect of increased surfactant adsorption with salt.<sup>34</sup> In spite of this, their data for electrically neutralized glass in cetyltrimethylammonium bromide (CTAB)/KBr solutions give a strong argument for correlating charge domains that are screened by half the Debye length,  $\kappa^{-1}/2$ , while the other experiments are only somewhat less convincing. Above some degree of screening, the correlation effect will be negligible compared to the actual hydrophobic effect whose presumably constant decay length would then be larger than the reduced correlation decay length. To the contrary, there are a number of experiments measuring attractions with decay lengths greater than the Debye length for very low electrolyte concentrations.<sup>41,48,49,59</sup>

The effect of electrolyte addition on some hydrophobic attractions may be a synthesis of solvent and surface structure phenomena. If so, experimental outcomes should be more definitive with naturally hydrophobic materials or chemically modified surfaces that remain

unaltered by ions in solution, thus eliminating one variable. A piezo-bimorph surface force apparatus using glass hemispheres hydrophobized with fluoro-functional silanes found slightly increased adhesion (10%) and strength and range of attraction (10%) by adding salt (pure water, 0.002, 0.01, 0.1, 1, 5 M NaCl). The authors linked this to increased surface tension (10%) and argued against any electrostatic mechanism in favor of submicroscopic bubbles or cavitation.<sup>41,60</sup> Conversely, force profiles between zinc sulfide spheres showed decreasing attraction with elevated KCl concentration at low pH.<sup>54</sup> Yet another study of non-DLVO attractions between stable hexadecanethiol SAMs in pure water doubled in range when the salt concentration was raised to 1.5 M NaCl, but there was no significant effect below 0.1 M.<sup>50</sup> The strength of adhesion seemed to be insensitive to electrolyte type but increased linearly with osmolality, in this case, water chemical potential or dielectric reductions. Also, the strength of adhesion is believed to be affected by the presence of salt when the surfaces are altered by competitive adsorption/desorption or other ion-induced surface modification.<sup>53,61,62</sup> Many arguably stable, hydrophobic surfaces (silanated silica or mica, polymers, etc.) have never been studied over a range of electrolyte concentrations,<sup>44,63-66</sup> and no definitive electrolyte dependence has been observed in interactions between polystyrene,<sup>57</sup> polypropylene,<sup>58</sup> and LB-deposited and polymerized alkylsilane films on mica.<sup>46</sup> It is significant to note that only relatively short-range attractions were observed in the latter studies.

Submicroscopic bridging bubbles cannot be dismissed as a possible hydrophobic interaction mechanism, where the range of attraction would be essentially fixed by the size of the bubble. A pre-formed bubble can pull two hydrophobic surfaces together in aqueous media when both are dewetted by the same cavity, making the more exotic explanation of unusually long-range cavitation unnecessary. Sufficiently large gas bubbles trapped on submerged surfaces may persist for hours or even months without careful de-aeration,<sup>38</sup> though any bubbles of colloidal dimensions on smooth surfaces are predicted to dissolve within microseconds and could not be a cause for attraction.<sup>67</sup> Cavitation certainly occurs between non-wetting surfaces in water at some small separation,<sup>40</sup> but it is thermodynamically unlikely at separations much larger than a few nanometers.<sup>43</sup> More troubling yet is the creation of stable air pockets during probing after the first contact.<sup>39</sup> Previous theories for bubble formation and stability have not considered the possibility of surface roughness maintaining a mesoscopic vapor cavity for minutes or hours, which is experimentally justified in some cases, though perhaps consistently

refutable in others. Regardless, these are all arguably issues of wettability and film stability that may eventually be reconciled as theories and observations are pieced into a larger understanding of the consequences of strong colloidal interactions.

Chemical species that are relatively free to migrate or that have some initial bulk concentration in the liquid medium, such as adsorbed surfactants or Langmuir-Blodgett (LB)-deposited molecules, may condense within the contact region of two surfaces. This would add a long-range capillary component to the interaction that is hydrophobically driven. For this reason, adsorbed macromolecules or other self-assembled structures may not produce practical surfaces for unambiguous investigations. The argument has also been made that because many adsorbates are not well anchored, a large portion of the adlayer could delaminate, snapping into mutual contact long before the substrates touch.<sup>43</sup> Most chemically hydrophobized surfaces of study have been silanated silica substrates, and their structural stability is well established.

Most recently, we have quantified the strength and range of the hydrophobic force from AFM snap-in distances measured during an electrolyte titration of the electrostatic forces for silanated glass and quartz (Chapter 4).<sup>14</sup> The reproducible minimum snap-in distance at intermediate salinity was predicted from computational parametric studies of cantilever snap-in caused by DLVO and hydrophobic forces. A characteristic trend in experimental snap-in was best fitted with the inclusion of an attractive electrostatic correlation, which is distinctly independent from the hydrophobic effect. Far from settling the debate of the extraordinarily long-ranged “hydrophobic” forces, there is now strong evidence pointing toward a multiplicity of sources for long-range attractions that appear in systems with low energy surfaces.

### **2.3 Theoretical Considerations for Deformable Interfaces**

When considering the interactions of a fluid-fluid interface with either a rigid probe or another deformable body, the greatest impediment to acquiring a useful plot of the force with separation is directly related to the mobility of the interface. A liquid interface can only resist a very weak normal stress before deforming significantly. Thus, it is difficult, even impossible in some instances, to accomplish a controlled study of equilibrium forces with bubbles, drops, or films. If an approaching drop is repelled from a rigid body—perhaps the simplest case—the configuration is stable; but if they are attracted, the fluid will dynamically jump into contact, defeating the experimental goal. In either case, knowing the separation from an air bubble or oil

drop is problematic since it cannot be inferred from the displacements of the AFM cantilever and scanner, for example, which is sufficient for rigid bodies.

Only slightly less troubling is the changing area of interaction as the surface deformation proceeds. In order to make quick comparisons between interaction profiles of diverse geometries, the force is often normalized by the radius of curvature of the system. Thus, the data are appropriate for plotting against theoretical interaction energies of parallel plates via Derjaguin's approximation (Eq. 2.1).<sup>26</sup> In the very simple case of a sphere and plate, the force,  $F$ , acting between them is proportional to the flat plate energy per unit area,  $W$ , by the factor of  $2\pi$  times the radius of the sphere,  $R$ , where plate separation is the same as distance between sphere apex and plate:

$$F = 2\pi RW. \quad (2.1)$$

Conveniently, for AFM force profiling where a sphere is usually the probe of interest, the most prevalent presentation is that of  $F/R$ , though  $F/2\pi R$  is, of course, suitable. However, when a liquid interface is the object of study,  $R$  effectively changes as a function of force, and thus, separation. In the past, this has been acknowledged and then largely ignored since the fluid deformation is almost never known. But the problem of true separation and system curvature is the crux to acquiring quantitative data for fluid interfaces.

A majority of researchers have converted AFM displacement into separation by assuming a Hookean spring analogy for the deflecting fluid interface.<sup>2</sup> It began with the argument that the actual deflections are very much smaller than the radius of bubble or drop and should give a fairly linear response with force. This assumption was checked by measuring the change in force,  $\Delta F$ , with displacement,  $\Delta d$ , at high load under repulsive conditions where the contribution of film thinning was negligible compared to the deflections of the interface and the cantilever. The actual change in separation for an experiment is estimated with an inferred interfacial spring constant,  $k_i$ , which is calculated from the known cantilever deflection and total displacement, assuming two springs acting in series:

$$\frac{\Delta d}{\Delta F} = \frac{1}{k_s} = \frac{1}{k_i} + \frac{1}{k_c}. \quad (2.2)$$

The cantilever certainly obeys Hooke's law, having a linear force constant,  $k_c$ , and the measured stiffness,  $k_s$ , appears to be approximately linear, as well. However, there is no well-defined point of zero, or closest, separation, so any separation scale is strictly arbitrary to within an additive constant. This does not provide the strongest argument for satisfactory comparisons to theoretical surface force models. Beyond this, there is actually theoretical support for a significantly nonlinear interfacial response of a drop pushing against a plate, and this effect may be all the more critical for interpreting sphere-drop interactions.

Some few and novel experimental designs allow for direct measurement of the separation between the interface and the probe. One AFM built for air bubbles used laser interferometry to detect bubble deflection,<sup>68</sup> though no quantitative results have yet been published. Optical interferometry was also employed in the liquid surface forces apparatus to follow the approach of two oil interfaces approaching in water.<sup>23</sup> Similarly, the separation of a mercury drop and mica plate was measured with an SFA and the results compared with a theoretical model including the interfacial profile.<sup>69</sup> They all show exciting promise, but the commercial AFM units are capable of equal or superior performance in force measurement and sample displacement control. Their ubiquity makes it highly desirable to develop a means to use them with minimal modifications, and this is possible with a more precise understanding of how the drop profile develops with applied force.

Some enlightening theoretical and experimental work showed that a curved fluid interface deforms exponentially with separation from a flat plate when considering only electrostatic double-layer forces between them.<sup>69-72</sup> This is essentially linear deformation with applied force at large separations, coincidentally a weak overlap regime. There is also a very minor but consistent trend of the force decay length falling short of the predicted Debye length, and the difference is exaggerated with increased electrolyte concentration or decreased interfacial strength. This discrepancy in decay length is quite small when considering typical experimental errors and will not be confirmed easily. It is difficult to attribute any physical significance to this finding except the suspicion that it is somehow linked to the form of the surface force(s) involved.

This theoretical model based on the Young-Laplace equation (Eq. 1.1) also predicts that a "limiting separation" is reached when the surface pressure equals the internal pressure of the fluid droplet. For constant internal drop pressure, these two surfaces cannot come closer than this limit. At this point ( $D^*$ ), the fluid interface has conformed to the geometry of the surface

forming parallel plates, and the net radius of curvature diverges faster  $\{\sim 1/(D-D^*)\}$  than the net force  $(\sim \{\ln(D-D^*)\}^2)$ . The area of interaction increases with decreasing separation, thus the net force increases. The final composite relation depicts two interaction regimes: 1) at large distances the force varies exponentially with separation, probably a direct consequence of the surface force considered, here, double-layer repulsion, and 2) at smaller distances, approaching the limiting separation, the force rises to infinity, and the interface moves in tandem with the plate, usually called constant compliance.

We have made similar conclusions from computations based on the solid sphere-deforming droplet configuration that represents colloidal AFM studies. The most significant difference is the limiting separation. When the AFM probe in the form of a microsphere deforms a curved interface via repulsive forces, the local interfacial curvature may invert and then continue to decrease in magnitude until the local drop radius is equal and opposite the sphere radius. The interface wraps around the sphere forming an interaction area equivalent to parallel plates, i.e., zero local net curvature. The final film thickness in this case can be as much as an order of magnitude smaller than that for the analogous drop-plate.

In order to understand truly quantitative measurements of interaction forces between colloidal particles and liquid interfaces, the separation must be describable theoretically when it cannot be measured directly. Since the most feasible and common means of force-profiling is AFM, the development of an appropriate numerical model to calculate separation from applied force is timely. Chapter 5 presents a detailed discussion of this analysis.

## 2.4 Dynamic Force Analysis

Finally, the pinnacle of AFM for measuring force profiles of drops and bubbles will be either an instrumental breakthrough, a wonder that controls interfacial mobility, or a theoretical construct capable of unambiguously interpreting dynamic and transient deflection data. AFM and SFA instruments are all limited to measuring repulsive and weakly attractive “near-equilibrium” forces via a flexible cantilever. The separation between sphere and plate is controllable only while the force-field gradient is less than the cantilever stiffness.<sup>56</sup> A gradient larger than the spring constant causes a dynamic “jump-in” or “snap-in” event during which the cantilever-particle assembly accelerates toward the interface until the particle makes contact. A very stiff spring will experience no instability but will not resolve any forces, while a very weak

spring will snap-in before any static deflection can be detected. This problem of static spring instability can be circumvented by the laborious and undesirable process of systematically increasing the cantilever stiffness, thus inferring stronger attractions from a plot of force-gradient vs. separation. This is not feasibly done for AFM experiments without introducing unacceptable uncertainties when exchanging one probe for another.

Custom modifications to conventional SFA<sup>45</sup> and AFM<sup>73</sup> provide force feed-back schemes to maintain constant cantilever deflection by using a magnetic force transducer and a differential capacitance sensor, respectively, to control the effective cantilever stiffness. These designs increase stability within attractive regimes, but the ability to control separation is first limited by the finite feed-back response time and ultimately by surface deformation when van der Waals attraction finally overcomes the material strength, regardless of cantilever stiffness, pulling the surfaces together. Probing fluid interfaces is inherently difficult because of how easily and rapidly they can deform under colloidal interactions.

A dynamic force analysis of the deflection during snap-in is another way of constructing an equilibrium force profile,<sup>1</sup> which has yet to be successfully accomplished in a quantitatively meaningful way. This is, presumably, the only way to quantify forces for attractive interactions involving fluid interfaces. Even with equipment modifications, there is no way to immobilize a bubble or drop against mechanical instability. Only under repulsive and weakly attractive regimes do both the cantilever and interface have stable equilibrium deflections. Usually the cantilever will be the stiffer "spring" with the interface snapping into contact first. However, the loss of information during the unavoidable deviation from static testing conditions can be compensated for if an appropriate force balance considering transient motion is used to interpret experimental results. Then, a surface force profile can be constructed from high resolution deflection data recorded during snap-in. Standard AFM data acquisition hardware is not fast enough nor is the software designed to gather the data on the microsecond scale. Therefore, a high-bandwidth oscilloscope may be connected to the AFM head to record the deflection signal,  $z(t)$ , directly from the photodetector. Determining sphere-sample separation is still straightforward for rigid substrates, but is now rather more complex for the deforming oil drop (Chapter 5).

There are essentially three types of interaction forces to be considered for measuring the interaction of two bodies in liquid with AFM or similar techniques:

1. Mechanical restoring forces:  $F_K$ .
2. Hydrodynamic lubrication or viscous forces:  $F_H$ .
3. Surface or colloidal forces:  $F_S$ .

The mechanical force is equated with the sum of the hydrodynamic and surface forces. In general, this equation cannot be solved analytically for separation as a function of time,  $D(t)$ . However, for rigid interfaces  $D(t)$  is known from the experiment and is equivalent to knowing the minimum film thickness. The total intermolecular force profile,  $F_S(D)$ , is obtained with complete knowledge of the relationships for  $F_K$  and  $F_H$ , and herein lie the greatest difficulties. Assuming these can be adequately addressed, the final goal is to determine which independent colloidal interactions are represented in the net force profile and to quantify physical properties with this AFM technique. This will require supplementary information about some minimum number of interaction parameters for surface forces in order to fit one unknown parameter unambiguously, although it is also possible to design experimental parametric studies in order to fit multiple unknowns (Chapters 4-6).

Personal communication with H.-J. Butt revealed that predicting the behavior of cantilever mechanics in the near field is not as straightforward as his simple second-order Newtonian analysis assumed.<sup>1</sup> Butt and coworkers continue to investigate. The rest of this chapter discusses the current state of dynamic AFM analysis, but the research presented in the following chapters focuses extensively on pseudo-steady state measurements to explain some of the more pressing issues with the hydrophobic interaction, thin film hydrodynamics, and a slowly deforming interface. These must all be well understood before a valid dynamic force analysis for drops and bubbles, or even solid plates, can be pursued further with any success.

### ***2.4.1 Mechanical Restoring Forces***

The mechanical restoring force,  $F_K$ , is ultimately resisted by the sample being probed, whether rigid or deformable. If the latter, then the amount of deformation must also be known to infer the true separation, but this does not complicate the calculation of  $F_K$ , which requires only  $z(t)$  for the static, viscous damping, and inertial forces of the probing sphere attached to the cantilever (Eq. 2.3). This application of the second-order equation of motion is already familiar from the initial work of H.-J. Butt:<sup>1</sup>

$$F_k = m \frac{d^2 z}{dt^2} + K_D \frac{dz}{dt} + k(z - z_o). \quad (2.3)$$

Here,  $m$  is the effective mass of the entire sphere-cantilever assembly in the probing fluid medium,  $K_D$  is the damping constant, and  $k$  is the normal spring constant of the cantilever.

Frictional drag on the approaching sphere and cantilever are usually made negligible when a sufficiently slow approach rate is maintained. Indirectly, this Stokes type drag,  $F \propto 6\pi\eta vR$ , will be dependent on separation within the colloidal force range because this will affect the true relative approach velocity of the sphere. However, the hydrodynamic lubrication effects should always dominate this frictional drag at least by  $R/D$  (Reynolds theory, Eq. 2.4), which is often a factor of 100 or more for colloidal AFM. The  $K_D$  term need only be considered in the dynamic analysis to prove quantitative accuracy.

All of the forces acting in a liquid medium between a solid plate and sphere should still be valid for the liquid interface, but with a moving boundary condition the force balance must encompass the drop profile, as well. Previously in the literature, the deformation of the interface has been dealt with as a simple spring in series with the cantilever (Eq. 2.2), and it was lumped into  $k$  of Eq. 2.3. A rigorous expression for the interfacial deformation requires the Laplace pressure (Eq. 1.1) be included in the dynamic model. It will be necessary first to solve the Young-Laplace equation (Chapter 5) using the applied dynamic force to find the separation and the entire interfacial profile from which to build the surface force profile. The numerical complexity of the procedure requires iterative routines to find the solution, and other phenomenological issues have been raised that must be resolved before proceeding with any dynamic force analysis, even of rigid planar samples (discussed below). Further, the dependence of interfacial tension on film thickness will also have an effect on the interaction behavior but only for very thin films. This would not be incorporated into the analysis in the foreseeable future since AFM experimental sensitivity does not detect force variations on this length scale for a "thin-thin film" of a few molecular lengths.

### ***2.4.2 Hydrodynamic Lubrication Forces***

Hydrodynamic lubrication forces are often evaluated with the aid of Reynolds lubrication theory for pseudo-steady state regimes (Eq. 2.4); but it is immediately recognized

that this is not a valid assumption for AFM snap-in even though it might be sufficient. A simplified Navier-Stokes equation of momentum along with continuity of mass, no-slip boundary conditions, and an approximation for the curved surface (a sphere of radius  $R$ ) yields the creeping flow ( $Re \ll 1$ ) velocity profile for the thinning film:

$$F_H = -\frac{6\pi\eta R^2}{D} \frac{dD}{dt}. \quad (2.4)$$

Here,  $dD/dt$  is the velocity or film thinning rate,  $\eta$  is the fluid dynamic viscosity, and  $D$  is the film thickness. A good example analysis for the crossed cylinders or sphere-plate system is found in a paper by Chan and Horn.<sup>74</sup> They showed that their model compares well with experiments using mica and dispersive liquids in the SFA.

While this simplified Reynolds lubrication is not strictly valid for transient flow, it has proven empirically sufficient in some cases for variable velocity and  $Re > 1$ .<sup>38</sup> But common impact mechanics equations suggest another, more complicated relation. Clark and Burmeister<sup>75</sup> used a derivation for transient drainage of a cylinder approaching a flat plate end on (Eq. 2.5) to approximate a sphere-plate interaction with good experimental agreement when the radius was of the order of a few hundred microns:

$$F_H = -\frac{3\pi\eta R^4}{2D^3} \frac{dD}{dt} - \frac{\pi\rho R^4}{8D} \frac{d^2D}{dt^2}. \quad (2.5)$$

The second term is inertial and often insignificant even in transient regimes. Considering other common geometries for hydrostatic bearings, e.g., triangular wedge, cylinder, spherical journal, the same basic relationship in force vs. distance is evident:

$$F_H = -\frac{\eta R^4}{D^3} \frac{dD}{dt} f, \quad (2.6)$$

where  $f$  is unitless and may be an explicit function of or a constant scalar specific to system geometry. We derive a similar equation for approximate spherical geometry, resulting in a somewhat intermediate equation that simplifies to Eq. 2.4 for typical AFM experiments:

$$F_H = -\frac{6\pi\eta R^2}{D} \frac{dD}{dt} f_1(R, D) - \pi\rho R^3 \frac{d^2D}{dt^2} g_1(R, D) \quad (2.7)$$

The first-order approximation replaces the functions  $f_1$  and  $g_1$  with unity, where they strictly represent generalized series expansions for arbitrary geometries that can be expressed by some equivalent radius of curvature and the separation. Future developments by Rajagopalan and coworkers<sup>76,77</sup> may provide techniques to measure hydrodynamics near interfaces with a vibrating cantilever or optically-trapped sphere in a way that distinguishes between transient effects and equilibrium interactions. However, it is clear that the quantitative description of a rapidly moving AFM cantilever near a surface in fluid is yet to be formulated.

Beyond these details, the no slip boundary condition may also be a poor assumption for hydrophobic or fluid interfaces.<sup>78-81</sup> A lubrication relationship based on the form of Reynolds equation (Eq. 2.4) has been developed which is additionally a function of the degree of hydrophobicity and a fluid boundary slip length. All things considered, the dynamic lubrication effect may not be consistent with any one of these relations during snap-in; but at least a semi-quantitative relationship should be experimentally apparent that scales similarly. Furthermore, the deforming interface greatly complicates the hydrodynamic issue and will be addressed in some detail in Chapters 5 and 6.

### 2.4.3 Surface Forces

After the surface force profile is obtained from the mechanical/hydrodynamic deconvolution, the various colloidal force contributions are considered to determine a best fit with theory. First, the well-known DLVO forces may be simply represented by the following equations for the van der Waals (Eq. 2.8) and electrostatic double-layer (Eq. 2.9) components for a sphere and plate configuration:

$$F_{vdW} = -\frac{AR}{6D^2}, \quad (2.8)$$

$$F_{el} = \frac{4\pi R\sigma_1\sigma_2e^{-\kappa D}}{\epsilon\epsilon_0\kappa}. \quad (2.9)$$

The separation is again expressed as  $D$ ,  $A$  is the Hamaker constant with sphere radius,  $R$ , surface charge density,  $\sigma$ , Debye length,  $\kappa^{-1}$ , permittivity of free space,  $\epsilon = 8.8542 \times 10^{-12} \text{ C}^2/(\text{N}\cdot\text{m}^2)$ , and dielectric constant,  $\epsilon_r$  ( $\approx 80$  for water). The assumption of a non-retarded van der Waals

interaction is sufficient, since none of our AFM experiments are sensitive enough to distinguish an error associated with this approximation. Likewise, deviations caused by zero-frequency screening effects are negligible. Equation 2.9 is a weak overlap approximation for low surface potentials ( $\leq 25$  mV) where surface charge density can be expressed as  $\sigma_i = \epsilon\epsilon_0\kappa\psi_{oi}$  and  $\psi_{oi}$  is the isolated surface potential. More exact calculations are necessary for higher magnitude in and greater disparity between surface potentials (Chapters 4-6); these may be executed numerically with the help of MATLAB or Visual Basic code based on previously published work<sup>82</sup> (Appendices B, C & D) or on more rigorous analytical approximations.<sup>83</sup>

For low surface energy materials in water, like hydrocarbons, it is also important to consider the hydrophobic force,  $F_h$ , described as a long-range attraction decaying exponentially with separation (details in Section 2.2 and Chapter 4). Thus, the total surface force is simply the sum of a few independent interactions:  $F_s = F_{vdw} + F_{el} + F_h + \dots$ . Structural forces may become important at very small separations of the order of molecular length scales, and contributions from other long-range phenomena may be examined or discovered, as well. Any unexpected or ill-defined interactions greatly complicate the issue of fitting parameters unless supporting experiments are possible. By way of Ockham's Razor, the fewer number of mechanisms required to explain reality the better, unless there is a strong argument for added complexity.

## CHAPTER 3:

### SINGLE-PARTICLE OIL AGGLOMERATION WITH AFM

#### 3.1 Summary

This chapter examines the feasibility of using atomic force microscopy (AFM) for direct study of colloidal particle-droplet interactions, showing practical application to separation processes.<sup>5,13</sup> Specifically, the interactions of a toner particle or analogous polystyrene sphere (10-20  $\mu\text{m}$  diameter) with various oil/water interfaces are observed using AFM to determine the effects of adsorbed polymer, surfactants, and collision rate on particle attachment and detachment, i.e., the success and efficiency of toner ink removal from a mixed slurry. The particle glued to an AFM cantilever probes the oil interface while both are submerged in a water-filled cell to simulate selective oil-assisted agglomeration for recycling toner-printed office waste.

These studies were the first to show quantitative measurements of drainage and rupture times (also, induction times) of aqueous films between a rigid micro-particle and a liquid drop under dynamic approaches ( $\sim 30 \mu\text{m/s}$ ) with force-profiling AFM. This experimental design makes possible a direct force measurement of electrosteric stability imparted by adsorbed macromolecules to both particle and oil interfaces. Our previous bulk agglomeration studies are compared to the single-particle analysis accomplished with a colloidal probe AFM.<sup>5,24,84</sup>

#### 3.2 Background

The first report by Ducker *et al.* of particle (7  $\mu\text{m}$  diameter) attachment to an AFM cantilever demonstrated the ability to probe colloidal forces under liquid environments.<sup>17</sup> The so-called *colloidal force microscopy* is not a conventional AFM scanning mode but has come into common practice for measuring solid-solid interactions over the last several years and has more recently been applied to a few solid/fluid/fluid interfacial studies: spheres near air bubbles<sup>1-3</sup> and oil droplets<sup>4-6,13</sup> in water.

The efficacy of oil-assisted agglomeration has been investigated for recycling toner-printed paper, a process governed by the colloidal interactions of oil droplets and toner (polymeric/mineral) particles.<sup>24,25</sup> The critical processing step in toner de-inking is the coalescence of dispersed toner and oil into large, strong aggregates that can be easily removed from the repulped paper slurries leaving clean cellulose fibers for reuse in paper-making. De-inking effectiveness is dependent on several factors, the most important of which is arguably the presence of cationic starch in the repulped paper slurries. This ubiquitous polyelectrolyte reduces and even eliminates oil-toner agglomeration by adsorbing to the oil ( $18 \text{ mg/m}^2$ ) and toner particles ( $3 \text{ mg/m}^2$ ), forming electrosteric adlayers that strongly repel upon close approach.<sup>25</sup>

The present work examines the interaction of a toner particle consisting mostly of poly(styrene-co-acrylate) with an n-hexadecane (oil) droplet and a commercial oil/surfactant, in pure water and in 0.1 wt% aqueous cationic starch dispersion. The ability of cationic starch to halt toner agglomeration was observed in previous aggregation experiments<sup>24,25</sup> and has been confirmed directly in this work with optical and atomic force microscopies.<sup>5,13</sup> Cationic starch adsorption renders coalescence highly unfavorable. Differences in force profiles for oil-toner interactions indicate the presence and specific effects of starch adlayers. Oil agglomerating agents containing lipophilic surfactants are added to encourage coalescence against the electrosteric resistance.

### 3.3 Experimental Methods

The single-particle AFM experiment is a nearly ideal method for direct comparison to bulk agglomeration studies that gauge the final degree of toner aggregation. A Park Scientific Instruments AutoProbe® CP AFM was used to measure the interaction forces in aqueous media of an approaching oil droplet and toner particle at similar conditions found in repulping agitation tanks (i.e., high velocity). Of particular interest are the attractive force, if any, between the toner and oil, the applied force required to induce toner attachment or film rupture, and the induction time—estimated from the time the toner is first repelled by the interface until snap-in indicates film rupture and wetting as it enters the oil. These parameters are measured from AFM force vs. distance data acquired while approaching and retracting the oil from the toner particle and

qualitatively compared with wetting measurements—advancing oil contact angles on printed toner flats under water.

The schematic in Fig. 3.1 shows an unfused toner particle roughly  $10\ \mu\text{m}$  in diameter glued with Devcon™ S-208 fast-cure epoxy at the end of a commercial AFM cantilever ( $k = 0.05\ \text{N/m}$ , ML06A, Park Scientific Instruments) which is lowered into the vinyl liquid cell for probing. The particle taken from Apple Laser Writer™ toner powder is composed of 55-65 wt% styrene acryl copolymer ( $\sim 1:1$  mole ratio), 30-40 wt% magnetite ( $\text{Fe}_3\text{O}_4$ ), and 1-3 wt% salicylic acid chromium chelate. The same sphere was used for all experiments and imaged with contact AFM showing no large asperities and having a spherical cap of radius  $5.3\ \mu\text{m}$ .

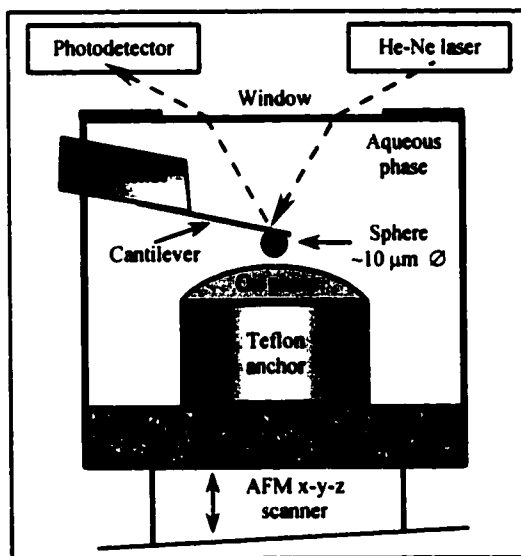


Figure 3.1: Schematic of AFM oil droplet probing with liquid cell. Not to scale.

A Teflon tube (ID = 2.25 mm) serves as a reservoir and anchor for the oil phase drop (n-hexadecane or oil/surfactant) under water (Fig.

3.1). A commercial agglomerating (densification) agent (product #225 from Betz Paperchem, Inc., Jacksonville, FL) for toner-printed paper recycling was used for the oil/surfactant. It consists of 60% simple aliphatic oils ( $\text{C}_9$ - $\text{C}_{12}$ ) and 40% low HLB (hydrophile-lipophile balance) surfactants that remain almost exclusively in the oil phase. It should be noted that the Betz products require elevated temperatures for maximum performance, but only room temperature comparisons are being made with these AFM experiments since the scanner operating conditions are thus restricted. The water used was reverse-osmosis deionized and twice-distilled (3D) with a conductivity equivalent to  $\sim 10^{-5}$  M NaCl, and thus an approximate Debye length ( $\kappa^{-1}$ ) of 96 nm. The cationic starch solution is prepared by boiling 0.1 wt% STA-LOK 400 in 3D water for 30 minutes and has a conductivity equivalent to  $3 \times 10^{-4}$  M NaCl ( $\kappa^{-1} = 18\ \text{nm}$ ). STA-LOK 400 (A. E. Staley Co., Decatur, IL) is a commercial brand polyelectrolyte similar to cationic starches present in many papers. The starch is a mixture of highly branched amylopectin ( $10^7$ - $10^8$  mol. wt.) and linear amylose ( $10^5$ - $10^6$  mol. wt.) derivatized with quaternary ammonium groups every 30-35 glucose units providing the positive charge in aqueous solution. These cationic groups

adsorb, perhaps even irreversibly, to the negative surfaces of toner particles and oil-aqueous interfaces. From dynamic light scattering, an adlayer thickness of 33 nm was determined for n-hexadecane droplets dispersed in water, while an adlayer thickness for toner was estimated from poly(styrene) spheres as 49 nm.<sup>25</sup>

The liquid cell mounts to the AFM scanner using piezoelectric transducers to move the sample (oil interface) relative to the probe (toner). The attractive or repulsive forces acting on the toner probe while near the oil interface deflects the cantilever down or up, respectively. The interface also deforms as a result of long-range interactions and physical contact with the impinging particle. The linear displacement of a He-Ne laser reflecting from the back of the cantilever is followed with the aid of a position-sensitive photodetector for a direct measurement of colloidal interaction force. The stiffness of the cantilever is characterized by a Hookean spring constant so that the force is linearly proportional to measured deflection, typically in the range of  $\mu\text{N}$ - $\text{pN}$ .

AFM force-distance profiles are qualitatively compared to the events captured in digital images of interfacial deformations at equilibrium conditions. A larger toner particle (100  $\mu\text{m}$  diameter) glued to the end of a long, glass capillary is manually maneuvered with a micro-manipulator. The oil phase is again anchored under water similarly to the modified AFM liquid cell. An optical microscope with a long working distance (Wild Makroscope), digital video camera, computer, and frame grabber using NIH Image allowed gray scale imaging of the toner particle and the oil/water interfaces. These images provide confirmation for the interpretations of the AFM force profiles.

Forces and induction times are reproducible to within a few percent. With the understanding that one of the overall end goals of this work is to determine the actual separation between sphere and drop indirectly with AFM, the results of this chapter are given with relative position based on the scanner displacement alone. With mutually deforming oil/water interface and cantilever, the AFM cannot measure the film thickness. Also, since the measurements in this chapter are purposefully dynamic to mimic collisions in a paper repulper, there can be no meaningful discussion of equilibrium surface forces, as will be considered in great detail in the following chapters.

### 3.4 Results and Discussion

Figure 3.2 is a crude representation of the expected differences between force profiles for oil-toner in pure (3D) water (A) and 0.1 wt% aqueous cationic starch (B). The horizontal line is the undeflected cantilever signal (no interaction force) at large oil-toner separations. There is a rapid increase in force,

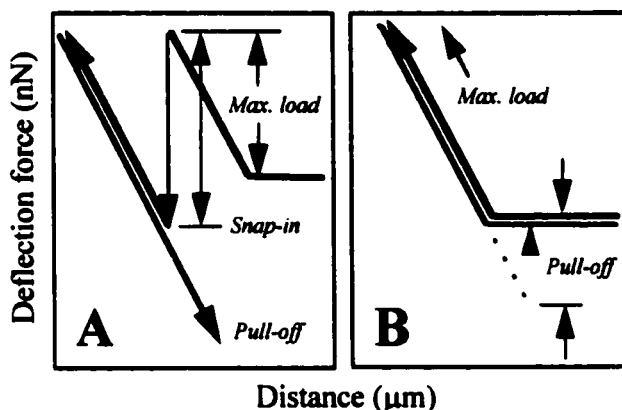


**Figure 3.2:** Generic force curves of polymer sphere interactions with oil-aqueous interfaces: (A) pure water, (B) cationic starch.

most likely dominated by hydrodynamics, approaching the oil interface. The viscous repulsion of the squeezed intervening fluid increases at fairly constant compliance (slope) up to some maximum load at film rupture. When the particle snaps into the oil, the oil/water interface forms a three-phase line (TPL) rapidly engulfing the toner until the dynamic advancing oil contact angle is achieved. The duration of the compliance regime before snap-in (wetting) is equated with the induction time defined earlier: the aqueous film thins, ruptures, and forms a TPL.<sup>85</sup> Advancing the particle after film rupture gives nearly linear compliance since the changes in TPL perimeter and angle relative to the displacement change very slightly. Removing the toner particle from the interface requires extremely large displacements to break the capillary neck.

Cationic starch adlayers should stabilize the interface such that the approach curve is monotonically repulsive and similar to the pull-off trace force positive force unloading (Fig. 3.2 B). The attractive snap-in will be gone since the electrosteric adlayers hold the interfaces apart. The compliant drop will simply deform indefinitely away from the impinging particle, maintaining a nearly constant separation after the adlayers contact—that is, once the steric interaction dominates the double-layer and hydrodynamic forces which are also repulsive. The hydrodynamic repulsion becomes negligible but not zero as the interface continues to wrap

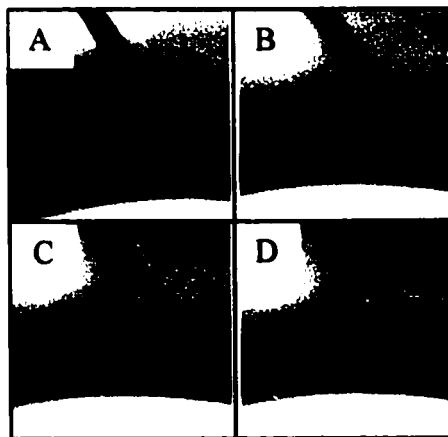


**Figure 3.3:** Toner sphere (100  $\mu\text{m}$ ) in water: (A-C) approaching oil, (D) wetted by oil.

hydrodynamic repulsion becomes negligible but not zero as the interface continues to wrap

around the particle bringing more interfacial area into constant separation, for an enlarging film of uniform thickness.

The large toner sphere attached to a glass capillary in the digital images of Fig. 3.3 approaches n-hexadecane in pure water (images A-C) and the wetted equilibrium condition is shown in image D. The sphere is engulfed to nearly its equator but still shows a relatively high oil contact angle when the capillary is relaxed. If the contact angle were very low, the particle should be completely engulfed when the capillary's action against the surface tension is relieved.

The corresponding pull-off sequence is shown in Fig. 3.4 with reversed lighting contrast to indicate the oil lens that detaches with the toner, seen as a bright spot. Image D was taken the instant after the capillary neck snaps and the final separation is  $\sim 200 \mu\text{m}$  which emphasizes not only the strength of the capillary force but the high deformability of the interface.

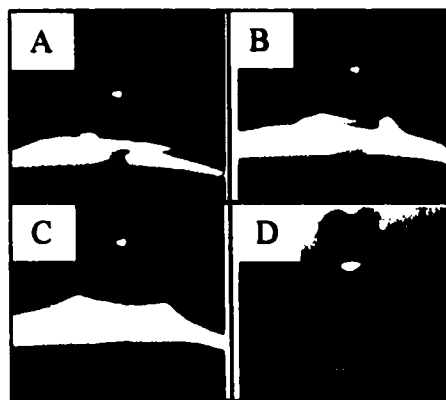


**Figure 3.4:** Inverse lighting contrast of toner in water: (A) wetted sphere, (B & C) capillary neck, (D) pull-off oil residue.

The nonwetting behavior of the oil in aqueous cationic starch against starch-covered toner is obvious from the sequence of images in Fig. 3.5. The large

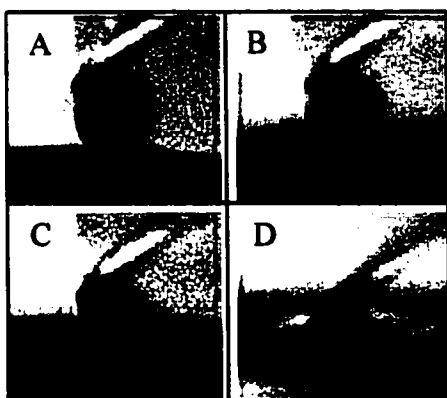


**Figure 3.5:** Toner sphere in 0.1 wt% aqueous cationic starch: (A) close oil approach, (B) initial contact, (C & D) strong monotonic repulsion.

dimpling of the oil surface (beginning in image B) caused by the impinging particle is extremely stable against rapid collisions (image D). No spontaneous wetting by the oil is visible: there is no snap-in or capillary neck formation. The amazing strength of the adlayer/oil interface is pronounced by the depth of the depression ( $\sim 100 \mu\text{m}$ ). When the surfaces are left in contact for several seconds—much longer than would be experienced in separation processes or AFM experiments—there is often a weak attachment, indicated by a thin neck visible only during rapid retraction. The instability of these weak necks suggest

they could be explained by hydrodynamics alone (see Chapter 6, Figs. 6.7 & 6.8).

The AFM allows a more quantitative and reproducible means of conducting similar experiments using a smaller toner particle. The highest scanner velocity possible was used ( $30 \mu\text{m/s}$ ), giving a dynamic draining condition and the largest range of displacement for force profiling. The actual relative film thinning rate are not accessible but are significantly less than during rupture. The viscous forces dominate at close approach (Fig. 3.6) before the expected long-range hydrophobic<sup>26,41,59</sup> (for more see Section 2.2) and van der Waals attractions can precipitate contact. The various surface forces in operation influence the induction time but are not themselves independently observable in these experiments designed for dynamic interactions, not equilibrium forces. The

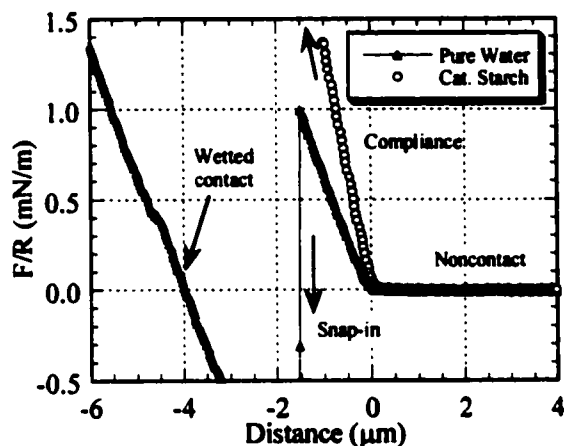


Figure 3.6: Oil-toner interaction normalized by sphere radius: mean velocity  $30 \mu\text{m/s}$ , arbitrary origin centered at onset of repulsion.

significantly smaller slope of the pure water compliance line prior to film rupture implies either the film, the liquid interface, or both are “softer” than when the adlayers are present. The interfacial tension is not measurably affected by the starch, but the hydrodynamic boundary conditions (i.e., slip length) could be very different between the two scenarios. The much larger Debye length in 3D water would present a softer film since the thicker electrical double-layer would compress more for a given increase in applied force. Another factor complicating the quantitative analysis is the drop curvature. The stiffness of the interface increases with decreasing radius resulting from Laplace pressure inside the drop. This issue was later determined to be of critical importance and is addressed in detail in Chapter 5.

Even though the rate and sensitivity of data acquisition cannot reveal DLVO forces with any certainty, the compliance regimes are clearly not linear during approach (Fig. 3.6). The slightly increasing slope contains a convoluted data set of interfacial deformation, surfaces forces, and hydrodynamic drainage. After the snap-in, the cantilever deflection continues below the limits of the detector but resumes a nearly linear compliance for the TPL regime after advancing  $\sim 1 \mu\text{m}$  to relax the system. The magnitude of the pull-off forces could not be measured with the AFM but can be roughly estimated from the distance traveled by the stepper motors ( $\sim 50 \mu\text{m}$ ) to detach the probe. These large cantilever deflections are no longer in the

Hookean regime of the material or within the small angle approximation for the laser beam reflection technique. This relatively huge capillary force indicates that the radius of the TPL perimeter is approaching that of the toner particle. The same toner particle approaching oil in 0.1 wt% aqueous cationic starch is monotonically repulsive, as anticipated, up to more than 20 nN load (Fig. 3.6)—again beyond detector limits. Film rupture was never observed in the presence of cationic starch. This further supports failed coalescence in oil and toner agglomerating processes due only to the presence of adsorbed polyelectrolyte.

The induction time is typically used as an indicator of successful particle-bubble or particle-drop attachment in flotation and oil-assisted agglomeration, respectively.<sup>85-90</sup> This first report of induction time from AFM measurements is typical of those found by other methods for mineral particles and air bubbles. In the oil/3D water system, the induction time for the toner was 52 ms, at an average film rupture load of 5.6 nN with particle entry greater than 330 nm (Table 3.1). The estimates of snap-in distance are calculated from cantilever deflection and force only. The particle entry is probably much greater than this due to interfacial displacement, but the measurement also includes whatever long-range snap-in distance was traversed. The cationic starch delayed interfacial rupture indefinitely beyond 191 ms (the length of the compliance regime in the AFM experiment) for loads above 77 nN; however, the optical studies imply far greater stability limits.

**Table 3.1: AFM interaction measurements: reported intervals show 90% confidence.**

<b>Interface</b>	<b>Induction Time (ms)</b>	<b>Maximum Load (nN)</b>	<b>Snap-in Force (nN)</b>	<b>Snap-in Distance (nm)</b>
Oil/water	52 ± 7	5.6 ± 0.6	> 16.6	> 330
oil/cationic starch	> 191	> 77	≤ 0	≤ 0
Betz 225/water	133 ± 26	0.7 ± 0.16	3.5 ± 0.57	> 70
Betz 225/cat. starch	151 ± 47	1.4 ± 0.16	2.5 ± 0.18	> 50

Significant amounts of starch also adsorb to an oil-surfactant blend (Betz #225) droplet in water; but here, the starch is imbibed into the oil phase presenting no adlayer for electrosteric stabilization against toner attachment.<sup>25</sup> When the pure oil (hexadecane) is replaced with the oil/surfactant blend, the induction time measured with AFM increases to 133 ms at loads around 0.7 nN (lower because of decreased interfacial tension). The snap-in is much smaller in force (3.5 nN) but probably even larger in distance than that for the pure oil system. Again, optical images are invaluable in showing that the particle is all but completely engulfed this time (Fig.

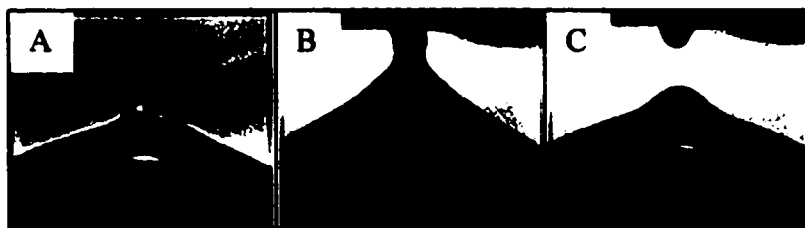


**Figure 3.7:** Toner engulfment in oil/surfactant under water (A). Extensive detachment necking (B) and slow viscous recovery of oil-water interface.

3.7 A). The significantly lower interfacial tension of the oil-surfactant with water gives a lower oil contact angle and forms a weaker capillary neck that is stable even at very long extensions (Fig. 3.7 B). Due to high viscosity, the bulk oil/surfactant does not have enough time to flow with the advancing TPL at high velocities, as is evidenced by the image of the releasing neck in Fig. 3.7 C. It takes several seconds for the interface to return to constant curvature after pull-off since the ratio of viscous force to surface tension force is much larger here than for n-hexadecane/water. Even though the toner is wetted by the oil/surfactant, the snap-in recorded with AFM is small since there is insufficient time for complete engulfment of the particle. The rheological behavior of this system deviates from that of an oil-surfactant emulsion in water.

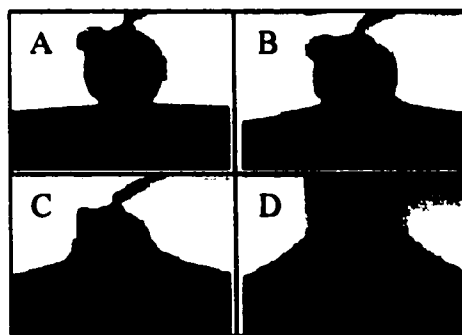


**Figure 3.8:** Toner (A) approaches oil/surfactant in 0.1 wt% cationic starch: (B) initial wetting, (C) slow viscous engulfment, (D) pull-off necking.

Cationic starch addition has reduced effect on oil-surfactant/toner coalescence (Table 3.1) agreeing with observations of the oil-surfactant's ability to imbibe the starch adsorbed to both toner and oil. The induction time and load are slightly elevated with a smaller snap-in, suggesting that the starch may still be working against complete wetting of the toner. Fig. 3.8 captures the initial wetting (B) and the equilibrium engulfment (C) of the toner particle when it contacts the oil/surfactant in aqueous cationic starch. Compared to the equilibrium wetting configuration in pure water (Fig. 3.7 A), the presence of adsorbed starch appears to be successful at halting the advancing oil/surfactant sooner. This might suggest that the contact angles are not the same, but this is contrary to previously reported contact angles (Table 3.2).<sup>91</sup>

**Table 3.2:** Comparison of snap-in force from AFM with static advancing oil contact angle under water or 0.1 wt% aqueous cationic starch.

<b>Interface Type</b>	<b>Snap-in Force (nN)</b>	<b>Contact Angle (<math>\theta^\circ</math>)</b>
oil/water	> 16.6	60°
oil/cationic starch	$\leq 0$	95°
Betz 225/water	3.5	15°
Betz 225/cationic starch	2.5	15°

### 3.5 Conclusions

While these single-particle AFM measurements in oil/water/toner systems specifically illuminate the consequences of cationic starch in halting oil-toner coalescence and the countering effect of oil surfactant addition, perhaps the more impressive conclusion is the feasibility of measuring colloidal scale interactions with highly deformable interfaces directly and quantitatively. Steric stability imparted by adsorbed macromolecules under dynamic film drainage conditions was recorded and rated by induction times and maximum applied loads. A good qualitative comparison is made between the AFM snap-in forces and advancing oil contact angles measured against toner under water (Table 3.2). The oil drop with an adlayer of starch did not wet the toner under water ( $\theta = 95^\circ$ ), and the analogous interface was completely stable to rapid dynamic collisions and approximately static contacts (no film rupture).

The many complications of variant interfacial systems become apparent, especially for comparing oil interactions to the Betz product #225 whose interfacial tension is negligible and rheology complex. In pure water, both oil phases wet the toner, but a naïve comparison of snap-in to contact angle is not at all helpful in the quantitative interpretation of force-distance profiling. And the difficulty goes far deeper than surface tension and viscosity, to the fundamentally different film thinning behavior governed by surface forces, hydrodynamics and interfacial deformation.

What follows are investigations into these areas that will open the door leading to detailed inspections of liquid/liquid/solid interactions. The next Chapter explores the illusive hydrophobic force to help delineate between true hydrophobic interactions and other specific long-range attractions. Section 2.2 addressed the extant literature on this topic, while Chapter 4 provides a meticulous study to establish a reference for further exploring the interactions of oil-droplets with other hydrophobic materials. Chapter 5 then develops the method for following

34

**interfacial deformation in theory to understand the quantitative relationship between AFM measures of distance and the actual separation between a liquid drop (or bubble) and a sphere.**

## CHAPTER 4:

### LONG-RANGE ATTRACTIONS BETWEEN SILANATED SILICA EXAMINED BY AFM ELECTROLYTE TITRATIONS

#### 4.1 Summary

A parametric study of electrostatic and hydrophobic forces with changing electrolyte concentration shows characteristic features in dynamic cantilever snap-in from which the hydrophobic interaction can be assessed. A relatively simple and efficient experimental procedure for determining the strength and range of the hydrophobic effect is accomplished in the sphere-plate geometry between silanated glass and quartz by a systematic electrolyte titration of electrostatic forces. Snap-in distance, acquired with atomic force microscopy (AFM), plotted against electrolyte concentration shows a minimum at some identifying intermediate salinity and a plateau at high concentrations. These prominent features, distinguishable from an adequate database represented by a single titration curve, facilitate deconvolution of the hydrophobic force from other interactions. Monovalent electrolyte concentration does not appear to affect the hydrophobic interaction directly between  $10^{-4}$  and  $10^{-1}$  M, but evidence of an independent and long-range electrostatic correlation force is observed.

#### 4.2 Background

Long-range attractions observed between non-polar interfaces in aqueous media that are not explained by the DLVO theory<sup>11</sup> have long been grouped under the single heading of hydrophobic effect (see Section 2.2). Numerous publications collectively suggest that a single mechanism, though desirable for its simplicity and elegance, is not reasonable to explain the different long-range and “hydrophobic” forces observed and substantiated.<sup>27-30,39</sup> An extensive review of the literature also reveals a certain lack of sufficiently thorough experimentation to provide satisfactory evidence for or against proposed hydrophobic interaction mechanisms.

The techniques available for measuring long-range colloidal attractions directly<sup>92,93</sup> all suffer from inherent system instabilities, requiring that new methods be developed. Rather than

exerting an external, mechanical force to counterbalance the attraction via the AFM cantilever, a contrasting methodology manipulates some repulsive interparticle force *in situ* and independently from the interaction of interest, or at least in a manner such that any coupled effects are understood and predictable. The electrostatic double-layer force can be comparable in magnitude to the hydrophobic attraction and is the most likely candidate for a tunable interaction. Systematic adjustments of the ionic strength affect the force balance, allowing the hydrophobic contribution to be quantified from the theoretical fitting of force profiles or titration curves (snap-in distance vs. electrolyte concentration).

In the present work, the objective is to determine the strength and range of the hydrophobic effect between stable, robust surfaces from AFM snap-in distances acquired during a careful titration of electrostatic forces. An adequate database compiled for reasonably well-defined surfaces might even distinguish different types of non-DLVO interactions occurring. It is hoped that a quantitative characterization can be accomplished when appropriately accounting for electrostatically screened interactions, even in the case where the hydrophobic effect is directly affected by the presence of ions. Therefore, a computational parametric study of electrostatic and hydrophobic forces is conducted to identify any characteristic trends with changing electrolyte concentration from which the hydrophobic interaction might be assessed. Finally, colloidal probe AFM is used to measure local surface forces and adhesion in aqueous solutions between glass or fused quartz plates and glass spheres rendered hydrophobic by vapor silanation and compared with the computational results.

### 4.3 Experimental Methods

Fused quartz plates from G. M. Associates, Inc., Oakland, CA, were first cut to size for sample tabs, rinsed with acetone to remove the bulk of organic contaminants, and dried. Contact AFM images  $5 \times 5 \mu\text{m}^2$  taken in air with an AutoProbe® CP from Park Scientific Instruments had average rms surface roughness of 1 nm;  $1 \times 1 \mu\text{m}^2$  gave 0.7 nm;  $0.4 \times 0.4 \mu\text{m}^2$  gave 0.4 nm with peak-to-valley maximums of a few nanometers (Fig. 4.1). A weak silicon nitride cantilever with a sharp tip (nominal radius  $\sim 20$  nm) was used for all imaging. The quartz was soaked overnight in a 1:1:8 by weight solution of ethanol:potassium hydroxide:water (EtOH-KOH), after which it was thoroughly rinsed with deionized and twice distilled (3D) water with specific conductivity

of  $9 \times 10^{-7} \Omega^{-1} \text{cm}^{-1}$ , and dried by heating. Similarly cleaned quartz and glass plates consistently show water contact angles of less than  $5^\circ$  for the first hour after drying.

Glass microspheres for particle-size standards were obtained from Duke Scientific Corp., Palo Alto, CA, with mean diameter  $8.2 \pm 0.8 \mu\text{m}$ . A single as-received replaces the sharp imaging tip of the cantilever ( $k = 0.05 \text{ N/m}$  nominally, Park Scientific Instruments, Sunnyvale, CA). A three-dimensional micro-manipulator stage with flame-drawn glass capillaries was used to apply epoxy and then attach the sphere to the cantilever under the view of a Wild Makroscope M420. After curing, the cantilever assembly was cleaned in a stream of acetone to remove epoxy residue and other adsorbed oils, and thoroughly rinsed with 3D water. EtOH-KOH cleaning proved too aggressive for AFM cantilevers and epoxy, removing the reflective gold coating and sphere after repeated washing. Surface roughness was estimated to be 6 nm from AFM images of the spherical cap region that would be interacting with the substrate. Arc and chord lengths from these images also confirmed the diameter of the sphere. The radius of curvature  $R_s = 4.1 \mu\text{m}$  was used for all figures and calculations.

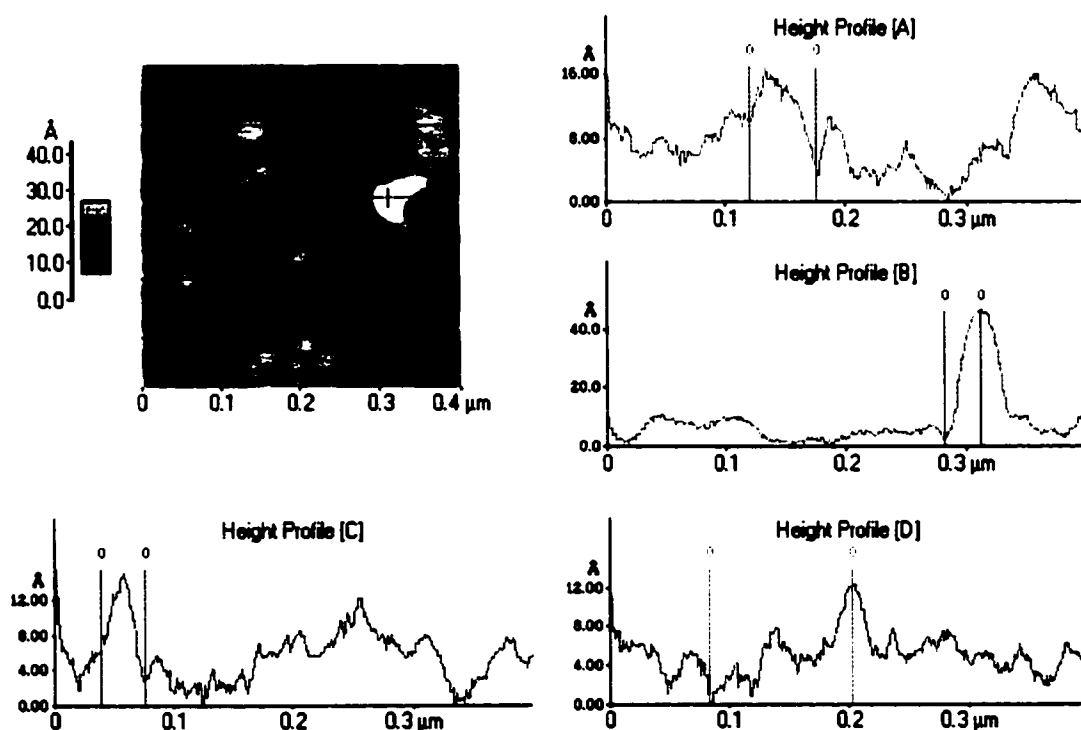


**Figure 4.1:** Contact AFM image ( $400 \times 400 \text{ nm}^2$ ) of cleaned quartz plate: rms surface roughness 0.43 nm, average roughness 0.28 nm, peak-to-valley max 5.6 nm. Profile statistics reported in Table 4.1.

**Table 4.1:** Dimensional data taken from cross-sectional traces of Fig. 4.1. Values of  $\Delta$  are measured between the markers of each profile.

<b>Line</b>	<b><math>\Delta</math>Height (nm)</b>	<b><math>\Delta</math>Distance (nm)</b>	<b><math>R_p-v</math> (nm)</b>	<b>rms (nm)</b>	<b><math>\langle</math>Height<math>\rangle</math> (nm)</b>
A	0.67	56.5	1.70	0.39	1.06
B	4.47	29.8	4.66	1.03	1.39
C	0.46	37.6	1.56	0.31	1.07
D	1.25	119.0	1.40	0.22	1.06

Cleaned samples and probes were immediately enclosed in an atmosphere saturated with octyltriethoxysilane (OTES) (Silquest A-137 Silane, OSi Specialties, Irvine, CA) vapor at approximately 65°C for 2 hours. Trialkoxysilane reactions with surface hydroxyl groups in the presence of water, assumed to be relatively abundant at silica surfaces in air, suffer from competitive self-condensation. In spite of this, triethoxysilanes are desirable because they graft more strongly to silica surfaces than other functional silanes including the commonly used octadecyltrichlorosilane.<sup>94</sup> The silanated surfaces were rinsed with ethanol and dried for 24 hours at 65°C. Treated quartz showed 85-95° static advancing contact angles when cleaned with EtOH-KOH and as low as 78° for quartz cleaned only with acetone. Pre-cleaned glass slides (VWR Scientific Inc.) were also rinsed with acetone or EtOH-KOH followed by vapor silanation, giving contact angle ranges of 73-90° and 80-84°, respectively. Thus, the contact angle on the silanated glass spheres was assumed to be around 80°. The ranges of contact angles are believed to reflect some variation in surface hydrophobicity rather than being completely explained by experimental error alone. While the silane film thickness is not known, AFM images indicate complete coverage and probe indentations suggest they are at least 10-20 nm.

Smaller glass spheres ( $1.6 \pm 0.3 \mu\text{m}$ ), also from Duke Scientific Corp., were stirred for 40 hours in a 1 mM OTES in pure ethanol for a maximum coverage of approximately 100 monolayers if all the silane was crosslinked to the spheres. The zeta-potential measurements in a Rank Brothers Mark II Microelectrophoresis Apparatus of the glass spheres in  $10^{-3}$  M  $\text{NaNO}_3$  ( $\text{pH} \approx 5.5$ ,  $T = 25^\circ\text{C}$ ) gave  $-45$  mV as-received and  $-35$  mV after silanation using the Helmholtz-Smoluchowski equation, and these values are used as estimates for the isolated surface potentials of the glass probes. The decreased zeta-potential might be completely explained by an increased separation between the Stern and slip planes if the hydrocarbon film is sufficiently thick. On the other hand, it might be insightfully indicative that silanation can change surface potential by

chemically modifying enough of the potential-determining surface sites, contrary to the usual assumption.<sup>11,44,95</sup>

**Table 4.2:** Dimensional data taken from cross-sectional traces of Fig. 4.2. Values of  $\Delta$  are measured between the markers of each profile.

Line	$\Delta$ Height (nm)	$\Delta$ Distance (nm)	Rp-v (nm)	rms (nm)	<Height> (nm)
A	0.05	28.2	3.46	0.74	1.70
B	0.14	28.2	2.35	0.48	1.70
C	0.03	43.9	3.61	0.77	1.70
D	0.03	26.7	2.72	0.62	1.70

The surface roughness is slightly increased after treatment with OTES, revealing a few more large clumps, presumably reacted silane aggregates, 2-5 nm in height.<sup>94</sup> For a  $5 \times 5 \mu\text{m}^2$  area taken in air the rms surface roughness was 4 nm;  $1 \times 1 \mu\text{m}^2$  gave 0.8 nm;  $0.4 \times 0.4 \mu\text{m}^2$  gave 0.5 nm with peak-to-valley maximums similar to quartz (Fig. 4.2). But the greatest difference in

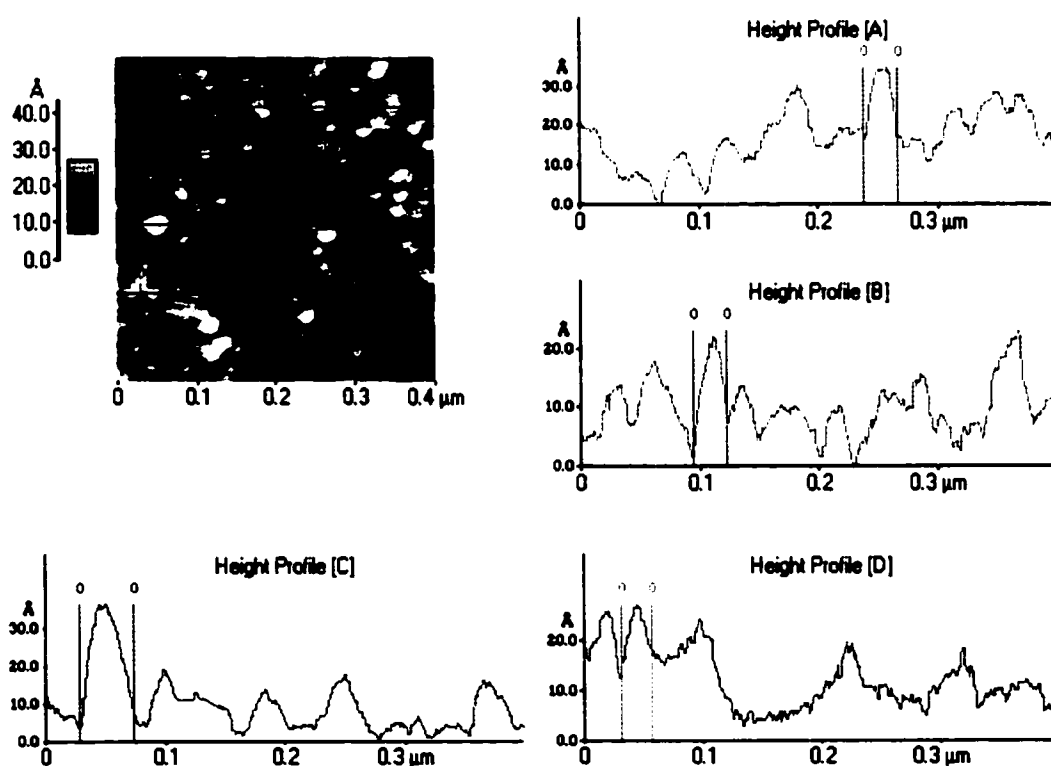


**Figure 4.2:** Contact AFM image ( $400 \times 400 \text{ nm}^2$ ) of cleaned quartz plate: rms surface roughness 0.43 nm, average roughness 0.28 nm, peak-to-valley max 5.6 nm. Profile statistics reported in Table 4.2.

topography is the more pronounced globular domains on the OTES-modified quartz seen in micrographs that are absent from the bare quartz images (compare Figs. 4.1 and 4.2). These fairly regular structures about 30 nm in diameter appear to be only a few nanometers high, though tip convolution with the topography does not allow definitive dimension measurements. Similar silane layers have been investigated<sup>66,94,96</sup> and are believed to be formed from small clusters of silane molecules that cross-link with each other before attaching to the substrate.

Force vs. separation profiles were computed for hydrophobic silica plates and microspheres in aqueous media, and force-distance measurements were made at 140 nm/s using a pendent-drop liquid cell and vinyl fluid reservoir. This particular AFM uses a laser reflected to a split photodiode to detect cantilever deflections independent of scanning the substrate. The equilibrium force exerted on the cantilever is calculated as the product of its deflection and the spring constant,  $k_c$ . The actual stiffness of cantilevers used here ( $k_c = 56 \pm 0.2$  mN/m) was confirmed through individual calibrations by adding tip mass and measuring the change in resonance frequency<sup>97</sup> (see Appendix A). Force values are often averaged over several random locations, each sometimes giving significantly different local forces for the same substrate. Enough randomly chosen data points are expected to give average snap-in distances and pull-off forces that agree with relative trends in macroscopically-averaged surface energies as observed from contact angle measurements. A single-location electrolyte titration experiment measured quantitative changes in force, independent of surface energy variations along the substrate, while altering salt concentration. Concentration changes were made every 20 minutes, and the liquid cell had no means of circulation other than that induced when adding or removing solution.

#### 4.4 Results

Parametric studies were conducted first varying the plate surface potential,  $\psi_{1\sigma}$  to predict the snap-in distance of the sphere-cantilever as a function of electrolyte concentration for constant potential surfaces, considering only DLVO forces and hydrophobic terms fitted at high salt (Figs. 4.3 and 4.4). A typical range for silica surface potentials was used in the plots with the sphere surface potential,  $\psi_{2\sigma}$ , being either the silanated or bare glass zeta-potential. The DLVO model for a sphere and plate geometry used here is the sum of the non-retarded van der Waals equation with a hard wall term (Eq. 4.1) and the electrostatic double-layer interaction. The parameter  $r_0 = 0.16$  nm is essentially universal as a limit for closest separation of two atoms

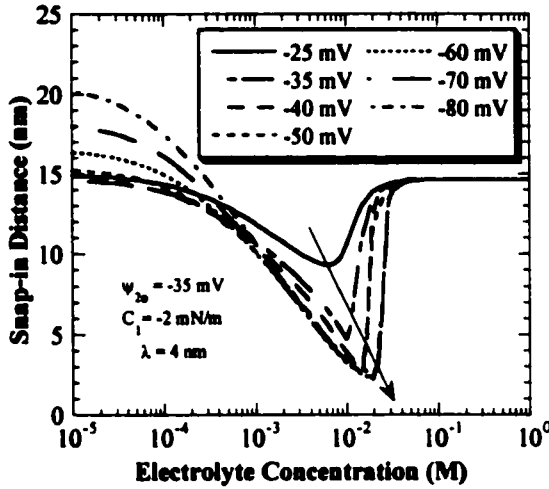


**Figure 4.3:** Profiles of theoretical snap-in distance for given  $\psi_{1o}$  with fixed  $\psi_{2o}$  for hydrophobic silica sphere and plate in monovalent electrolyte solutions:  $k_c = 0.056$  N/m (snap-in force gradient).

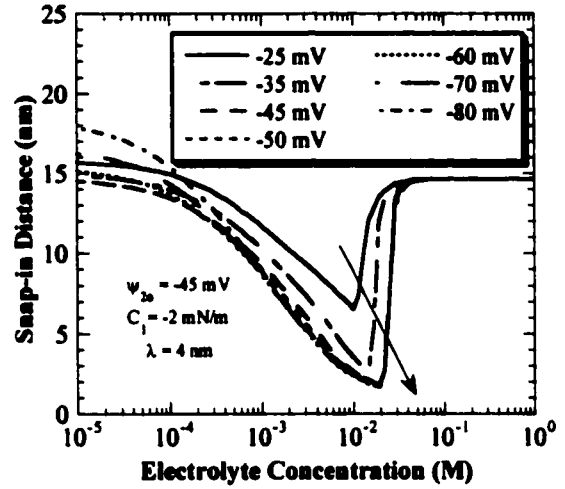


**Figure 4.4:** Profiles of theoretical snap-in distance for given  $\psi_{1o}$  with fixed  $\psi_{2o}$  for hydrophobic silica sphere and plate in monovalent electrolyte solutions, similar to Fig. 4.3.

and the Hamaker constant,  $A$ , is basically unchanged whether the surfaces are assumed to be fused quartz ( $8.3 \times 10^{-21}$  J) or hydrocarbon ( $\sim 10^{-20}$  J):<sup>26</sup>

$$\frac{F_{whw}}{R_s} = \frac{A}{6} \left( \frac{1}{D^2} - \frac{r_o^6}{D^8} \right). \quad (4.1)$$

Program code for MATLAB<sup>®</sup> 5 was written to evaluate the equations tabulated by McCormack *et al.* numerically for calculating the double-layer energy formulated with the non-linear Poisson-Boltzmann equation<sup>82</sup> and the Derjaguin approximation for a sphere and plate made without restriction on the magnitudes of constant surface potential or constant surface charge density boundary conditions (see Appendix B). These results compare very well to those from the Debye-Hückel approximation for dissimilar surface potentials.<sup>11</sup>

$$\frac{F_h}{R_s} = C_1 \exp\left(\frac{-D}{\lambda}\right). \quad (4.2)$$

The exponential form of the hydrophobic interaction with pre-factor  $C_1 = -2$  mN/m and decay length  $\lambda = 4$  nm (Eq. 4.2) is assumed to be independent of electrolyte concentration.

When at least one surface does not maintain a constant charge density, double-layer forces may precipitate dynamic snap-in at low electrolyte concentrations before a shorter-ranged hydrophobic or van der Waals attraction can. A larger difference between  $\psi_{1o}$  and  $\psi_{2o}$  increases the snap-in distance at low concentrations, but an interesting, non-monotonic behavior of snap-in becomes apparent at intermediate concentrations for modest hydrophobic strength and range. The forces compete most strongly where the Debye length and hydrophobic decay length are of similar magnitude, while the electrolyte-independent hydrophobic interaction is responsible for the snap-in plateau at higher concentrations. This is manifested as a minimum snap-in distance at some intermediate electrolyte concentration. The minimum is smaller and shifted to higher concentrations with increasing surface potential,  $\psi_{1o}$ , but the effect levels off quickly as  $\psi_{1o}$  becomes substantially higher than  $\psi_{2o}$ . The maximum electrostatic repulsion is determined by the lower potential; therefore, the minimum snap-in is more sensitive to the lower surface potential but also to the hydrophobic parameters. Figures 4.5 and 4.6 show parametric studies for the hydrophobic pre-exponential,  $C_1$ , and decay length,  $\lambda$ , of moderate magnitudes for fixed surface potentials of  $-60$  mV and  $-35$  mV. A surface potential of  $-60$  mV is quite reasonable for silica materials and seems to be the best value for fitting our profiles in the end analysis.

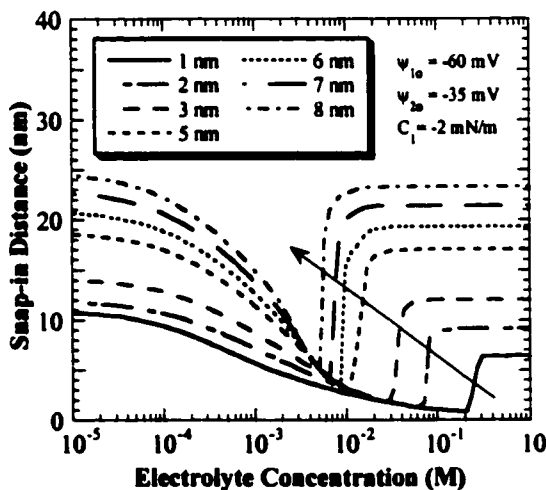


Figure 4.5: Parametric study of hydrophobic decay length  $\lambda$  predicting snap-in distance of hydrophobic silica sphere and plate.

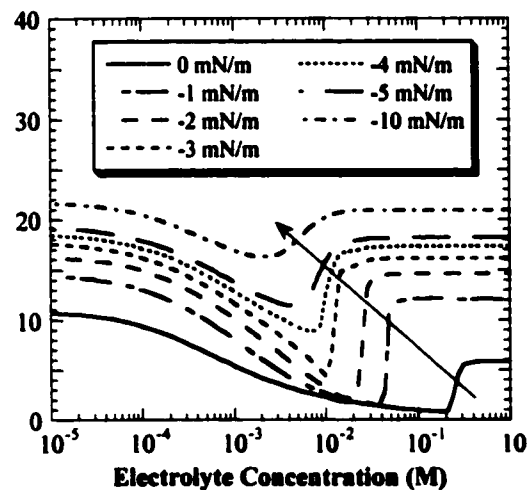


Figure 4.6: Complimentary parametric study (Fig. 4.5) of hydrophobic pre-factor  $C_1$  predicting snap-in distance for  $\lambda = 4$  nm.

The minimum snap-in distance could be used as an identifying marker in a salt titration experiment where two or more force parameters are unknown and equilibrium force-profiles are unavailable to fit these parameters independently. The minimum snap-in along with the snap-in

plateau at high salt form a unique data group, strictly speaking, for a given set of DLVO interactions that determines the strength and range of the hydrophobic force. This is not necessarily true for any combination and magnitude of interactions, but this sort of titration sensitivity could possibly be generalized for other systems to quantify force parameters by a unique fit of identifying data points.

Two different force-profiling procedures have substantiated that the long-range attraction between hydrophobized silica surfaces is significantly reduced around a concentration of  $10^{-2}$  M NaCl and NaNO<sub>3</sub> compared to the interactions above and below this concentration. The snap-in distances and pull-off forces taken from AFM force-distance profiles are reported for the hydrophobic glass sphere and plate system in aqueous NaCl solutions (Table 4.3).

**Table 4.3:** AFM snap-in distances and pull-off forces from force profiles of hydrophobized glass plate and sphere under electrolyte: 95% confidence intervals reported.

Aqueous Solution	Snap-in (nm)	Pull-off (mN/m)
$10^{-4}$ M NaCl	$27 \pm 3.0$	$2.0 \pm 0.12$
$10^{-3}$ M NaCl	$23 \pm 3.0$	$1.8 \pm 0.15$
$10^{-2}$ M NaCl	$\sim 0$	$0.9 \pm 0.32$
$10^{-1}$ M NaCl	$13 \pm 1.5$	$2.9 \pm 0.27$

Approaching force profiles for each salt concentration shown in Fig. 4.7 are compared to model fits using DLVO and hydrophobic equations:  $A = 10^{-20}$  J, constant surface potentials  $\psi_{10} = -60$  mV,  $\psi_{20} = -35$  mV,  $C_1 = -2$  mN/m,  $\lambda = 4$  nm. Exact fits for each curve are possible with slight adjustments to the surface potentials used, showing only slight deviations from our constant surface potential assumption. Attraction between the silanated glass sphere and plate (interpreted from snap-in distances) decreased when the aqueous medium changed

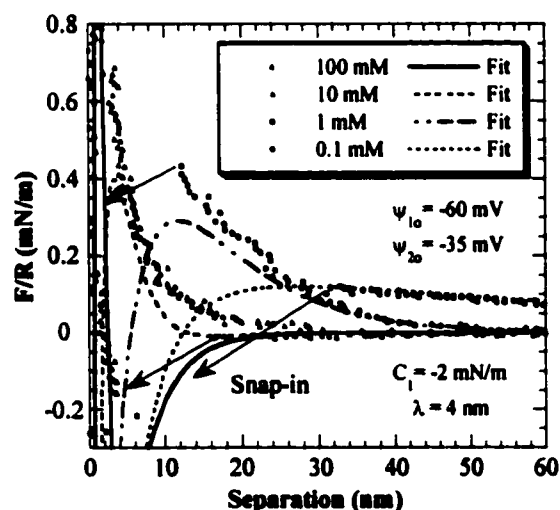


**Figure 4.7:** Force-separation profiles for silanated glass sphere and plate in aqueous NaCl. Fitted with DLVO and hydrophobic equations.

from  $10^{-4}$  to  $10^{-3}$  M NaCl, and was again less for  $10^{-1}$  M. At the intermediate concentration of  $10^{-2}$  M, the approach curves were monotonically repulsive and weak adhesion was achieved showing a similar trend with ion concentration to the parametric studies of Figs. 4.3 and 4.4. Pull-off forces were always independent of loading in these experiments.

A second procedure was followed in order to reduce or completely remove considerations of local topography and surface energy variances along the substrate that complicated the interpretation of force-distance measurements in the first procedure. AFM probing was conducted at a single location while injecting electrolyte solution or 3D water at intervals to alter the salinity. This single-location titration experiment is capable of measuring quantitative changes in force, independent of surface variations on the scale of the probe contact area, and facilitates more convenient concentration adjustments (Fig. 4.8). Again, the attraction decreased to a minimum at  $\sim 10^{-2}$  M  $\text{NaNO}_3$ . The attraction was significantly stronger and roughly constant at higher concentrations up to  $10^{-1}$  M. Electrolyte concentrations are not known exactly in the titration experiment because of water evaporation from the cell.

Adhesion values inferred from JKR theory<sup>26,98</sup> (simply the pull-off force normalized by  $2\pi R$ ) are as much as two orders of magnitude smaller than average literature results for

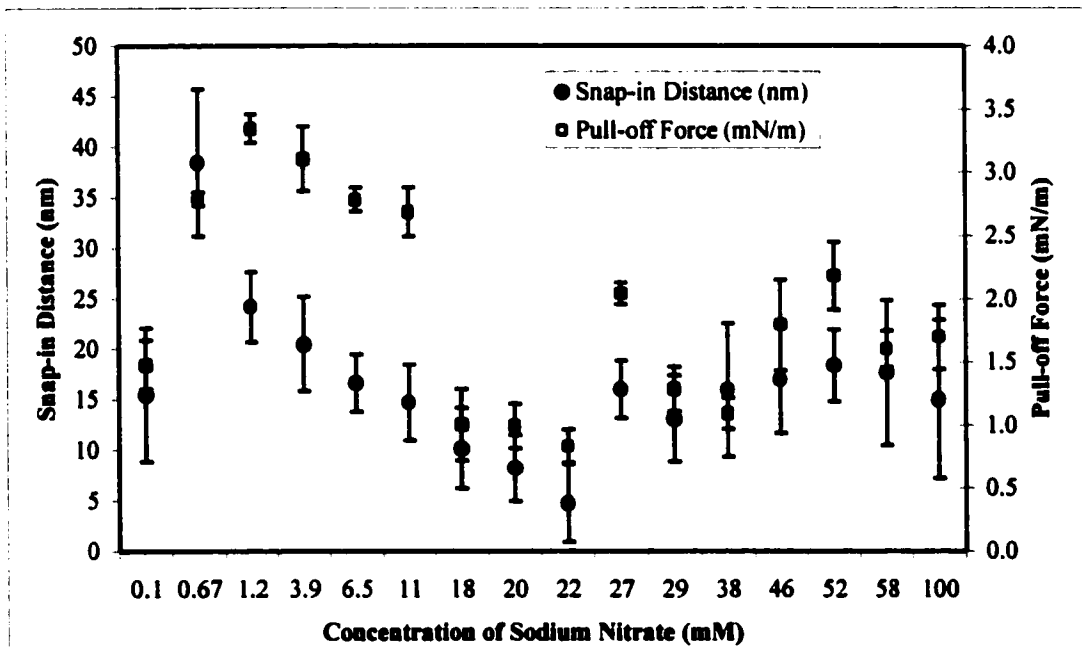


**Figure 4.8:** Electrolyte titration shows snap-in distances and pull-off forces versus  $\text{NaNO}_3$  concentration. Both profiles exhibit coincident minima ( $\sim 22$  mM) as predicted. Attractive snap-in decreases up to 22 mM, then jumps to a constant value for 27-100 mM. Pull-offs are more random.

hydrophobic silica with water contact angles  $\theta > 90^\circ$ . Yoon *et al.* reported 4.63 mN/m for adhesion between hydrophobic silica sphere and plate ( $\theta = 81^\circ$ )<sup>44</sup> which is not drastically different from current results. Surface roughness—best understood as an increase in the effective curvature and a decrease in contact area—will reduce the measured adhesion from the expected ideal value. The JKR theory is only used here as a relative measure of adhesion since the mechanical properties of the film and substrate are not known to fit the elastic assumptions inherent therein.

The simplest explanation for the non-monotonic behavior of dynamic cantilever snap-in as a function of electrolyte concentration (Fig. 4.8) invokes only a single exponential function (Eq. 4.2) for the hydrophobic contribution with  $C_1 = -2$  mN/m and  $\lambda = 4$  nm for  $\psi_{1o} = -60$  mV and  $\psi_{2o} = -35$  mV. The small database represented in Table 4.1 is not really sufficient to determine interaction parameters; however, the findings suggest a slightly weaker hydrophobic attraction separate from a non-double-layer dependence on the presence of ions in solution. Rather than assigning odd electrolyte dependence to the hydrophobic effect, a thorough electrostatic analysis of two moderately hydrophobic surfaces with unequal potentials of same sign provides at least a qualitatively accurate description.

Close examination of the titration curve at lower salt concentrations suggests that a charge, or dipole, correlation is responsible for the longer than expected range of attraction. The hydrophobic parameters were determined from force curves obtained at high salinity (>20 mM) where double-layer and correlation forces are weaker and of shorter range than the hydrophobic effect, which appears to be independent of electrolyte concentration up to 100 mM. This is not contradictory to the work of Kokkoli and Zukowski since the chemical potential effects would remain insignificant for these solutions.<sup>50</sup> Quantitative measurements of electrostatic interactions become dubious when the Debye length is less than the surface roughness and certainly negligible compared to the van der Waals force when under 1 nm.

Lastly, the correlation force (Eq. 4.3) normalized by the radius of curvature was included in generic form with a length scale for surface domains,  $L$ , and a constant scalar,  $C_2$ , being the typical unknowns in an exponential function of separation,  $D$ , and effective inverse decay length,  $\kappa_{eff}$ , raised to a variable power,  $n$ , when included in the pre-exponential intensity:

$$\frac{F}{R_s} \approx C_2 \kappa_{eff}^n \exp(-2D\kappa_{eff}), \quad (4.3)$$

$$\kappa_{eff} \approx \sqrt{\kappa^2 + \left(\frac{\pi}{L}\right)^2}. \quad (4.4)$$

With surface potentials fixed at  $-60$  mV and  $-35$  mV, a single set of parameters is sought that produce theoretical snap-ins with the same trend as the titration experiment (Fig. 4.8). The data between  $0.67$  and  $10$  mM clearly scale exponentially with half the Debye length as predicted by electrostatic correlation theories in general, though the snap-in trend in this regime is not exactly described by simplified theories using values of  $n = 0, 1$ , or  $2$ .<sup>33-37</sup> The remarkable fact is that the snap-in at  $10^{-4}$  M  $\text{NaNO}_3$  is predicted by the hydrophobic term alone, suggesting that the correlation forces are too weak to contribute.

Since the behavior of the correlation effect is not yet well known in a rigorous fashion, it is difficult to determine what dependence the magnitude of the interaction has on ion concentration. Another simple parametric study using  $n = 1$  gives a qualitative fit with  $L = 100$  nm and  $C_2 = -50$  pN as used in Eqs. 4.3 and 4.4. The magnitude of  $C_2$  greatly affects the

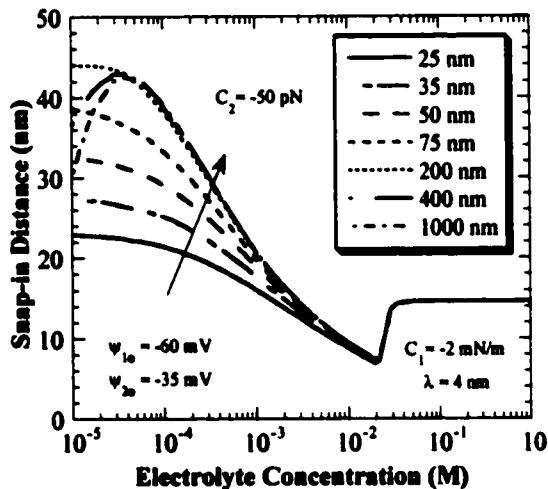


**Figure 4.9:** Parametric study for correlation domain size,  $L$ , with fixed pre-exponential factor  $C_2 = -50$  pN predicting snap-in distance, as previously:  $k_c = 0.056$  N/m.

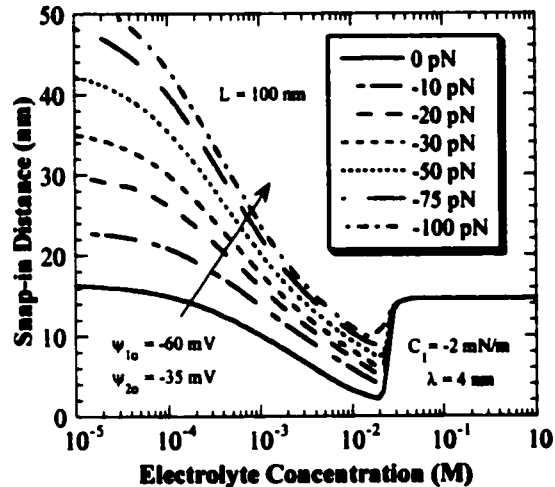


**Figure 4.10:** Parametric study on charge correlation strength  $C_2$  with fixed  $L$  predicting the snap-in distance, complimentary to Fig. 4.9.

minimum snap-in distance and location with respect to ion concentration (Figs. 4.9 and 4.10). Larger values of  $L$  seem equally plausible as they lead to the asymptotic relation  $\kappa_{eff} \approx \kappa$ , where the correlation decay length is basically constant with  $L > 100$  nm for concentrations between

$10^{-4}$  M and  $10^{-1}$  M. Other computations with  $n = 0$  and  $n = 2$  (not shown here) did not accurately reproduce the experimental results either.

Figure 4.11 has a dark, segmented line marking the cantilever stiffness on a force gradient profile calculated as a function of sphere-plate separation, including DLVO, electrostatic correlation, and hydrophobic forces as described above. Following any curve from large to small separations, the surfaces will snap together when the cantilever stiffness,  $k_c$ , equals the force gradient, i.e., when the curve first reaches the spring instability (horizontal line). The snap-in data from Fig. 4.8 has been plotted again with two theoretical profiles from Fig. 4.9 to show the justification for a rather large charge domain correlation length (Fig. 4.12). The calculated snap-in distance decreases with increasing salt to a minimum of 7 nm until the concentration goes above  $2 \times 10^{-2}$  M, qualitatively the same as the experiment. At slightly higher

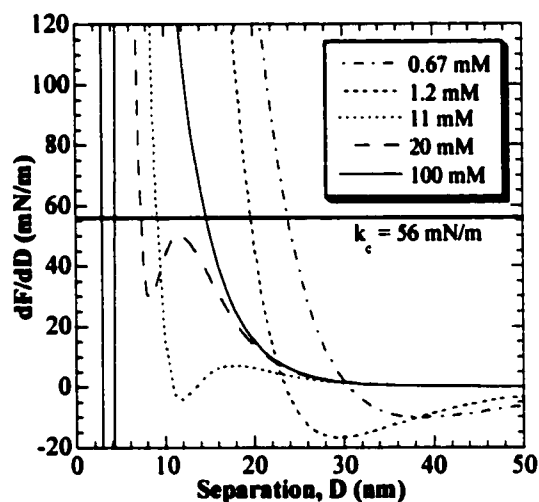


**Figure 4.11:** Total interaction force-field gradients for given monovalent electrolyte concentrations vs. sphere-plate separation. Snap-in occurs for  $dF/dD > k_c$ :  $\psi_{10} = -60$  mV,  $\psi_{20} = -35$  mV,  $C_1 = -2$  mN/m,  $\lambda = 4$  nm,  $C_2 = -50$  pN and  $L = 100$  nm.

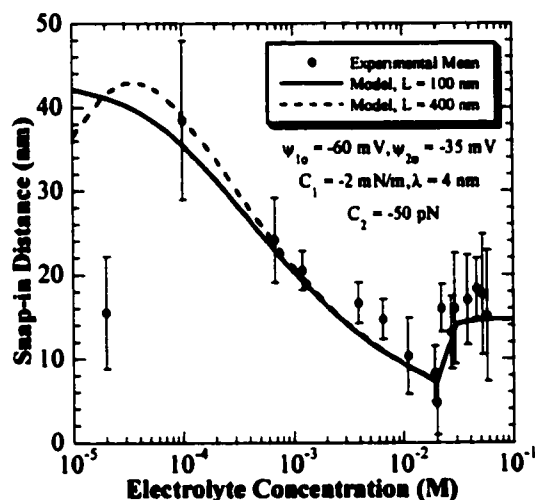


**Figure 4.12:** Snap-in vs. concentration data for  $\text{NaNO}_3$  titration fitted with example curves from Fig. 4.9. Charge domains characterized by a 400 nm length scale provides the better fit.

concentrations, the snap-in quickly grows to the asymptotic value of 15 nm as the hydrophobic effect becomes dominant. However, at lower electrolyte concentrations, the model was unable to fit the magnitude well. The data in Fig. 4.12 have been plotted vs. local concentration prior to complete mixing for a best fit. This suggests that the electrolyte concentration could not reach equilibrium within the sphere-plate gap, after each solution addition, before the next

measurement was taken. It makes little difference above the characteristic minimum snap-in when the interaction is no longer a function of electrolyte.

## 4.5 Discussion

Our colloidal probe experiments showed measurable variability in the local surface energy of the substrates as treated with the silane-coupling agent OTES. The averaged results in Table 4.3 were compiled from several locations to reduce the inherent variability due to topographical roughness and chemical patchiness on the length scale of the probed area, but this also had the undesirable effect of reducing the sensitivity of force profiling. The SFA has a similar effective averaging within a single measurement as it probes larger areas ( $\sim 1 \text{ cm}^2$ ) with reduced absolute force sensitivity. Also, slow mass transfer into the narrow sphere-plate gap can make local electrolyte concentrations lag behind bulk changes, i.e., lower after salt addition or higher when conducting dilutions. However, our data do not reveal any such lagging with time or repeated scans, meaning mass transfer effects should be an insignificant source of error here.

Another source of uncertainty is the very weak cantilever. These probes have been observed to snap in before reaching the theoretical instability, i.e., while the force gradient is less than the spring constant.<sup>56,99</sup> Interaction parameters evaluated with this instability criterion may be overestimates, inferring stronger interactions than an equilibrium measurement would show.<sup>44</sup> The snap-in and pull-off events are both points of instability, and this alone can generate a significant random error for very weak cantilevers caused by finite disturbances from the surroundings. Sufficiently weak cantilevers snap in after reaching the maximum repulsive force,<sup>56</sup> somewhere between a force gradient of  $k_c$  and zero.<sup>65,66</sup> The switch from a negative to a positive force gradient is probably not a smooth transition during real measurements, making this a possible point for induced cantilever instability. In low salt concentrations the difference in separation between zero gradient and  $k_c$  is quite large, and with the current interaction parameters, a snap-in distance as large as 30 nm is supported by this argument for  $6.7 \times 10^{-4} \text{ M}$  (Fig. 4.8). In concentrated electrolyte when the hydrophobic interaction dominates throughout the entire separation range, the computed force gradient is always positive (attractive), gradually increasing with approach until snap-in.

Attractive interactions cannot be tested simply for exponential scaling with Debye length for a proof of electrolyte dependence without successfully deconvoluting the various forces

involved. In general, double-layer interactions depend on the Debye length in a more complex fashion than presented by the commonly used weak overlap approximations,<sup>11</sup> thus our reason for numerically computing the interaction. The decay lengths for the attractive portions of the experimental force profiles could not be compared directly because no equilibrium deflections were accessible with the weak cantilevers in this regime. This eliminated the ability to make any comments about specific changes in force magnitude and range, individually. The findings in the literature<sup>31,33,37,48,49,51-54</sup> of decreasing long-range attraction with greater electrostatic screening do, of course, provide some direction for data interpretation, but most of those systems studied are not very similar to the present work. An electrolyte titration is best suited for investigating attractive forces with decay lengths less than the Debye length of the most dilute electrolyte available. In any case, it is still useful to determine the electrolyte dependence for long-range attractions.

The use of a single surface potential,  $\psi_0$ , to describe a pair of interfaces can lead to erroneous hydrophobic parameters inferred from force vs. separation profiles, especially for the inherently asymmetric surfaces of AFM and even for presumably symmetric systems such as *in situ* surfactant adsorption on to mica in SFA measurements. Small changes in surface potential can also significantly affect the inferred hydrophobic parameters for shorter-range interactions.<sup>66</sup> Two isolated surfaces with constant, unequal and same-sign surface potentials are attracted to each other at small separations in aqueous media because of an imposed charge reversal at the surface of lower potential.<sup>11</sup> The repulsive double-layer force between parallel plates is greatest when the lower potential surface becomes uncharged, in some cases possibly having small charged domains of opposite sign. At some smaller separation the net pressure becomes attractive when the Maxwell stresses overcome the osmotic repulsion of ions in solution.

Other boundary conditions giving first repulsive then attractive double-layer forces with decreasing separation hold the higher potential surface at constant charge density while the lower potential surface is of same sign at constant potential. This situation is not likely since we know both glass and silica surfaces, usually negatively charged, behave closer to constant potential surfaces. Some intermediate behavior like charge regulation is possible, falling between the results of constant potential and constant charge density results; however, the strongest electrostatic attraction occurs when both surfaces hold constant potentials.

Oxide surfaces are expected to be constant potential surfaces, though most studies show some charge-regulation for silica behaving intermediate to the limiting cases of constant potential and constant charge density.<sup>11</sup> We speculate that silanated oxides would not necessarily exhibit the same double-layer behavior as prior to coating since a significant number of the amphoteric hydroxyl groups responsible for surface charging are eliminated, and hydrocarbon becomes the majority species of the presented surface. Then the plane of charge responsible for double-layer interactions consists of a unique environment which may include surface silica, unreacted silanols, partially charged siloxanes, trapped, bound, or dissociated water—all likely components for nearly constant surface potential. Also, Podgornik and Parsegian pointed out that these constant-potential/constant-charge limits may not hold for charge-correlating surfaces and are definitely not valid for their model of cationic surfactant adsorption to mica.<sup>100</sup> Attractive double-layer forces for any reasonable surface potentials could not explain the range of attraction observed at lower electrolyte concentrations, though they may for some systems.

The formalisms for various electrostatic correlations have been derived for simplified cases but do not completely explain the extant body of work on attractions decaying exponentially with half the Debye length,  $\kappa^{-1}$ . Theoretical models for charge correlation effects have been derived for net neutral surfaces assuming a regular lattice of domains, but neutrality of only one surface will also precipitate a similar range of attraction.<sup>36,37</sup> If an electrostatic correlation exists between the constant potential quartz and glass surfaces, it is most attractive when the lower potential surface becomes neutrally charged. The fact that the surface charge density is not constant during an experiment makes it extremely difficult to apply existing correlation theories directly with quantitative significance. To further complicate experimental interpretations, a correlation between randomly patchy surfaces is not expected to quantitatively agree with these ideal lattice-based constructs.

The strength of adhesion, or pull-off force, observed between the OTES-coated surfaces does not follow a clear trend, as with snap-in, though the effect of electrolyte cannot be ruled out by these experiments alone (Fig. 4.12). The work of adhesion appears to remain roughly constant over ranges of concentration followed by larger, discrete changes, in contrast to the more continuous changes in long-range attractions. Pull-off forces did not change in connection with any particular feature of snap-in distances and any hypothesized trend will have obvious outliers. Pull-off magnitudes began at 1.5 mN/m in  $10^{-4}$  M NaNO<sub>3</sub> and jumped to 3.5 mN/m at

$10^{-3}$  M, then remained constant at  $\sim 2.7$  mN/m from  $3.9 \times 10^{-3}$  M to  $1.1 \times 10^{-2}$  M  $\text{NaNO}_3$ ,  $\sim 1$ - $2$  mN/m above  $2.7 \times 10^{-2}$  M, and hit a minimum plateau at  $\sim 1$  mN/m for the same concentration range as the minimum snap-in ( $2 \times 10^{-2}$  M). The wettability of the hydrophobic layers may be affected, either through surface energy or structure, to some small degree by the presence of ions. The lack of strong correlation makes it difficult to say anything conclusively about the effect of electrolyte on adhesion, but it may be increased for low to medium electrolyte concentrations by the same mechanism that increased long-range attraction. This is a reasonable assertion when considering that electrostatic fluctuations are related to the zero-frequency van der Waals force which would directly affect adhesion.<sup>33</sup>

Surface deformation with repeated contacts complicates interpretations because it cannot be directly deconvoluted from other system changes. Several consecutive pull-off forces taken within minutes of each other showed gradually increasing adhesion 60% of the time while only 10% showed decreasing trends. The AFM measurements conducted over several minutes and more inevitably show some variability due to scanner drift even after hours of warm-up, but this more likely suggests a visco-elasto-plastic behavior of the cross-linked siloxane film. Asperity alignment shifts slightly with time, and imperfect elastic deformation of the soft hydrophobic films with repeated contact conforms the surfaces to each other, decreasing roughness. After waiting twenty minutes, the pull-off force often returned to near the initially measured value, suggesting that the hydrophobic layers were fairly soft, with some viscoelastic character that allowed the deformed areas to recover their original condition within minutes. The respective groupings of consecutive approach curves had a matching upward trend in snap-in distance. Taken in concert, these observations suggest that the effective surface area over which the interaction was operating generally increased with repeated contact, increasing the interaction by temporarily reducing surface roughness. Considering that roughness tends to decrease interparticle forces, or at least their apparent range, makes colloidal probing less likely to detect very small ranged interactions accurately or at all with anything other than atomically flat or smooth surfaces.<sup>54</sup> An independent study of surface deformation with repeated contact at constant loading would be extremely helpful for conclusive interpretations.

## 4.6 Conclusions

A parametric study of snap-in distance as a function of electrolyte concentration considering DLVO and hydrophobic interactions between silanated glass and quartz has illustrated the competition of forces that can produce a characteristic, non-monotonic trend in long-range attraction. We have outlined and conducted a relatively simple and efficient procedure for determining the hydrophobic interaction parameters of an asymmetric system tested in the sphere-plate geometry for AFM, and similar, experiments. This is the first thorough electrolyte investigation that we are aware of with stable, chemically modified surfaces suggesting that electrolyte does not play a role in the hydrophobic interaction, which is believed to be distinctly independent of any long-range electrostatic correlations.

The strength and range of the hydrophobic effect may be readily quantified from an experimental snap-in vs. concentration curve, providing the substrates are adequately charged, but interaction parameters cannot be unambiguously determined from snap-in distances at only a few concentrations. It is understandable that inconclusive or even false deductions about the hydrophobic strength and range can be drawn from an insufficient database of surface force experiments requiring deconvolution of several effects. The interesting and reproducible observation of a minimum snap-in distance for some intermediate salinity is qualitatively modeled with only a single exponential function for the hydrophobic effect. Independent knowledge of the potential or charge density of at least one surface was required, and additionally, an attractive electrostatic correlation provided a more quantitative explanation of the trend at low to intermediate concentrations.

## CHAPTER 5:

### QUANTITATIVE AFM FOR FLUID INTERFACES

#### 5.1 Summary

Net repulsive interactions between n-hexadecane and a polystyrene microsphere in aqueous solutions are measured with atomic force microscopy (AFM) and interpreted using the augmented Young-Laplace equation. The true separation between probe and fluid interface is implicitly computed from the force-distance data, providing a more accurate description of drop or bubble deformation. Experiments and theoretical arguments demonstrate that a fluid interface stiffens with increasing deformation and is not accurately treated as a Hookean spring. The unexpected stability of the draining aqueous film between hydrophobic bodies in electrolyte solutions is explained primarily by the deformation of the oil drop in response to the applied normal force, as well as the increased hydrodynamic resistance due to the increased drainage area.

#### 5.2 Background

The now routine colloidal probe technique of AFM has come to explore interfacial phenomena between rigid microspheres and deforming drops or air bubbles, but provides limited quantitative results that are comparable to theoretical models (see Sections 2.1 and 2.3). The main difficulty lies in the approximations of the interfacial deformation with applied force, since the true sphere-drop separation is typically unknown and cannot be measured. The present work seeks to establish the efficacy of solving the augmented Young-Laplace equation with known interaction parameters for drop deformation as a function of applied force in order to examine fluid interface (FI)-AFM force-distance data properly on a basis of actual surface-probe separation. Until now, a linear interfacial deformation with applied force has always been assumed without independent evidence<sup>2</sup> when interpreting the behavior of air bubbles and oil drops. This assumption of linear drop deflection is scrutinized through a more exact theoretical analysis, and the effect of changing various experimental conditions is evaluated in consideration

of the apparent oil drop stiffness. The most straightforward procedure is an electrolyte titration<sup>14</sup> that may be more generically employed as a force titration in which any single parameter may be systematically changed to facilitate deconvolution of the independent forces in combined action at the fluid-fluid interface. The addition of salt or increase of approach velocity happen to be the easiest to accomplish; but it is also feasible, though more time consuming, to vary probe radius, drop radius, surface potential or charge density.

The current objective is to determine the exact relationship between applied force and deformation of a fluid-fluid interface for the AFM geometry of a rigid sphere impinging at a drop or bubble apex. The magnitude and range of interactions between a polystyrene microsphere and n-hexadecane drop are measured in aqueous environments, and experimental force-distance profiles are modeled using the augmented Young-Laplace equation. A careful deconvolution of the true sphere-drop separation from the scanner displacement is possible for repulsive interactions, allowing FI-AFM to be a truly quantitative technique for surface force investigations. This work utilizes the electrolyte titration to investigate the relative importance and complexity of film drainage and dynamic interfacial tension.

### 5.3 Experimental Methods

FI-AFM force profiles were gathered using a Park Scientific Instruments AutoProbe<sup>®</sup> CP with the pendent-drop liquid cell and a clear, homemade sample holder with fluid reservoir. A polystyrene-divinylbenzene sphere (Duke Scientific Corp., Palo Alto, CA, mean diameter 19.7  $\mu\text{m}$ ) was glued to replace the pyramidal tip of a gold-coated triangular cantilever (Microlever<sup>™</sup> A, Park Scientific Instruments, Sunnyvale, CA) of nominal spring constant 0.05 N/m—a standard procedure.<sup>17</sup> Stiffness calibrations<sup>97</sup> gave values of 0.048 to 0.056 N/m. The surface roughness of the sphere is quite high:  $\sim 10\text{-}30$  nm rms by contact AFM over a 1- $\mu\text{m}$  cap.

Force-distance,  $F(z)$ , measurements were performed at the apex of the oil (n-hexadecane) drop to satisfy the axisymmetry condition imposed on the Young-Laplace equation (Eq. 5.1). The probe was carefully aligned horizontally and vertically with a monocular microscope to within 10  $\mu\text{m}$  of center; the relatively large drop radius of curvature ( $R_d \sim 250$   $\mu\text{m}$ ) does not allow better accuracy. The salt concentration was adjusted by volumetric additions of  $\text{NaNO}_3$  solutions, beginning with an initial charge 0.1 mM prepared with deionized and twice-

distilled (3D) water increasing to 100 mM. Sodium dodecyl sulfate (SDS),  $\text{NaNO}_3$ , and n-hexadecane were all purchased from Sigma Chemical Co. (St. Louis, MO).

The previous work of Miklavcic *et al.* is naturally extended to AFM experiments, as suggested.<sup>70</sup> The augmented Young-Laplace equation (Eq. 5.1) describes a pressure balance at the oil/water interface, where the curvature (bracketed term) at any point,  $\kappa(r,z)$ , is determined by the sum of gravity,  $g\Delta\rho z$ , internal drop pressure,  $P_o$ , and disjoining pressure,  $\Pi$ :  $\sigma = 52$  mN/m,  $g = -9.81$  m/s,  $\Delta\rho = 0.224$ ,  $P_o = 2\sigma/R_d$ ,

$$\sigma \left( \frac{z''(r)}{(1+z'(r)^2)^{3/2}} + \frac{z'(r)}{r\sqrt{1+z'(r)^2}} \right) = g\Delta\rho z(r) - [P_o - \Pi(D(r))]. \quad (5.1)$$

The Laplace pressure (Eq. 5.1, left term) is simplified for axisymmetry of the drop deformed by a sphere with an inverted cylindrical coordinate system of origin at the initial drop apex (Fig. 5.1). The function  $D(r)$  expresses the separation profile for the sphere-drop system, i.e., the aqueous film thickness, whose minimum value is the point of closest separation,  $D_o$ . The first

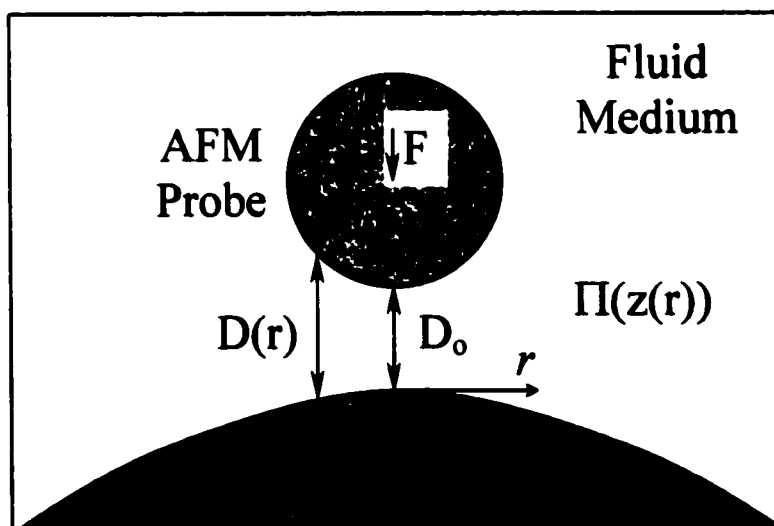


**Figure 5.1:** FI-AFM schematic: sphere-drop (or bubble) geometry for the Young-Laplace equation. The unique gap profile  $D(r)$  describes the separation between the fluid interface and probe at any radial distances from the cylindrical axis of symmetry.

and second derivatives of drop height with radius are written as  $z'(r)$  and  $z''(r)$ , and the drop profile  $(r,z)$  is computed numerically with a variable step-size 4<sup>th</sup> order Runge-Kutta routine (Appendix C). When the slope of the drop profile is large, the Young-Laplace equation is

parameterized by  $dz/dr = \tan\phi^2$  where  $z$  and  $r$  are both functions of the azimuthal angle  $\phi$  measured from the negative  $z$ -axis.

Boundary conditions on the drop include constant volume and symmetry at the apex ( $dz/dr = 0$ ). The effect of gravity on the drop profile for the present conditions is insignificant, but it has been included for generality. The internal drop pressure is effectively constant. The disjoining pressure includes terms for DLVO and hydrophobic interactions as well as hydrodynamic drainage. Only the two hydrophobic interaction parameters are treated as fitted values; all other system parameters are known.

## 5.4 Results and Discussion

Solutions to Eq. 5.1 for the n-hexadecane drop profile evolution in water during an FI-AFM experiment were first computed using only DLVO theory for the surface forces. The Derjaguin approximation relating the force between two spheres of radii  $R_1$  and  $R_2$  to the interaction energy per area of parallel plates,  $W$ , is valid for all oil-drop/microsphere configurations since the separation,  $D$ , is always much less than the radius of curvature of either the oil/water interface or the polystyrene bead:<sup>26</sup>

$$F = 2\pi \left( \frac{R_1 R_2}{R_1 + R_2} \right) W. \quad (5.2)$$

To get the disjoining pressure needed for Eq. 5.1, common expressions for  $W$  or  $F$  were differentiated,<sup>101</sup> where  $R_e$  is the equivalent radius of a sphere interacting with a plate (Eq. 5.3):

$$\Pi = -\frac{dW}{dD} = -\frac{1}{2\pi R_e} \frac{dF}{dD}. \quad (5.3)$$

The non-retarded van der Waals pressure (Eq. 5.4) is derived from Eq. 4.1 including the hard wall term:

$$\Pi_{vdW} = -\frac{A}{6\pi} \left( \frac{1}{D^3} - \frac{4r_o^6}{D^9} \right). \quad (5.4)$$

The Hamaker constant,  $A$ , for hydrocarbon-water-hydrocarbon interfaces is of the order of  $10^{-20}$  J, the exact value depending on the mixing rule used.<sup>26</sup> The contact repulsion is practically

unnecessary and could be dropped for fluid interfaces, since physical contact is a wetting condition.

The pressure expression for electrostatic double-layer interactions (Eq. 5.5) is derived from the Debye-Hückel approximation by Wiese and Healy, which is appropriate for the oil drop/polystyrene sphere in water having constant surface charge densities and dissimilar, isolated surface potentials:<sup>102</sup>

$$\Pi_{el} = \frac{2\epsilon\epsilon_0\kappa^2 \left[ \psi_{10}\psi_{20}(e^{-\kappa D} + e^{-3\kappa D}) + (\psi_{10}^2 + \psi_{20}^2)e^{-2\kappa D} \right]}{(1 - e^{-2\kappa D})^2} \quad (5.5)$$

This relationship was found to be in excellent agreement with numerical solutions to the non-linear Poisson-Boltzmann equation<sup>82</sup> even up to 50 mV surface potentials,  $\psi_{10}$  and  $\psi_{20}$ . For experimental analysis, the isolated surface potentials are replaced by zeta-potentials for both n-hexadecane drops and polystyrene beads calculated with the Helmholtz-Smoluchowski equation from electrophoretic mobilities measured with a Rank Brothers Mark II and a Malvern Zetasizer 3000HS, respectively, in carbon dioxide-equilibrated water (pH  $\approx$  5.5-6). The oil drops dispersed in water by sonication were typically of the order of a micron in diameter and assumed rigid. The oil drop zeta-potentials averaged  $-16$  mV in 10 mM NaCl at 22°C, while the mean value for polystyrene was  $-20$  mV in pure water at 25°C. Since these zeta-potentials are quite similar, Eq. 5.5 may be further reduced with the approximation  $\psi_{10} = \psi_{20} = \psi_0$ . But it is useful to introduce the more generalized form for fitting experimental data when the electrostatic boundary conditions are known.

The sum of Eqs. 5.4 and 5.5 is used for  $\Pi(D(r))$  in Eq. 5.1. The vertical deformation of the oil drop (a hemisphere resting on a flat plate) is only linear with force applied at the apex for extremely weak interactions or for appropriately small changes in force. Figure 5.2 is a theoretical calculation of force normalized by the sphere radius,  $F/R_s$ , as a function of

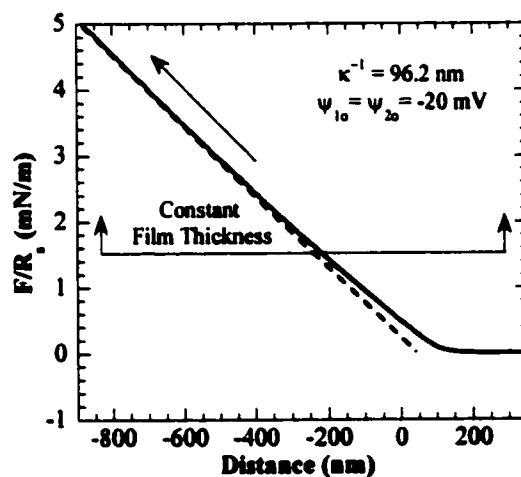


Figure 5.2: Computed force-distance profile expected from FI-AFM with a polystyrene sphere and n-hexadecane droplet in water. Actual separation is constant above 1.4 mN/m. The dashed line is to aid the eye.

sample or scanner displacement,  $z$ . This  $F(z)$  profile depicts typical experimental data as acquired with FI-AFM. The drop deflection is convoluted with the actual sphere-drop separation by simple additivity. The result is a nonlinear constant compliance region for the deforming oil/water interface. Above some critical force (about 1.4 mN/m for conditions of Fig. 5.2) the true sphere-drop separation at the apex remains constant. This regime stretches the fluid interface under stable film draining conditions. The interface continues to wrap itself around the sphere, increasing the interfacial area within the constant film thickness zone. Theoretically, the drop will dimple inward indefinitely if it is able to reach this constant and limiting film thickness; but practical limitations on film stability will eventually disrupt equilibrium: finite disturbances from the environment or microsphere surface roughness, for example.

Even for moderately low surface potentials or charge densities, the interfacial tension is not great enough to force the intervening aqueous film to drain to the point where the van der Waals attraction can dominate the interaction. If the double-layers are collapsed with high salt or if the surfaces are oppositely charged, as is fairly uncommon, then the probe will eventually contact the oil, even snapping in dynamically to attain a three-phase contact line. Similarly, if another long-range attraction like the hydrophobic force were at work, the oil drop would be pulled upward, quickly becoming mechanically unstable and jumping into contact. In light of the fact that the hexadecane/water interfacial tension is large and the zeta-potential is small, it would seem likely that most other systems of interest would have a significant repulsive regime to study with FI-AFM.

By summing the vertical components of pressure distributed over the oil/water interface, the net force as it would be measured by the AFM probe is computed for plotting as a function of actual sphere-drop separation (Fig. 5.3, solid line). Then, if the interface were to behave as a Hookean spring, it should be possible to convert the force vs. total distance displaced (Fig. 5.2) into the true force-separation profile simply by adding the quantity

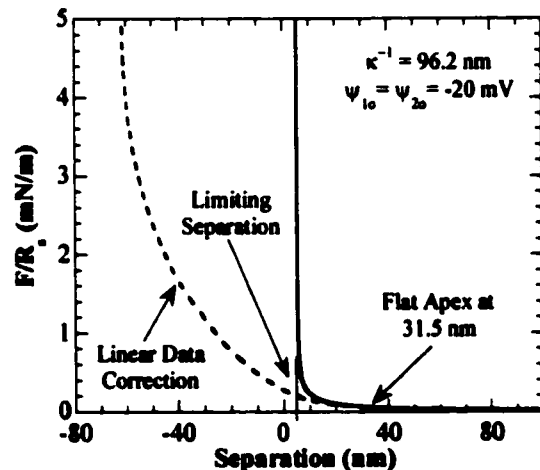
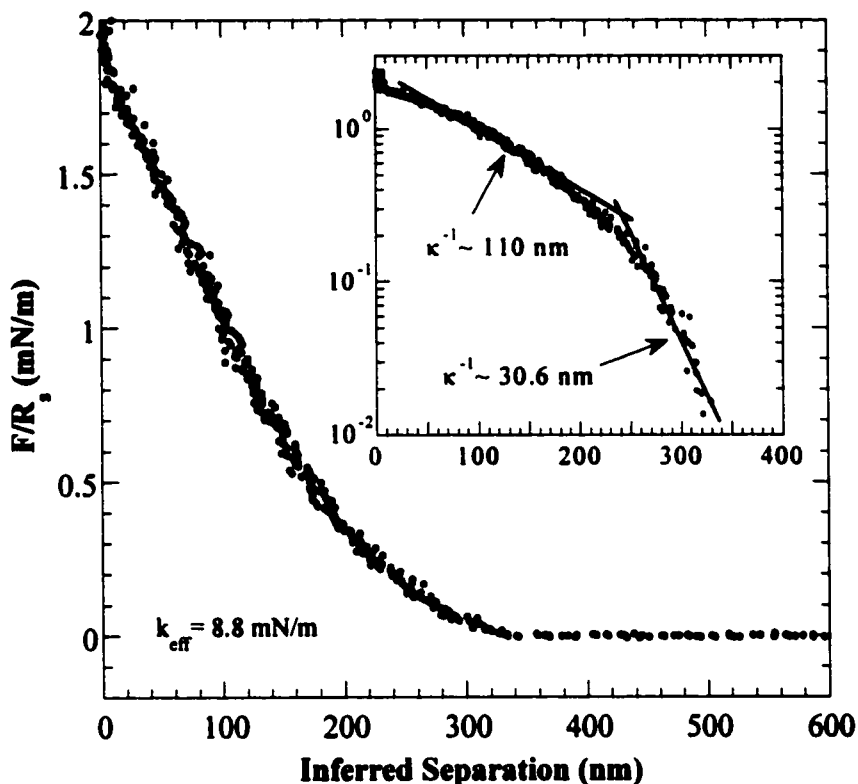


Figure 5.3: Theoretical DLVO force profile for hexadecane-polystyrene interaction in water for true separation (solid line) and separation inferred from AFM data based on Hookean model (dashed line)



**Figure 5.4:** Experimental data for a polystyrene sphere pushing against an n-hexadecane droplet in 0.1 mM NaNO<sub>3</sub>, corrected for a linearly deflecting interface. Inset emphasizes disparity in attempted exponential fitting.

of force divided by the effective interfacial spring stiffness,  $k_{\text{eff}}^{-2}$  Separation = Distance +  $F/k_{\text{eff}}$ . The quantity  $F/k_{\text{eff}}$  is the interfacial displacement normally inferred from AFM experiments on air bubbles or oil droplets. The value of  $k_{\text{eff}}$  is the slope of  $F(z)$  at high load, considered to be similar to hard wall contact with a solid surface. But it is obvious from Fig. 5.2, as well as from experimental data (Fig. 5.4), that  $k_{\text{eff}}$  is different depending on where it is measured; greater deformation yields a larger linear spring constant.

An experimental force-separation profile for the hexadecane-polystyrene interaction in 0.1 mM NaNO<sub>3</sub>, was constructed using the procedure of Ducker *et al.*, assuming a linearly deflecting interface (Fig. 5.4). The attempt to convert the force-displacement data of the experiment into a force-separation profile was unsuccessful. It is obvious that the resulting curve cannot be fit by a single repulsive and exponentially decaying function (Fig. 5.4, inset). Only in the limit of vanishingly small forces (very large separations) are the data fit by a reasonable Debye length, viz., one expected for 0.1 mM monovalent electrolyte ( $\kappa^{-1} = 30.4$  nm).

The compliance portion of the data is also completely unaffected by any change in external approach velocity, and the slope continuously increases with deformation, deviating further and further from linearity. Thus, both experiment and theory clearly point to a nonlinearly deflecting fluid-fluid interface.

The numerical algorithm for calculating the oil drop deformation with force, i.e., given values of  $R_0$ ,  $R_d$ ,  $A$ ,  $\kappa^{-1}$ ,  $\psi_{10}$ , and  $\psi_{20}$ , does not allow a direct fitting procedure for experimental data. Instead, the model results are plotted and compared in the  $F(z)$  format, as in Fig. 5.2. The surface charge densities involved are not large enough to expect much variance with electrostatic screening, even with a rather weak cantilever. The sensitivity of the AFM relative to the surface forces being measured is of the order of 0.01 mN/m, but is more greatly limited on the displacement scale by the interfacial mobility. Variations between similar experiments are common and easily explained as the result of varied oil drop size and probe position relative to the center of the drop.

It has been suggested that  $k_{eff}$  may be related to the interfacial tension;<sup>6</sup> however, it is suspected that this would only be the case within some limiting regime, like that of small interfacial deflections. This linear correction clearly leads to misinterpretation of the data for interactions larger than 0.1 mN/m (Fig. 5.4). Furthermore, this provides another possible explanation for the apparent transition observed by Hartley *et al.* from the exponential force behavior of overlapping double-layers, when the drop acts like a ideal spring, to the “simple linear relationship” of force with apparent separation, not to be confused with the linearity of the interfacial deflection with load. To maintain the analogy, if the oil/water interface is like a spring but with an increasing stiffness, then  $k_{eff}$  may be expressed as a weak function of drop deflection. It might be useful to fit experimental data with a power function to convert  $F(z)$  curves into  $F/R$  vs. separation, viz.,  $F = kd^n$ , where  $d$  is the drop deflection,  $k$  is constant, and  $n$  is slightly increasing as  $d$  increases ( $n$ -values taken from fitting the model results). If the stiffness is, indeed, equivalent to the interfacial tension, then the  $d^n$  term is merely the  $z$ -component of a surface integral of the interfacial curvature (Eq. 5.1), which has no analytical solution, in general. It remains to be shown what physical conditions, if any, lead to this complex behavior. Empirically, there seems to be a connection between the onset of the drop dimpling inward and the deviation from linear interfacial deflection (Fig. 5.3): apex curvature inversion from convex to concave (Fig. 5.5). It may be simply a geometric consequence of measuring only the normal force component of a curved film with increasing interfacial area.

Unlike the scenario where a drop or bubble pushes against a flat plate,<sup>70</sup> the initial curvature of the interface has a relatively small effect on the sphere-drop interaction. The internal drop pressure is minute compared to the disjoining pressures associated with significant deformation. The microsphere radius,  $R_s$ , is a much more significant parameter, since it determines the final interfacial curvature for repulsive interactions. A fluid-fluid interface deforms less for smaller probes having two consequences on AFM: the cantilever bends more for a given interfacial deflection, and the minimum film thickness

decreases. The drop profile is also much more sensitive to  $R_s$  than to the Debye length,  $\kappa^{-1}$ , or the surface potentials,  $\psi_{10}$  and  $\psi_{20}$ . This fact makes it difficult to use FI-AFM for independent determination of  $\psi_{10}$  and  $\psi_{20}$ .

In order to reproduce a real experiment successfully with the augmented Young-Laplace equation, hydrodynamics must be considered. This repulsive lubrication will help to further stabilize the sphere and oil against coalescence and to maintain film thickness. A simple pseudo-steady state equation for hydrodynamic film drainage between a sphere and a plate may be derived as the Reynolds equation in pressure form (Eq. 5.6) from the Navier-Stokes equation:<sup>74</sup>

$$\Pi_H = \frac{3\eta R_{eff}}{D^2} \frac{dD}{dt}. \quad (5.6)$$

This relation has been further generalized for boundary conditions that deviate from the no-slip condition<sup>79</sup> or if film drainage rates are large enough to see inertial effects.<sup>75,103</sup> But the Reynolds equation appears to be sufficient as a first approximation for most FI-AFM approach velocities accessible. Film drainage is more important here than for approaching solid bodies because of the film area increasing with deformation. The velocity,  $v = dD/dt$ , is estimated as a function of radius from a simple mass balance. That is, the film drainage rate is recalculated for

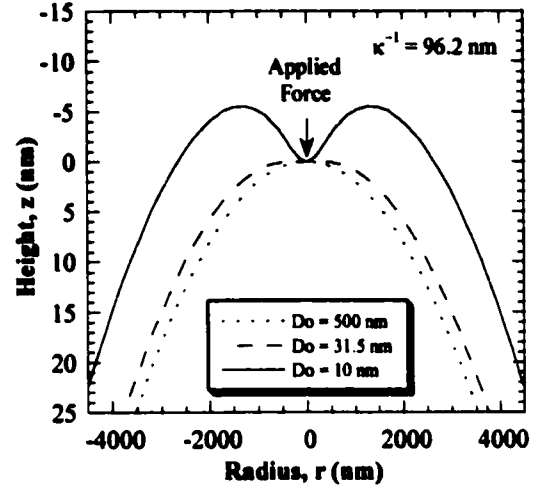


**Figure 5.5:** Drop apex profiles calculated for axisymmetric deformation by a sphere:  $R_d = 250 \mu\text{m}$ , constant curvature ( $D_o > 500 \text{ nm}$ ), zero apex curvature ( $31.5 \text{ nm}$ ), apex curvature inversion ( $< 31.5 \text{ nm}$ ) and wrapping film (e.g.,  $10 \text{ nm}$ ), limiting separation not shown ( $5.4 \text{ nm}$ ).

all separations as the difference between the initial external approach speed and the rate of interfacial deformation. The effective radius of curvature,  $R_{\text{eff}}$ , changes with deformation, as well.

Lastly, since both oil drop and polystyrene sphere are hydrophobic, a long-range attraction is expected of an exponential form with separation, whatever the mechanism.<sup>12,39,44,104</sup> This hydrophobic force empirically described by pre-factor,  $C_1$ , and decay length,  $\lambda$ , is assumed to be independent of electrolyte concentration (Eq. 5.7):

$$\Pi_h = \frac{C_1}{2\pi\lambda} \exp\left(\frac{-D}{\lambda}\right). \quad (5.7)$$

A more classic hydrophobic interaction<sup>55</sup> may be too short-ranged to be observable with FI-AFM, in which case maximum possible values for the hydrophobic parameters can be estimated from the theoretical model (see Section 2.2 and Chapter 4 for more).

The first experimental data for hexadecane and polystyrene were gathered in 0.1, 1, 10, and 100 mM  $\text{NaNO}_3$  solutions ( $\kappa^{-1} = 30.4, 9.6, 3.4$  and  $0.96$  nm, respectively) for several external approach velocities (Fig. 5.6). The data for 0.1 mM  $\text{NaNO}_3$  show a slightly longer-range

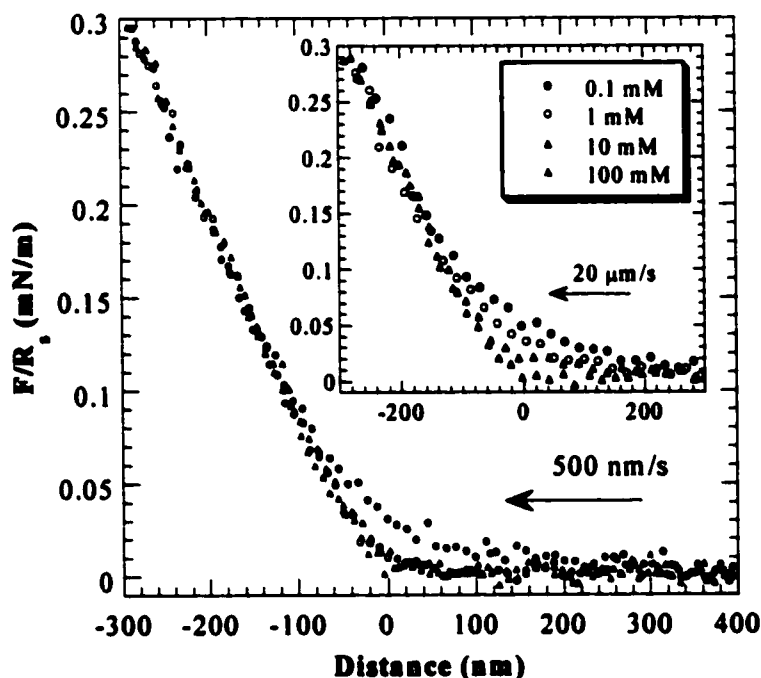


**Figure 5.6:** FI-AFM profiles for hexadecane-polystyrene interaction in aqueous  $\text{NaNO}_3$  solutions compared on a distance scale of scanner displacement at two external approach speeds.

repulsion, but the other profiles are indistinguishable from one another. Changing approach speeds in the range of 0.12-1  $\mu\text{m/s}$  did not affect the interaction profiles, but data acquired above 2  $\mu\text{m/s}$  gradually differentiated itself with respect to electrolyte concentration for higher velocities up to 20  $\mu\text{m/s}$ , as seen in the inset of Fig. 5.6. Even so, the ambient noise level within the system is very near the force sensitivity. The trend with decreasing Debye length is opposite from what might be expected from the theory as previously outlined. The calculated force-profiles predict a decreasing dependence on electrolyte with higher approach speeds (Fig. 5.7); that is, the hydrodynamic repulsion will dominate the electrostatic double-layer force for fast approaches. At 0.5  $\mu\text{m/s}$  external approach velocity, the net interaction is decreased by increasing salt concentration, while the drainage repulsion becomes dominant above 1  $\mu\text{m/s}$ . Even at 2  $\mu\text{m/s}$  (Fig. 5.7 inset), the calculated profiles for 1, 10, & 100 mM are nearly identical, similar to experiment (Fig. 5.6). Considering that there is no absolute reference for the distance scale with FI-AFM, there is no way to observe experimentally the slight variations at small separation.

Changing the approach speed is a very indirect and highly inefficient way of manipulating the hydrodynamics in FI-AFM. The reason for this is quite clear: the faster the

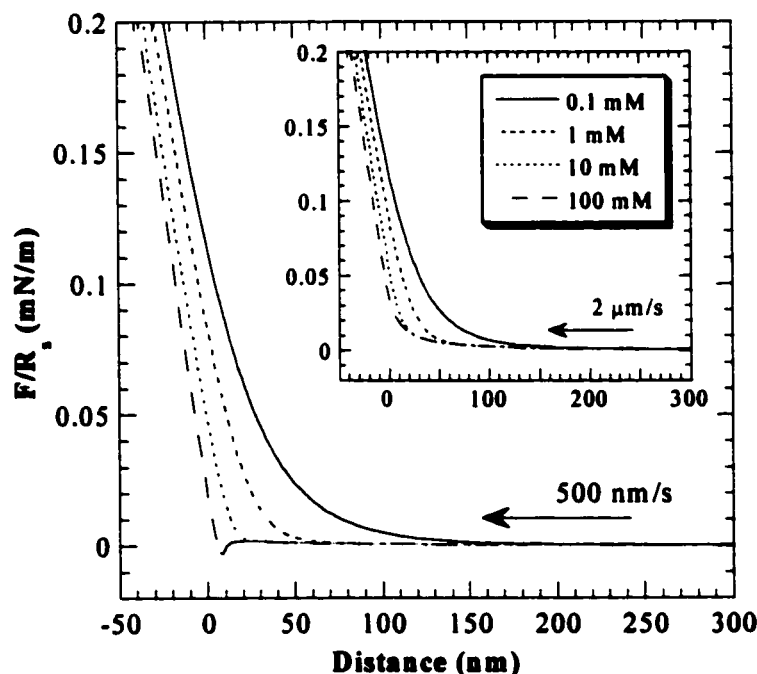


**Figure 5.7:** Theoretical  $F(z)$  curves for electrolyte titrations at 0.5 and 2  $\mu\text{m/s}$  (inset) for comparison with Fig. 5.6:  $\psi_{1o} = -16$  mV,  $\psi_{2o} = -20$  mV,  $R_d = 250$   $\mu\text{m}$ ,  $R_s = 8.5$   $\mu\text{m}$ .

approach, the faster the deflection of the interface and, thus, the true film drainage rate which is responsible for the hydrodynamic repulsion remains nearly constant over a range of external approach velocities spanning more than an order of magnitude. The increased probing rate can only have a measurable effect at long ranges before significant interfacial deformation reduces the actual approach velocity of the two interfaces. The most likely explanation for the quantitative disagreement between experiment and theory is that the hydrodynamics of the draining thin film are more repulsive than expected from Reynolds lubrication because of the changing geometry and deviations from the ideal boundary conditions, specifically, assuming smooth interfaces. Because of this, not only are the electrostatic interactions of lesser importance, but no long-range attractions are ever observed. Model computations suggest that a hydrophobic force of  $\lambda = 3$  nm and  $C_1 = -2$  mN/m, or smaller, could essentially remain hidden during these experiments, since the film thickness remains too large under all explored conditions for the hydrophobic interaction to be felt. However, this is by no means a unique fit, and the underestimate of hydrodynamics must be addressed before anything certain may be concluded. The van der Waals attractions also go undetected for similar reasons.

The most simplistic corrections to the Reynolds equation have already been made: variable film drainage rate,  $dD/dt$ , and radius of curvature for the system,  $R_{eff}$ . An *ad hoc* solution of fitting an effective probe radius would be one way to approach the problem empirically. This also complicates the issue by adding another parameter to fit along with the hydrophobic force parameters. Simply scaling the current hydrodynamic relation still shows an electrostatic decay that is not convincingly evident in the experiments and does not address the specific issue raised of why there appears to be two hydrodynamic regimes: one for thin “Reynolds” films and one for thin-thin films. It might also be tempting to suggest that the electrostatic interaction was simply too weak to be observed independently. However, if that were the case, then the polystyrene sphere would be engulfed once the true approach velocity went to zero, either at the limiting film thickness or the turn-around point of the AFM scan. Reality is to the contrary, since a majority of the profiles are monotonically repulsive and show no wetting on withdrawal (zero pull-off).

Clearly, the hydrodynamic effect is very important for film stability and more complex than our current analysis explains. The current approximation is reasonable for thicker films, or larger separations, in the FI-AFM configuration because the geometry is not far from that of the rigid sphere-plate case and is still adequately described by  $R_{eff}$ . But when the film begins

wrapping about the spherical probe, the situation comes closer to parallel plates of finite area. This regime dominates at very small separations, perhaps 10-20 nm for this probe diameter and other system parameters, very near the limiting separation due to the deforming interface. That is, the hydrodynamics in the wrapping thin film are likely more repulsive, in terms of a net force, than the electrostatics at all salt concentrations observed. This can be easily visualized in a qualitative sense but will require a greater depth of fluid dynamics to describe quantitatively.

In the present experiments, the thin hydrodynamic film regime is observed when the fluid interface is moving nearly in register with the impinging sphere, i.e., the drainage rate approaches zero at the apex. The velocity profile increases in the radial direction, so the first assumption is that the hydrodynamic repulsion must increase radially for some distance before it drops off into the bulk pressure of the medium. Then, there is some circumscribing region about the axis of symmetry, perhaps the hydrodynamic “edge” of the film, where the pressure would be maximum. But, ignoring surface forces, the hydrodynamic pressure must be constant, from Eq. 5.1, throughout that portion of the draining film having constant curvature at the oil/water interface, i.e., the wrapping film. Therefore, it is this film “edge” pressure which determines the interior film pressure even when the drainage rate inside the film is zero, or nearly so.

Of course, the surface forces are also constant within a constant thickness film, so their inclusion really does not complicate the issue any further. In this scenario, since the surface forces must either stay constant or decrease with increasing radius, it is the hydrodynamics at this “edge” which will determine the film dimensions and evolution after the final interfacial curvature at the geometrically-limited minimum separation is achieved. The film area continues to grow with further interfacial deformation. Therefore, it is probably neither the externally driven approach velocity nor the drainage rate at the apex of the probe which most greatly affects the net interaction in this constantly complying regime, but a very much more complex situation. The scope of the present work does not quantitatively address this issue, but the combined experiments and theoretical arguments definitely show that something like this hypothetical explanation is at play.

There are some further issues to consider for good theoretical comparison to experiment. Careful alignment of the probe at the drop apex is critical to the axisymmetric constraint. Since the AFM detects only a net force in the vertical direction, the magnitude of the measured force decreases for locations off-axis from the drop apex. In this configuration, the net action of the Laplace pressure is no longer co-linear with the cantilever deflection. Non-axisymmetric

pressures will serve to displace the drop horizontally due to unbalanced forces which also go undetected and lead to smaller inferred interactions than those computed. The deformed drop profiles calculated are not the lowest energy conditions, since the apex is not in reality constrained to a fixed x-y position relative to the probe. The ideal axisymmetric deformation with a sphere is metastable, since the drop would prefer to slip sideways in order to maintain a profile closest to the unperturbed state. The net effect of gravity is to pull the lighter oil upward, which exacerbates the onset of instability, even though it is a negligible amount when considering the entire drop, i.e., low Bond number ( $Bo = g\Delta\rho R^2/\sigma$ ). Strictly speaking, then, even if the microsphere is aligned precisely at the drop apex, finite disturbances would still cause horizontal interfacial displacement. This is the reason for the much larger experimental deflections than predicted, and it may also reflect on the hydrodynamics if there is significant sliding lubrication of the microsphere. For this reason it may be useful to use a flat interface or to pursue a more rigorous computation that will determine the lowest global energy profile.

A second experiment was conducted in which the anionic surfactant SDS was added to alter the interfacial tension (see Chapter 7 for more data). As expected, the  $F(z)$  compliance slope decreases significantly and by a similar factor as the interfacial tension (Fig. 5.8). The lower interfacial tension of 10 mM SDS is expected to be about 8 mN/m<sup>6</sup> compared to 52 mN/m for pure water/hexadecane,<sup>26</sup> a reduction of 6.5 times. This is close to the experimental estimate of 5.6 for the slopes measured in the range 0.2-0.4 mN/m, close to the linear spring limit at vanishingly small force but very near or after reaching the limiting separation. This assures that the same regime of interfacial deflection is probed, that is, the drop has dimpled inward and the film is wrapping about the sphere to an equal extent. At this point, the interaction is basically constant (except at the edges of the intervening film) with respect to increasing force while the film grows at constant pressure. The slight disparity may be reduced once the issue of horizontal drop displacement is precisely addressed. While FI-AFM force profiles of weaker interfacial tensions agree quite well with the model in form and magnitude,

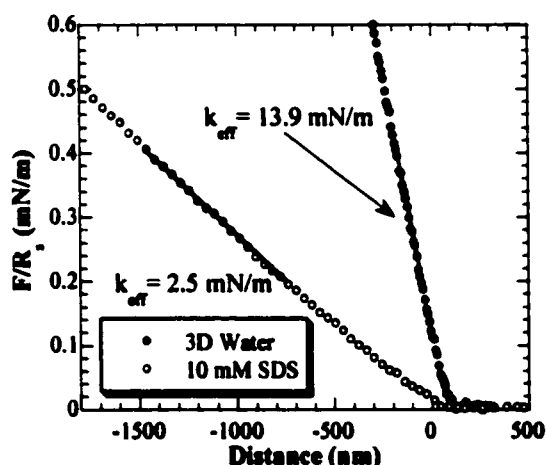


Figure 5.8: Effective drop stiffness ( $k_{\text{eff}}$ ) of n-hexadecane measured over small intervals for relative interfacial tension decrease with surfactant.

the drops with higher interfacial tensions can deform as much as five times more than predicted because the stronger drops are more likely to deform horizontally.

It must be realized at the outset that this amounts to a dynamic interfacial tension measurement, since the probing time scale is of the same order as surfactant migration and adsorption. Attempts to fit these data exactly to the equilibrium deformation model showed that the interface stiffens more with deformation than predicted for a constant interfacial tension value. This is because the interface is stretched faster than the SDS molecules can adsorb to maintain equilibrium; thus, the local interfacial tension increases. Such dynamic interfacial tension measurements and corresponding Marangoni effects are more complex to model mathematically and will be the objective of a future study.

The fact that the surface charge densities are increased through the adsorption of ionic surfactant at both the oil and polystyrene interfaces has no visible effect on the results of the FI-AFM measurements. However, unless the exact surface charge densities are known, the correct steady-state, or limiting, film thickness cannot be properly estimated. Lower interfacial tension serves to increase stability in scanning since the drop deforms more readily to the impinging sphere. The final film is thicker with larger area of interaction. Also, due to the dynamic curvature and surfactant concentration, the interfacial charge density will not be uniform throughout a force measurement which further complicates a rigorous accounting of all phenomena involved in FI-AFM.

## 5.5 Conclusions

Solutions to the augmented Young-Laplace equation explain why fluid interfacial deformation is not a linear function of applied force, so an oil drop or air bubble cannot be treated as a Hookean spring when constructing force-separation profiles from experimental data. Computing drop deformation allows the deconvolution of true separation for AFM force profiling without further instrumental modification to commercial units. FI-AFM is then quantitatively useful when implemented for parametric studies on interparticle behavior, though a large number and variety of data are required to interpret the results properly. The correct form of the  $F(z)$  data for an oil drop in water has been demonstrated but not the correct magnitude of observed deflections. Further mathematical analysis of the interfacial profile evolution and its free energy is still required for a precise understanding of why a strong interface appears to

deform more than predicted while lower interfacial tension experiments behave more ideally. It is most likely that this is merely a consequence of horizontal drop displacement that cannot be detected by conventional AFM.

The film drainage for very small separations is not properly described by our modified Reynolds lubrication. FI-AFM measures a monotonic repulsion between an oil drop and a polystyrene sphere at all external probe driving velocity and electrolyte concentrations. A dominant repulsive drainage force at very small separations would explain these observed interactions and is qualitatively feasible for a film confined by a sphere and fluid-fluid interface. This is a result of the wrapping film geometry and requires the development of a more sophisticated hydrodynamic theory to describe the interactions properly for accurate quantification of the true sphere-drop separation.

## CHAPTER 6:

### MICRO-HYDRODYNAMICS OF THIN WRAPPING FILMS IN AFM

#### 6.1 Summary

Repulsive and attractive hydrodynamic interactions are measured between an oil droplet (n-hexadecane) and various glass microspheres in aqueous environments with the atomic force microscope (AFM). The magnitude and form of the hydrodynamics in a spherically wrapping thin-film are investigated with a parametric study on external approach velocity and probe radius. The actual sphere-drop separation at closest approach can be experimentally deconvoluted in some situations from parametric data without ambiguity. Theoretical force profiles are calculated from the augmented Young-Laplace equation modified to allow two distinct hydrodynamic drainage regimes: Reynolds lubrication for thick films with slightly deformed drops, and a wrapping film condition for the indented interface. Also, an increase in film stability is directly observed as a function of velocity between a hydrophobized-glass sphere and oil, in pure water and in the presence of sodium dodecyl sulfate (SDS) below the critical micelle concentration (CMC).

#### 6.2 Background

With theoretical modeling procedures established for deconvoluting the sphere-drop separation for AFM<sup>15,70,105,106</sup> (Chapter 5, Appendices C and D), it becomes possible to investigate more complex colloidal systems and interactions. The previous chapter revealed the inadequacy of Reynolds lubrication theory to describe properly the hydrodynamics occurring within the thin, wrapping film draining between a rigid sphere and oil/water interface. This is clearly because the Reynolds equation does not consider the deforming boundary, which is readily incorporated into the analysis. While the hydrodynamics should be fairly straightforward to model and verify experimentally, the mechanism of the hydrophobic interaction(s) (a very probable component to the oil-particle behavior) is not even agreed upon (Section 2.2). Proposed empirical expressions have from one to four fitted parameters with broad value

ranges.<sup>44</sup> The addition of more fitted variables to the fluid interface (FI)-AFM model is undesirable because it reduces the certainty in a successful interpretation. Before more investigations of the hydrophobic force can be properly conducted, the thin-film hydrodynamics must be accurately quantified.

Oil drop deformations caused by an AFM probe are the result of overcoming the initial Laplace pressure (Eq. 1.1), which changes magnitude and direction as needed to balance the force applied by the rigid microsphere. The drop profile, as a whole, is very sensitive to changes in probe radius. With decreasing radius, the interface deforms over less of its area but with a higher rate of change of local curvature near the apex. Two important consequences are that (1) the cantilever bends more for a given vertical deflection of the drop, and (2) the limiting film thickness decreases (repulsive regimes) or is eliminated all together (film rupture). The trend in applied force vs. drop deformation at constant interfacial compliance, the FI-AFM equivalent of hard-wall contact, appears unaffected by its rate of change, even though the film thickness may be drastically altered relative to pseudo-equilibrium drainage.<sup>15</sup> However, the long-range, or thick-film, hydrodynamics are expected to alter both the film thickness and the drop profile to a larger degree.

The purpose of this work is to clarify the importance of hydrodynamics in film drainage, mainly from an experimental point of view, between a rigid microsphere and an oil drop in aqueous solutions. Previous results indicated that hydrodynamic effects may be more significant than normally considered, due to the increasing area in the “wrapping film” geometry of a repulsive interaction (Chapter 5). The suggestion that there are two hydrodynamic regimes, thick and thin films (though not necessarily implying the more usual connotations behind thick, thick-thin, and thin-thin films), is empirically explored by varying the external driving velocity of the scanner as well as the probe radius, which is the more direct and efficient parameter of interest to affect drainage in FI-AFM studies. Force-profile comparisons are made with the Reynolds lubrication theory, a more appropriate relation for the wrapping regime<sup>107</sup> and hydrodynamic AFM measurements against a rigid plate (mica). The present analysis establishes the need for a more rigorous mathematical treatment for quantitative exactness of the wrapping film drainage but does not attempt to compound that full complexity into the current theoretical model for colloidal interactions with a deforming interface. The effect of making a glass microsphere hydrophobic is also explored tangentially, but any solid conclusion awaits further experimentation and development of transient drainage theory for AFM.<sup>1</sup> SDS is added to

decrease interfacial tension, stabilizing the sphere-drop interaction, and more importantly to reduce the hydrophobicity of the oil drop and the coated glass.<sup>9</sup> Possible effects of dynamic interfacial tension on the accuracy of the measurements are noted but not quantitatively addressed by this investigation.

### 6.3 Experimental Methods

Force-distance profiles,  $F(z)$ , were measured in a custom sample reservoir made of glass with the pendent-drop cantilever holder in an AutoProbe® CP (ThermoMicroscopes, Sunnyvale, CA). Glass microspheres of various diameters (Duke Scientific Corp., Palo Alto, CA) were glued to gold-coated triangular cantilevers (Microlever™ A, ThermoMicroscopes) of 0.05 N/m nominal stiffness. The spheres were imaged after attachment, showing somewhat higher surface roughness (1-3 nm rms) than typical for glass and silica plates from contact AFM. Calibrating the cantilevers by resonance frequency comparison<sup>97</sup> gave values ranging from 0.048 to 0.056 N/m. The sensitivity to measured forces is typically less than 0.1 nN, but accurate interpretation is more greatly limited by the displacement scale because of interfacial mobility, especially in the horizontal plain which cannot be measured.

FI-AFM measurements were performed at the apex of an n-hexadecane drop pinned by a Teflon rim submerged in deionized and twice-distilled (3D) water or 7 mM sodium dodecyl sulfate (SDS) solution, just below the critical micelle concentration (CMC = 8 mM). SDS (>99%) and n-hexadecane (oil) were all purchased from Sigma Chemical Co. (St. Louis, MO). The majority of hydrodynamic measurements with oil were conducted in 7 mM SDS to make the interaction softer. The oil/water interfacial tension,  $\sigma$ , (52 mN/m) is reduced by almost an order of magnitude (~8 mN/m at the CMC)<sup>6</sup> without introducing the complications of having micelles in the draining film. The oil drop is hydrophilized by having a SDS monolayer with ionized sulfate head-groups exposed to the aqueous phase. There is no significant adsorption of SDS on clean silica surfaces,<sup>19</sup> but glass coated with a hydrophobic layer will adsorb a significant amount of SDS, though perhaps not a full monolayer.<sup>9</sup> Thus, adding SDS reduces the possibility of any hydrophobic attractions but also makes both surface charge densities more negative, increasing the magnitude of the double-layer repulsion while decreasing its range. Overall, the net result maximizes the importance of hydrodynamics over the effects of surface forces. But,

without exact values for the increased surface charge densities, the film thickness cannot be calculated with as much precision.

The probe was carefully aligned horizontally and vertically with a monocular microscope to within 10  $\mu\text{m}$  of center; the relatively flat radius of curvature for the unperturbed interface ( $R_d \sim 2500 \mu\text{m}$ ) does not allow better accuracy. This axisymmetric condition allows simplification of the curvature term to the augmented Young-Laplace equation (Eq. 5.1, left-hand brackets) as described previously (see Chapter 5 for details). Deforming the drop at the apex with some net force via the AFM probe redistributes the drop volume outward from the symmetry axis and away from the supporting base, even while the overall height of the drop is decreasing, as required by the equilibrium condition for the entire profile. The curvature at the three-phase interline decreases while the curvature near the top is increasing, irrespective of the assumption of constant internal pressure. The effect of constant volume, then, is to decrease the contact angle of the drop with the anchoring surface (Fig. 3.1), causing a net inward force at the interline perpendicular to the force applied by the AFM probe. If the interline does not remain pinned against this force, then it will contract.

The numerical FI-AFM algorithm does not allow the experimental  $F(z)$  data to be fitted directly to a theoretical force-separation profile, as might be preferable. Instead, the model results are plotted and compared in the  $F(z)$  format through incremental iterations of the unknown and less well-defined interaction parameters. DLVO and hydrophobic interactions as well as hydrodynamic drainage are included in  $\Pi$ . Consistent with the rest of the present work, two hydrophobic interaction parameters are used to simplify the fitting, which should be sufficient.<sup>44</sup> All other parameter values are known from supplementary sources.

The oil/water interface should behave as a constant charge density surface ( $\zeta = -16 \text{ mV}$ ) and the glass spheres as constant potential surfaces. Then, the DLVO terms include the usual non-retarded van der Waals interaction (Eq. 5.4) and the low potential electrostatic double-layer interaction for dissimilar surfaces using Debye-Hückel approximation (Eq. 6.1). The Hamaker constant,  $A$ , for hexadecane interacting with glass or alkylsilane layers across water is between 0.5 and 1 ( $\times 10^{-20} \text{ J}$ ), the exact value depending on the mixing rule used.<sup>26</sup> The pressure expression for double-layer interactions (Eq. 6.1) was derived from the potential energy equation shown by Kar *et al.*<sup>83</sup> between a constant potential surface (1) and a constant charge density surface (2):

$$\Pi_{el} = \frac{2\epsilon\epsilon_0\kappa^2 [\psi_{1o}\psi_{2o}(e^{-\kappa D} - e^{-3\kappa D}) + (\psi_{1o}^2 - \psi_{2o}^2)e^{-2\kappa D}]}{(1 + e^{-2\kappa D})^2}. \quad (6.1)$$

This agrees well with the Poisson-Boltzmann equation<sup>82</sup> when the isolated surface potentials,  $\psi_{1o}$  and  $\psi_{2o}$ , are replaced by the zeta-potentials. These were calculated from electrophoretic mobilities measured with a Rank Brothers Mark II at 25°C using the Helmholtz-Smoluchowski equation (Section 5.4). Section 4.3 details the glass probe hydrophobization.

Interaction profiles are plotted in the familiar F/R vs. a distance scale, where the net force has been normalized by the probe radius,  $R_s$ , for convenience. The fact that an equivalent system radius of curvature improperly describes the deforming interaction does not affect the calculation of DLVO forces or, explicitly, pressures. The Derjaguin approximation (Eq. 5.2) will hold because the radius of curvature at any point on the deforming interface, while always changing, is always much greater than the separation.<sup>26</sup> In some cases, it is beneficial simply to plot the force,  $F$ , in order to compare the hydrodynamic effects more directly. The hydrodynamic contribution to the drainage force will likely scale with the radius of curvature to a higher power, e.g.,  $\sim R^2$  for Reynolds theory,  $\sim R^3$  for wrapping films.<sup>107</sup>

Equations 5.4 and 6.1 are summed with the Reynolds lubrication equation (Eq. 5.6) for the first estimations of the drop-profile evolution with applied force. Results from Chapter 5 showed that even in high electrolyte concentrations (0.1 M NaNO<sub>3</sub>) and at low approach speed ( $\sim 200$  nm/s), when the film should rupture spontaneously, the interaction between polystyrene and oil was stable to coalescence, suggesting that Reynolds theory was inappropriate when the drop curvature is inverted, i.e., the wrapping film.<sup>15</sup> Even though the net system curvature,  $R_{eff}$ , and the velocity,  $dD/dt$ , are recalculated each step to maintain continuity, it was not sufficient to predict the results exactly. Furthermore, a hydrophobic attraction was initially expected to dominate at close approach for the polystyrene-oil interaction, but was never observed.

A more appropriate relation for the hydrodynamics of the dimpling droplet is one derived some years ago by Hartland, observing a much larger aluminum sphere draining a paraffin film against glycerol by gravity.<sup>107</sup> Hartland's pressure equation has been truncated here to the first term since the effect of gravity is already accounted for in Eq. 5.1:

$$\Pi_H = \frac{12\eta R_s^2}{D^3} \frac{dD}{dt} \log \left[ \frac{1 + \cos \phi}{1 + \cos \phi_c} \right]. \quad (6.2)$$

The requisite radius of curvature is recovered as that of the microsphere,  $R_s$ , and  $\phi$  describes the extent of the squeezed film as an angle about the sphere's centroid from the apex,  $r = z = 0$ ,  $D = D_0$ , to the bulk phase,  $\Pi = 0$  at  $\phi = \phi_c$  (Fig. 6.1). As with Reynolds lubrication, no-slip boundaries, parallel film flow and Newtonian fluid assumptions were made, though the

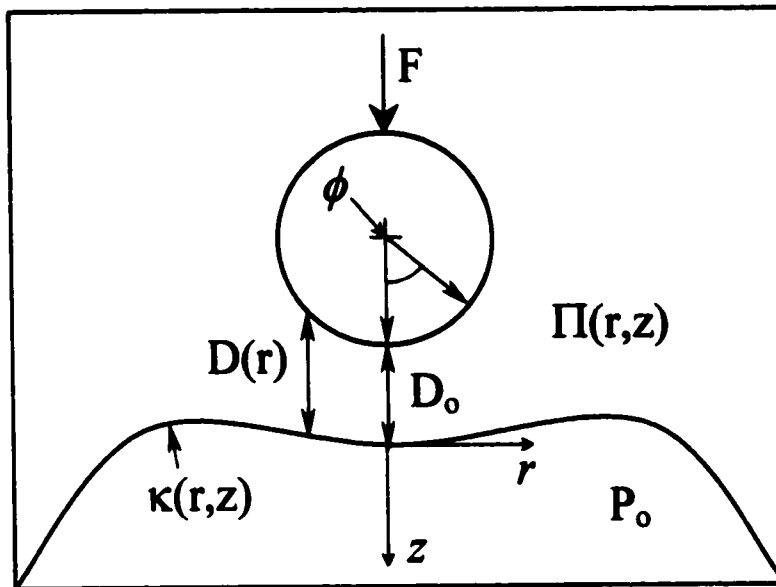


Figure 6.1: FI-AFM geometric setup: a microsphere interacting by force  $F$  axisymmetrically with a drop or bubble across the film of thickness  $D(r)$  and curvature  $\kappa(r, z)$ .

oil/water interface and perhaps any hydrophobic surface in general may allow limited slip.<sup>78</sup> Further constraints from the original work of symmetrical drainage at constant film area and thickness are clearly not representative of the dynamic nature involved, but this development should produce a closer form to the reality of FI-AFM experiments. However, Eq. 6.2 is valid even if film thickness is not constant but varies slightly with  $\phi$ . For a thick film, defined as a positive interfacial curvature (no dimple), Reynolds theory is probably more reasonable than Eq. 6.2. But at closest approach and even as soon as the drop apex has flattened, the pressure gradient within the film roughly scales with  $R_s/D$  of Reynolds theory, possibly exceeding it by orders of magnitude. Therefore, Eq. 6.2 should be substituted for Eq. 5.6 in what will be referred to as the thin-film regime, viz., after the interface dimples.

The vertical deformation of the oil/water interface from its undisturbed state,  $\Delta z$ , is added to the separation,  $D_0$ , to model scanner displacement. The result is a strictly nonlinear

“constant compliance” region for the deforming oil/water interface.<sup>15,105</sup> For many realistic situations, repulsive electrostatics and the probe radius limit the ultimate separation range accessible. That is, there is a point at which the true sphere-drop separation at the apex remains constant with increasing force, but the interface stretches to bring more of the draining film to this “limiting” thickness.<sup>70</sup> The interface wraps itself around the sphere, increasing the interfacial area, because the interfacial tension is insufficient to drain the film further against the double-layer repulsion. At this point and beyond, the fluid interface moves in truly constant compliance (though this does not mean the same thing as for a rigid surface) with a growing spherical area at constant pressure. The velocity profile increases radially outward in the film, but will also flatten out with continued wrapping of the interface. Environmental disturbances or probe surface roughness may render this condition improbable to attain experimentally. But it is also apparent that the hydrodynamic repulsion will increase significantly as the interface indents, and this will slow drainage, perhaps even eliminating film rupture when it would normally be expected under equilibrium conditions.

Conversely, if there were a long-range attraction, e.g., the hydrophobic force,<sup>12</sup> the oil and probe could be drawn together from much larger separation than standard convention might predict. A single exponential function is implemented to fit experimental data when DLVO forces alone cannot explain “snap-in” and at least one interacting surface is hydrophobic,<sup>44</sup> i.e., having a high water contact angle or, in the case of hexadecane, being immiscible. The pressure function derived from the empirical hydrophobic force equation (Eq. 5.7) has the common intensity pre-factor,  $C_1$ , and decay length,  $\lambda$ , both presumably independent of electrostatic influences. A more classic hydrophobic interaction<sup>55</sup> may be too short-ranged to be observed with FI-AFM due to the geometrical constraint on closest approach, in which case only maximum limits for the hydrophobic parameters can be inferred from data analysis. In any event, the hydrophobic term will only be added to Eq. 5.1 if the experimental conditions or resulting data warrant its inclusion, specifically, when DLVO theory underestimates an attractive response.

## 6.4 Results and Discussion

The first hydrodynamic measurements were made with a very large sphere ( $R_s = 50 \mu\text{m}$ ) against oil in SDS solution at external approach speeds of 2, 5, 10, and 20  $\mu\text{m/s}$  (Fig. 6.2).

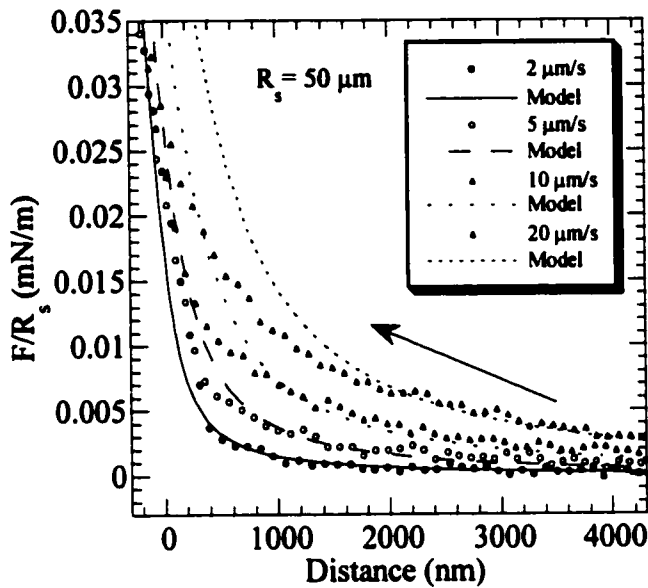


**Figure 6.2:** Glass sphere interacting with hexadecane in 7 mM SDS solution fitted with the Reynolds equation (Eq. 5.6) plotted against the total scanner displacement:  $\psi_{10} = -45$  mV,  $\psi_{20} = -16$  mV,  $\kappa^{-1} = 3.6$  nm.

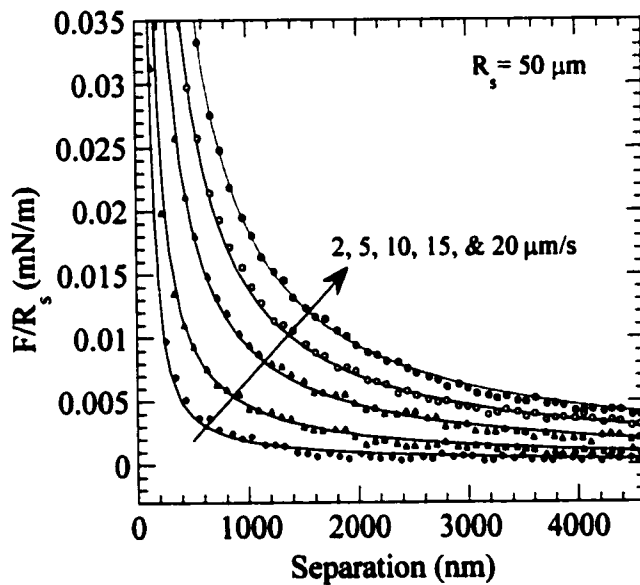


**Figure 6.3:** Glass sphere interacting with mica in water fitted with the Reynolds equation (Eq. 5.6):  $\psi_{10} = -45$  mV,  $\psi_{20} = -50$  mV,  $\kappa^{-1} = 68.4$  nm.

mode as well as when dimpled, but the deviation from a Hookean spring is much less significant allowing its reasonable usage for thick-film drainage as defined here.

Comparisons with theoretical computations using the simple Reynolds equation (Eq. 5.6) and AFM profiles taken against a freshly cleaved mica sheet (Fig. 6.3) show excellent long-range agreement. The data in Fig. 6.3 were taken merely to confirm that Reynolds lubrication is sufficient to describe the probe moving toward a flat rigid surface. Taking the 2  $\mu\text{m/s}$  as a specific example for the oil drop (Fig. 6.2), the interface begins to dimple at a separation of about 400 nm, where the data and theory diverge significantly. If hydrodynamic forces are larger in the thin, deforming film as proposed, then the interface will indeed deflect more for a given change in force, but the drainage rate will also change more rapidly such that it is difficult to make a generalization about the differences observed in Fig. 6.2. Considering that very little of the total interfacial deflection occurs while the drop has positive curvature under the thick-film condition, it is quite clear that the relations of a rigid sphere-plate interaction should hold. Of course, the interface deflects nonlinearly in this

Faster approach causes more rapid interfacial deflection so that the drainage rate is not strongly affected by the external approach velocity. The increased probing rate can only have a measurable effect at long ranges, before significant interfacial deformation reduces the actual approach velocity of the two interfaces. Since changing the approach does relatively little to alter the hydrodynamics within the region of interest, several more experiments were conducted on the same oil drop system with probe microspheres of differing radii. Again, comparing the  $2\ \mu\text{m/s}$  case for  $R_s = 15\ \mu\text{m}$  (Fig. 6.4) dimples at  $160\ \text{nm}$  separation and increasing for higher velocity under Reynolds drainage. The force profile differences approach the resolution of the AFM, so only the two extreme velocities are conveniently plotted together. It should be noted that there is a continuous increase in repulsion with velocities between  $2$  and  $20\ \mu\text{m/s}$  (not shown), and a consistently larger deviation from the Reynolds theory even at long-range. Other FI-AFM results for probe radii of  $7\ \mu\text{m}$  (Fig. 6.5) and  $0.8\ \mu\text{m}$  (Fig. 6.6) are increasingly difficult to fit accurately to either hydrodynamic model due to signal-to-noise ratios, but Eq. 6.2 appears to give a slightly better agreement in most scenarios. For the

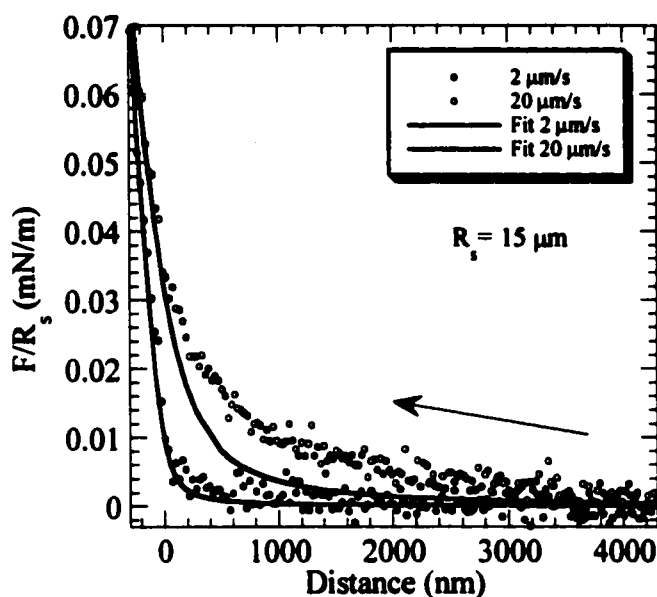


Figure 6.4: Glass sphere interacting with hexadecane in  $7\ \text{mM}$  SDS, similar to Fig. 2 with Eq. 6.2 replacing Eq. 5.6.

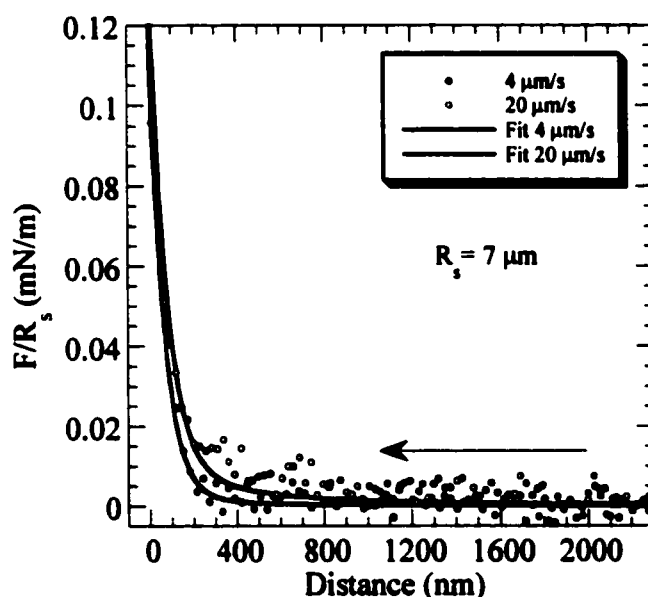


Figure 6.5: Hexadecane/glass sphere interaction fitted using Eq. 6.2.

Other FI-AFM results for probe radii of  $7\ \mu\text{m}$  (Fig. 6.5) and  $0.8\ \mu\text{m}$  (Fig. 6.6) are increasingly difficult to fit accurately to either hydrodynamic model due to signal-to-noise ratios, but Eq. 6.2 appears to give a slightly better agreement in most scenarios. For the

0.8  $\mu\text{m}$  radius, there is no resolvable difference in force profiles with increasing approach velocity, and the agreement with the model is relatively poor just prior to “contact.”

The transition from the thick-film (Eq. 5.6) to the thin-film (Eq. 6.2) drainage must be a smooth hydrodynamic process within one approach-retract cycle. Unfortunately, Hartland’s relation requires knowledge of the film’s extent, i.e.,  $\phi_c$ , which is not known experimentally, nor is it knowable *a priori* during the theoretical drop-profile calculation. This adds further complexity to the iterative modeling described above. Now, both  $dD/dt$  and  $\phi_c$  are cyclically adjusted quantities, making the numerical procedure computationally sensitive and less stable with respect to step-size.

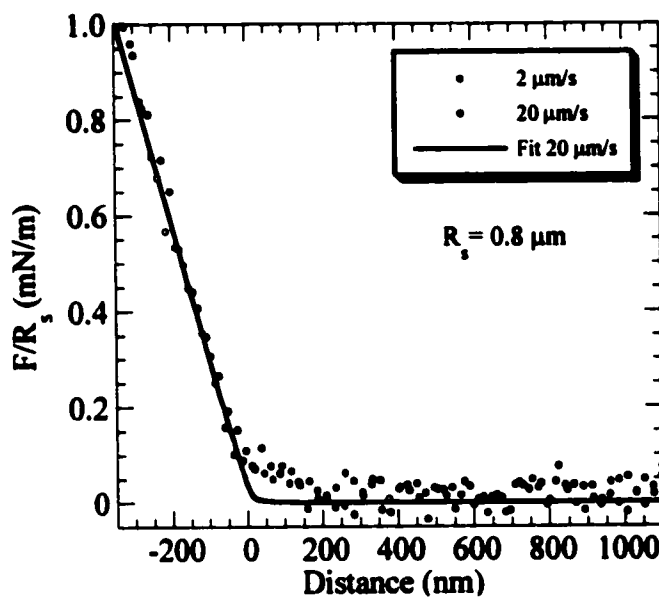
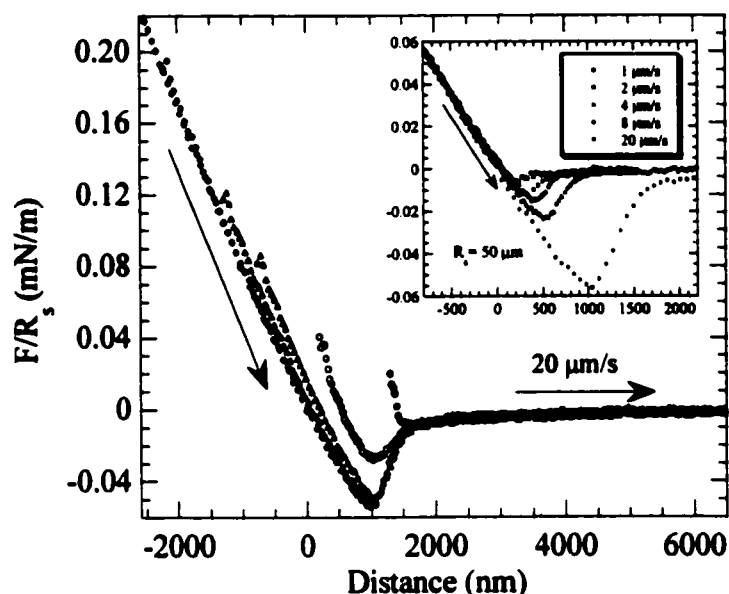


Figure 6.6: Hexadecane/glass sphere interaction in 7 mM SDS fitted using Eq. 6.2.

Another very helpful result in determining equilibrium film stability and limiting film thickness is the hydrodynamic attraction when the probe is withdrawn from the oil drop. Like the repulsion on approach, this different kind of “pull-off” force is typically small and can only be accurately measured for larger sphere radii. Hydrodynamic pull-off forces between the largest glass sphere ( $R_s = 50 \mu\text{m}$ ) and oil drop in 7 mM SDS solution increases significantly with maximum loading, or minimum film thickness achieved, up to the limiting separation (Fig. 6.7). Film rupture does not occur even when the interface is deformed beyond the point of closest approach, at forces above  $\sim 0.12 \text{ mN/m}$  for this case. The very slight increase in pull-off with maximum load at constant separation is due to radial growth of the film even though the probe never comes closer to the interface. This non-adhesion pull-off force also logically diminishes with decreasing relative velocity (Fig. 6.7, inset). Similar experiments with a smaller probe ( $R_s = 15 \mu\text{m}$ ) show that the pull-off also scales roughly with rigid sphere radius (Fig. 6.8), suggesting that this hydrodynamic attraction might also be fitted well with Reynolds theory (Eq. 5.6). Smaller spheres were incapable of resolving any attractive pull-off forces.



**Figure 6.7:** Hydrodynamic pull-off measured between a large glass sphere ( $R_s = 50 \mu\text{m}$ ) and hexadecane in 7 mM SDS solution increases with maximum loading, or minimum film thickness achieved. Film rupture does not occur, and the pull-off force diminishes with decreasing relative velocity (inset).

No long-range attractions are ever observed between glass and hexadecane in SDS solution. However, snap-ins are seen between a pure oil/water interface and a hydrophobized glass sphere followed by very large pull-off forces related to the oil/water contact angle and the wetted perimeter. The electrostatic double-layers are of sufficient thickness and density to provide some small level of stabilization against the long-range attraction, but it appears that the hydrodynamic repulsion may be equally or even more important in this system. Figure 6.9 shows increasing maximum load, or stability, with approach velocity. These results beg the question

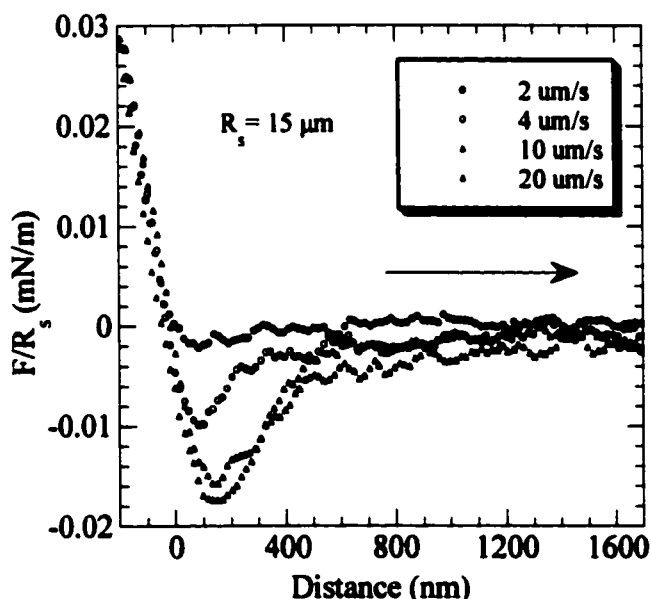


**Figure 6.8:** Hydrodynamic pull-off forces between a smaller glass sphere ( $R_s = 15 \mu\text{m}$ ) and hexadecane in 7 mM SDS solution scale roughly with  $R_s$ . Raw data were 5-pt averaged due to poor single-to-noise ratio.

of why the polystyrene probe under similar conditions was not attracted to the oil.<sup>15</sup> The larger polystyrene sphere ( $R_s = 8.5 \mu\text{m}$ ) would have been more hydrodynamically stabilized, but this does not seem to be sufficient. The polystyrene has greater surface roughness and may be more

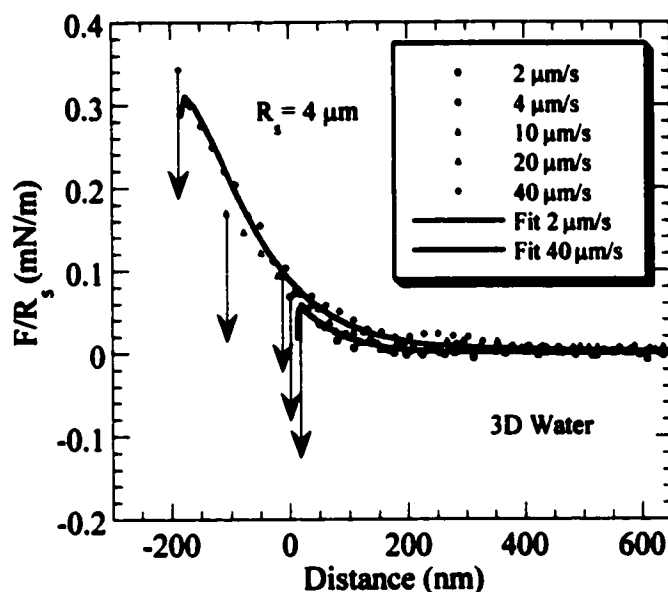


**Figure 6.9:** OTES-coated glass sphere ( $R_s = 4 \mu\text{m}$ ) interacting with hexadecane in water:  $\psi_{10} = -35 \text{ mV}$ ,  $\psi_{20} = -16 \text{ mV}$ ,  $\kappa^{-1} = 68.4 \text{ nm}$ . Fit includes Eqs. 5.7 and 6.2. Hydrodynamic repulsion works against the long-range attraction between these two hydrophobic interfaces:  $C_1 = -5.1 \text{ mN/m}$ ,  $\lambda = 3 \text{ nm}$ .

hydrophilic than initially believed due to ionized sulfate surface groups. Also, the electrostatic condition of two constant surface charge densities is a more repulsive situation at close approach than the mixed boundary conditions of the silanized glass and oil drop. However, the assumption of constant surface potential for the OTES-glass covered with SDS is probably no longer valid. In any event, the experimental results taken together warrant further investigation.

When SDS was added to the OTES-glass experiment, the maximum stable load achievable increased by an order of magnitude, but the trend with approach velocity is uncertain (Fig. 6.10). There is experimental error of the same order as the hydrodynamic effect on the force limit of film stability in the presence of surfactant. The differences in the interaction parameters for Figs. 6.9 and 6.10 are not defined well enough to comment quantitatively, but more important is the question of the hydrophobic effect. The data from the pure water profiles (max. loads:  $0.056 \text{ mN/m}$ ,  $2 \mu\text{m/s}$ ;  $0.069 \text{ mN/m}$ ,  $4 \mu\text{m/s}$ ;  $0.10 \text{ mN/m}$ ,  $10 \mu\text{m/s}$ ;  $0.18 \text{ mN/m}$ ,  $20 \mu\text{m/s}$ ;  $0.36 \text{ mN/m}$ ,  $40 \mu\text{m/s}$ ) are fitted reasonably well with  $C_1 = -5.1 \text{ mN/m}$  and  $\lambda = 3 \text{ nm}$  (Eq.

5.7), even though the theory predicts a smoother attraction, not an instantaneous snap-in as observed. The lowest velocity is fitted almost exactly by the model snap-in, but the maximum loads increasingly underestimate the data. Only a very slight change in one parameter, e.g.,  $C_1 =$

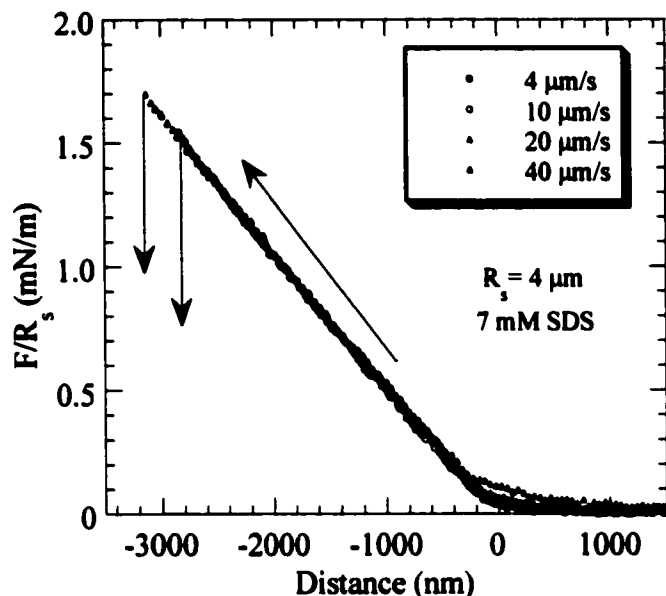


**Figure 6.10:** OTES-glass sphere ( $R_s = 4 \mu\text{m}$ ) interacting with hexadecane in 7 mM SDS is much more stable to film rupture, having increased in interfacial charge densities and reducing the hydrophobicity.

-5 mN/m, leads to significant overestimates of snap-in load. The addition of SDS to 7 mM was expected to completely stabilize the interaction against coalescence, but this was not the case (Fig. 6.10). In order to realistically fit these data, the electrostatic boundary conditions must be known with more certainty. It is also possible that the OTES-glass is not completely hydrophilized with a monolayer of surfactant, so that there is still some long-range attraction beyond the van der Waals force, or an electrostatic correlation

force is again at play (Chapter 4).

## 6.5 Conclusions

The experimental AFM design for oil drops and air bubbles requires at least two hydrodynamic relations to describe the thick Reynolds film and the thin, wrapping film regimes. The present model is more reasonable than the previous one<sup>15</sup> because the dynamic geometry of the interaction area in FI-AFM has been explicitly accounted for in the hydrodynamic pressure profile. The hydrodynamic repulsion between rigid microspheres and deforming interfaces can be the controlling factor in film stability and may be even more complex than the current analysis supposes.

FI-AFM profiling reveals a monotonic repulsion between an n-hexadecane drop and glass sphere in 7 mM SDS solution regardless of probing velocity and maximum loading. When the approach velocity drops to zero, the films remain stable. Significant hydrodynamic attraction

is observed as a pull-off force (mN/m) between sphere and oil drop which scales with probe radius and velocity. This pull-off information can be used to infer the minimum separation achieved during an experiment. Thin-film hydrodynamics also aid stabilization against long-range attractions between hydrophobic interfaces in water, OTES-glass and hexadecane. The addition of SDS to 7 mM greatly increases interfacial stability to AFM probing but is not sufficient to eliminate film rupture at much higher loading.

## CHAPTER 7:

### DYNAMIC INTERFACIAL TENSIONS WITH FI-AFM

#### 7.1 Summary

The current objective is to show the general trend of apparent oil drop stiffness with actual interfacial tension mediated with anionic surfactant, sodium dodecyl sulfate (SDS). While the research is on-going, our initial experimental results suggest that fluid interface-atomic force microscopy (FI-AFM) is capable of measuring global as well as local changes in interfacial tension. AFM is sensitive enough to distinguish variances as small as and perhaps much smaller than existing surface tensiometers and is likely to prove well-suited for dynamic interfacial tension measurements, including a nanoscale instrument for investigating Marangoni and Gibbs elasticity effects.<sup>108</sup> Strictly speaking, FI-AFM is a dynamic interfacial tension technique, since the probing time scale can be of the same order as that of surfactant migration and adsorption. Once these issues are accounted for explicitly within the current model framework (Chapters 5 and 6), by no means a trivial exercise, FI-AFM is expected to allow precise dynamic measurements to be accomplished with alacrity.

#### 7.2 Background and Experimental Methods

The FI-AFM procedures for an oil drop/rigid particle interaction have already been outlined in detail in Chapters 5 and 6 and Appendix C. The following experimental data and fitted models are different from the previous studies only in that the interfacial tension,  $\sigma$ , is now treated as the parameter of interest. In some instances the value of  $\sigma$  is known, and in any event it may be measured at equilibrium on a much larger scale with the drop-weight or other method. However, the concept of the present procedure is to establish a practical routine for measurement changes in interfacial tension on a micro- or nano-scale, perhaps allowing access to local dynamic interfacial tension effects.

As before, force-distance measurements were performed at the apex of the drop (n-hexadecane in aqueous solutions) to satisfy the axisymmetry condition imposed on the form of

the augmented Young-Laplace expression of Eq. 5.1. The initial concentration of SDS (Sigma Chemical Co., St. Louis, MO). was adjusted by volumetric additions to the AFM liquid cell of stock prepared with deionized and twice-distilled (3D) water. The fact that surface charge densities are increased through ionic surfactant adsorption at hydrophobic interfaces (e.g., hexadecane, polystyrene, OTES-glass) should have no visible effect on the results for interfacial tension measurements here. However, unless the exact electrostatic double-layer boundary conditions are known, the correct aqueous film thickness cannot be properly calculated, but this is insignificant to the quantification of  $\sigma$ . In any reasonable scenario, this will amount to the order of ten nanometers, much less than the radii of curvature for the colloidal AFM experiments. Lower interfacial tension serves to increase stability in scanning, since the drop deforms more readily to the impinging sphere. Thus, the film at a given load is thicker with larger area of interaction. Also, due to the dynamic curvature and surfactant concentration, the charge density will not necessarily be uniform over the entire interfacial profile or throughout a force measurement, further complicating a rigorous account of the multiple phenomena involved.

### 7.3 Results and Discussion

Figure 7.1 shows an *in situ* interfacial tension titration, adding SDS to the same polystyrene/water/hexadecane interaction from Chapter 5 for the purpose of quantifying relative changes in  $\sigma$  by smaller increments than demonstrated in Fig. 5.8. Except at very low concentrations where snap-in occurred at relatively small loads, the interfacial stiffness, and thus  $\sigma$ , decreases when adding SDS, indicated by the slope of the compliance line. Of course, the compliance portions of these profiles are not strictly linear, but the

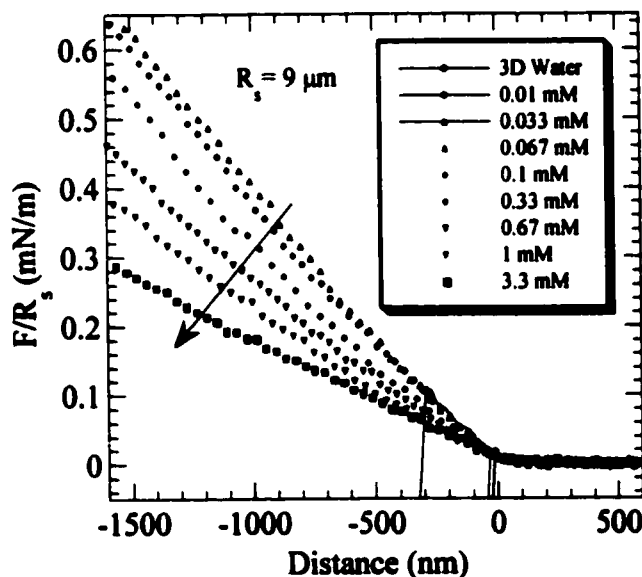


Figure 7.1: FI-AFM of a polystyrene sphere pushing against n-hexadecane in aqueous solutions of SDS. Drop stiffness decreases with increasing SDS concentration.

trend is still the same. Again, a rough estimate is quickly made from the ratio of the slopes fitted over some small region. There is essentially no difference between the AFM data ( $1.55 \pm 0.1$ ) and the ratio of 1.62 for two independently measured values (49.9 and 30.8 mN/m at 0.1 and 1 mM, respectively, from the drop-weight method); the experimental deviation, if there is one, is much less than that previously seen (underestimate of Chapter 5). This shows excellent agreement considering the inaccuracies incurred by estimating from the slopes and the fact that the exact liquid cell concentration is not known. The SDS concentration varies with evaporation during an experimental run, and interfacial tension is very sensitive in this range where differences are most readily measured. A further complication is the obvious movement of the three-phase interline at some higher surfactant concentrations. This brings into question the assumed boundary condition of a pinned interline, which is a good one for higher values of  $\sigma$ . This interline slipping may account for the experimental difficulty of fitting data to the current drop deformation model.

Other  $\sigma$  titrations were conducted with glass microspheres to reduce the uncertainty in the actual “contact area” during testing. Because the large polystyrene spheres are more irregular, a better experiment for sensitivity to subtle fluctuations in  $\sigma$  would be conducted with smoother probes, e.g., silica. This also reduces the likelihood of a long-range hydrophobic interaction. The data in Fig. 7.2 focus more on the intermediate SDS concentrations and shows smoother profiles than with the rougher polystyrene

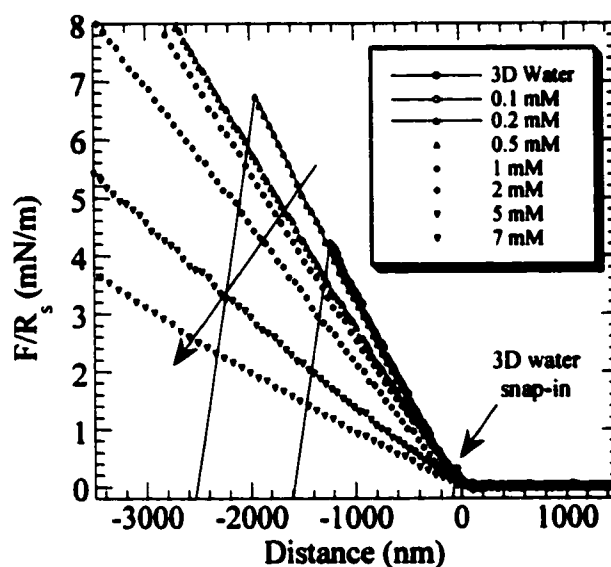


Figure 7.2: Glass sphere ( $R_s = 4 \mu\text{m}$ ) against hexadecane ( $R_d \approx 5 \text{mm}$ ) in aqueous SDS solutions.

probe. Little or no SDS will adsorb to the silica, but its surface charge density is high enough to maintain film stability for smaller probe radii. Therefore, higher pressure may be applied to deforming the interface and thinner wrapping films are achieved over the polystyrene system. The result is that film rupture can be forced at higher SDS concentrations (0.1 and 0.2 mM) than expected from models that do not account for increased surface charge.

Using the model developed in Chapter 5, the predictions for compliance slopes may be compared to experimental data for determining the efficacy of micro-tensiometry with the current state of FI-AFM. Figure 7.3 assumes no hydrophobic interaction and reveals no snap-ins to contact. It is obvious that the trend is very similar to those found in experiments (Figs. 7.1 and 7.2), even though the slopes do not match exactly to those SDS concentrations with known  $\sigma$ . The relative trend of decreasing slope with decreasing  $\sigma$  is always consistent with

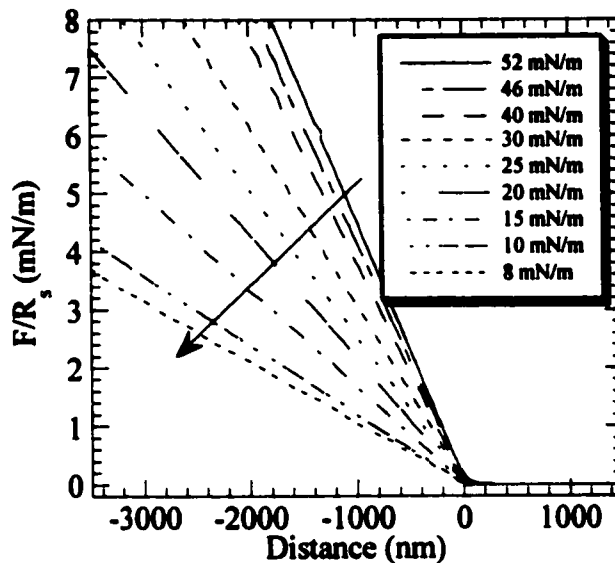


Figure 7.3:  $F(z)$  profiles predicted for various interfacial tensions,  $\sigma$ , (legend) from the Young-Laplace equation (Eq. 5.1):  $\psi_{1o} = -16$  mV,  $\psi_{2o} = -45$  mV,  $R_d = 2500$   $\mu\text{m}$ ,  $R_s = 4$   $\mu\text{m}$ .

observations and will be quantitatively exact when the experimental design for the drop formation is perfected (see Chapter 8). Estimates to within a few percent can be easily made for intermediate SDS concentrations. For example, data for 5 mM SDS suggest the slope is just under 15 mN/m, and it is about 23 mN/m for 2 mM SDS. The error, of course, can be easily determined from drop-weight measurements. One very important point to note is that the slopes at higher loads, i.e., for large film areas, appear to be unaffected by hydrodynamic effects. In other words, this type of measurement for film “stiffness” is very much like an indentation study on a solid plate that is not infinitely rigid. Also, the magnitude of surface forces is not really an issue; that is, they do not affect the contact slope. Double-layer forces are only included in Eq. 5.1 to model these experiments as a stable measurement, viz., a constant film thickness, and the van der Waals and other interactions may be completely ignored unless film rupture is being investigated for characteristic applied loads.

A third experiment shows that there can be a time-dependence involved in measuring interfacial tension with AFM. The profiles shown in Fig. 7.4 have been normalized against the slope of the first curve (1<sup>st</sup>) at peak loading such that it appears to approach an infinitely rigid wall. In this way, the very minor differences are amplified for viewing on a somewhat arbitrary distance scale which is intermediate to scanner displacement and actual probe-drop separation

(see Chapter 5 and Fig. 5.3 for further details). If consecutive measurements are taken within a few seconds of each other, the interfacial tension appears to decrease from stretching the interface and allowing more surfactant to crowd onto the surface before the drop relaxes to its equilibrium shape. Ionic surfactant adsorption takes place quite rapidly, however, the results in Fig. 7.4 indicate a total change in  $\sigma$  of the order of 1 mN/m. While the local interfacial tension can be expected to change as much as 10 mN/m from an instantaneous area expansion, it is more

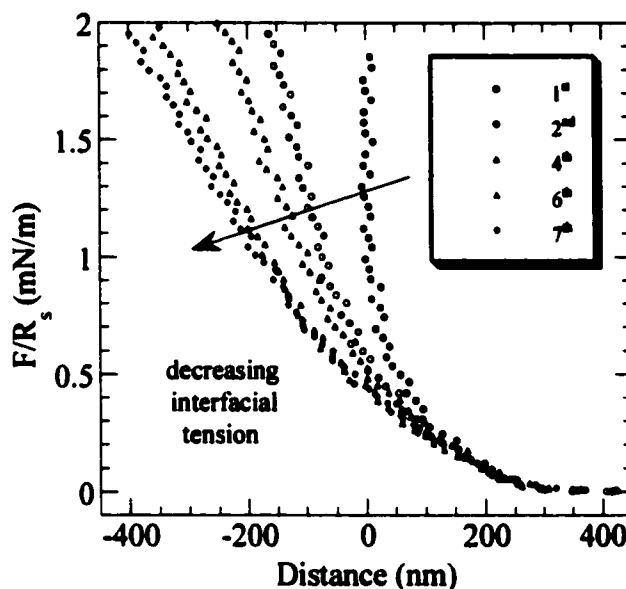


Figure 7.4: Dynamic FI-AFM effects with a hexadecane drop stiffness in 10 mM SDS using a polystyrene probe ( $R_s = 8.5 \mu\text{m}$ ). Each curve was produced in 1 s and shows decreasing stiffness from right to left.

likely that over the interval of a single AFM probing a much smaller change will be detected. However, these deviations from equilibrium need not invoke a truly dynamic interfacial tension to be explained. These observations may also be due to the drop, once pushed out of its equilibrium profile, changing shape via three-phase interline movement. This was not a problem for hydrodynamic and surface force measurements because the magnitudes of the applied forces and drop deformations were small. Interline slipping is a more likely scenario with the higher loads and certainly with the lower  $\sigma$  values for micro-tensiometry. In either event, more detailed calculations and appropriate experimentation are required to make a sound conclusion. Regardless of the outcome, it is clear that FI-AFM may, in fact, be utilized to probe dynamic events specifically related to surfactant adsorption and desorption with second to microsecond resolution and with greater than 0.1 mN/m sensitivity (not to be confused with force per radius). As a side note, it is interesting that these dynamic effects were only distinctive above the critical micelle concentration (CMC  $\approx 8$  mM). Further investigations are needed to form a reasonable hypothesis about any connection with micellization, surfactant packing at the interface, or other possibilities.

## 7.4 Conclusions and Recommendations

This chapter shows proof of principle for a new type of micro-tensiometry for noninvasive interfacial tension studies, but the present experimentation is not yet optimized for analytical accuracy. The most important issue, besides those discussed in the previous chapters, is one of the three-phase interline boundary condition. The theoretical model used above does no iteration on the interfacial contact angle and does not allow the interline to slip. It can be quite easily shown that if the interline were to slip as little as a few microns during the course of one profile acquisition, this would translate into the same order of magnitude in displacement deviation at the oil drop apex. Unfortunately, the precise calculations required for conducting an accurate investigation of this effect is costly in computation time and requires significant modification of the FI-AFM model. The easiest approach should be to run tests on various anchoring substrates that confine the shape of the oil drop to be studied. Overall drop size, substrate roughness and surface energy must all be investigated parametrically to determine the most efficient method of holding the interface of interest to match theoretical conditions.

The pseudo-equilibrium Young-Laplace model (wrapping film hydrodynamics included) suggests that the oil/water interfacial tension (in the presence of SDS) may change slightly during a single force probing and with repeated probing over short time intervals. This could be because the interface is stretched faster than the SDS molecules can adsorb to maintain equilibrium; thus, the local interfacial tension increases with deformation. Oil/water/substrate interline slipping could play a significant role in complicating the measurements and must be ruled out or sufficiently reduced in order to continue with quantitatively useful experiments. While AFM is quite capable of making dynamic interfacial tension measurements, the corresponding Gibbs elasticity and Marangoni effects are complex to model mathematically and will be the objectives of future study.

## **CHAPTER 8:**

### **CONCLUSIONS AND RECOMMENDATIONS**

#### **8.1 Overview of Results**

We have shown throughout the previous chapters that the AFM is an appropriate instrument for the quantitative measurement of a number of interactions between a rigid sphere and a highly deforming fluid interface, specifically, that of an oil drop (hexadecane) in aqueous environments. What follows is a condensed list of the major contributions of this dissertation to the advancement of interfacial science and the ever-enlarging toolbox of scanning probe microscopy:

1. The first, proof-of-principle AFM experiments determining the interaction of an unfused toner-ink particle with an oil drop under water were performed. They showed that while adsorbed cationic starch inhibits oil-toner coalescence by electrosterically resisting film drainage, the addition of a lipophilic surfactant to the oil (a.k.a., agglomerating or densifying agents) eliminated the imparted stability. The first direct measures of induction (film drainage and rupture) times were also accomplished on a colloidal scale with the same AFM toner probe.
2. The technique of electrolyte titration (Chapter 4) was developed as a colloidal AFM probe. A parametric study to fit multiple surface forces unambiguously via a theoretical plot of the characteristic snap-in distance vs. electrolyte concentration curve was carried out. These calculations provided the template for determining two or more unknown interaction parameters from correlated data points.
3. Our investigations into the long-range attractions between hydrophobic, chemically-modified surfaces (i.e., alkyl-silanated silica sphere and plate) supported the still-emerging consensus that the reputed “hydrophobic” interaction is a combination of phenomena. The most likely scenario was shown to include at least two long-range effects.

4. It was shown that cross-linked films of silane-coupling agents exhibit a secondary electrostatic correlation that scales exponentially with half the Debye length, is independent of the electrostatic double-layer force, and resembles data of other surface forces experiments that may have mistakenly lumped this effect into an empirical hydrophobic force. There is still a long-range attraction observed that is totally independent of electrostatic screening and is more correctly associated with the so-called hydrophobic effect.
5. It has been shown that a fluid interface, like that of an oil drop or air bubble in water, does not behavior as a simple linear spring, such as has been assumed in the past. Our development of fluid interface-atomic force microscopy (FI-AFM) established the theoretical procedures and experimental justifications for constructing the true force vs. separation profile for a fluid interface being deformed by an impinging sphere. The augmented Young-Laplace equation defines the equilibrium interfacial profile for a given applied force, allowing the deconvolution of the otherwise inaccessible separation.
6. Our first FI-AFM experiments showed that thin film hydrodynamics is more complex than the simplified Reynolds theory alone. Once the draining film and interface begin to wrap around the rigid, spherical AFM probe, the Reynolds equation no longer describes the behavior well. Furthermore, the qualitative trends in force profiles as a function of the externally-driven probing velocity are not appropriate for straightforward interpretation of the thin film hydrodynamics.
7. It has been shown that the hydrodynamic regimes accessible to FI-AFM can be reasonably separated into a thick film component that dominates outside the range of colloidal interactions, when the fluid interface maintains a positive curvature (i.e., convex, no dimpling, no wrapping film), and a thin film relation that accounts for the wrapping film geometry manifest at small separations. These same experiments demonstrated that hydrodynamic forces alone can be the determining factor in maintaining film stability during FI-AFM experimentation.
8. The first known observations of hydrodynamic pull-off forces with FI-AFM were made for completely stable interactions, that is, no film rupture and wetting took place. These

measurements might be used for independent extrapolation of the closest separation achieved at the highest applied load, i.e., the turn-around point in the force profile.

9. The ability of FI-AFM to measure static interfacial tension with modest accuracy (within a few tenths of mN/m, or dynes/cm) has been demonstrated. While this micro-tensiometry approach is novel for its size scale, it is also capable of dynamic measurements where surfactant adsorption and interfacial tension gradient effects may be observed.

## **8.2 Recommendations for Future Work**

There are, of course, a few minor variations on the previous experiments that will be highly useful to pursue, as well as some more complex but very logical tangents to explore using FI-AFM and related measurements:

1. The fact that the presence of cationic starch appears to have no effect on air flotation for recycling paper remains a mystery in light of its deleterious effect on oil-assisted agglomeration, as seen in Chapter 3. FI-AFM is clearly suited to delve into this issue via a comparative study with air bubbles in the presence and absence of cationic starch solutions. Similar to our previous work, a toner particle or a more ideal polystyrene sphere would be the AFM probe particle to deform the air/water interface. The hope would be to find some detailed difference between the oil and air cases in the force profiles that would suggest the form of the adlayers or long-range interactions that causes stability and coalescence, respectively.
2. It remains to be shown if the so-called hydrophobic force is just one example of a more general "solvophobic" effect that occurs between interfaces of poor chemical compatibility with the intervening medium. Some data exist in the literature to suggest this possibility (see Section 2.2), but a detailed AFM (or SFA) study on low surface energy materials in other polar media is still called for to explore the issue further. The reversed situation should also be investigated, viz., a nonpolar fluid with similarly incompatible surfaces. The latter need not be highly polar, though that is the more common option; however, a general parameter like solubility or free energy of mixing may turn out to be the more appropriate factor.

These studies will also provide a better basis for interpretation of the hydrophobic interaction mechanism, specifically.

3. The observation of an electrostatic correlation not associated with overlapping double-layers between chemically hydrophobized silica requires more attention. The cause of this very long-range attraction has been associated with some level of domain ordering in the cross-linked silane layers, probably a semi-regular lattice of alternating dipolar or charged regions (Chapter 4). This presents a highly complex problem of deconvolution between multiple interactions of electrostatic, or electrodynamic, origin. One simplification on the experiment would be to move away from hydrophobic treatments to other organo-functional moieties of the siloxane chemicals. If the correlation effect has something to do with the silane-coating process, it should manifest itself with amino or ethylene oxide films made from their associated trialkoxysilane molecules as well. It may also be possible to force a more strongly differentiated domain structuring by blending two organo-silane species with high partition coefficients for one another.
4. Another straightforward method of exploring thin-film micro-hydrodynamics with FI-AFM would be to study a wide range of fluid medium viscosities. This immediately complicates the issue of comparing colloidal interactions in lesser studied fluids, but various steps can be taken to reduce their effects. Using thicker Newtonian fluids is also a practical way of slowing down transient attractive interactions, like the long-range snap-in to contact. Thus, weak cantilevers may still be used for the best force sensitivity in equilibrium and viscous measurements with improved resolution of temporal events.
5. The most useful instrumental improvement would be a precisely machined liquid cell for FI-AFM. The goal is to have a user-friendly piece for analytical grade measurements for interfacial tension, but this would also make any FI-AFM experiment easier to accomplish. The critical design feature for the new cell is a rigid and well-controlled fluid volume for creating a reproducible droplet or bubble on the same interline perimeter, like a syringe needle with an orifice of the order of 100  $\mu\text{m}$ . There are many fine-tuning issues, such as fluid delivery, pressure control, and needle tip geometry, that will have to be addressed in order to get a substantial benefit over the simple cell design already being used.

6. The critical micelle concentration (CMC) of a surfactant could then be determined quite accurately by the force titration of interfacial tension. Clearly, other surfactants, especially cationic ones, would be of interest not only for CMC studies but also to see the effects on thin-film stability.
7. Theoretical considerations for dynamic interfacial tension examinations should be studied for feasibility regarding the current FI-AFM development. It seems that the usual but high-speed force profile could accomplish some type of surfactant adsorption analysis, but there are some obvious complications mentioned previously (Chapters 6 and 7). Another similar possibility could be an oscillating cantilever, or droplet, instead of using a single, transient scan. This would bring the study into the frequency domain, probably on the same scale as pulsed-force microscopy (PFM): 0.1-5 kHz.
8. This leads us to the possibility of determining surface charge density changes, if not absolute values, with FI-AFM. Of course, independent measurements of zeta-potentials or surface charge densities need to be done for oil drops in solution first. Microelectrophoresis is the most widely used and readily available technique for quantifying the effect of the electrostatic double layer on the true film thickness which is inferred via theoretical modeling from AFM data.
9. The initial zeta-potential experiments should be of n-hexadecane droplets in SDS solutions to utilize the extant force profiles for determining the precise magnitude and effect of increasing surface charge densities on the draining film thickness in FI-AFM. This is the key equilibrium information required to begin interpreting the hydrodynamic pull-off forces and distances with quantitative accuracy.
10. In order to model the event(s) of hydrodynamic pull-off during an FI-AFM experiment, the current programs (Appendices C and D) may require the implementation of an altered or completely different hydrodynamic pressure relation. The appropriateness of these routines, as they exist, should be tested against the already available data (Chapter 6). If any shortcomings become immediately evident, a new hydrodynamic equation could be derived from the Navier-Stokes equation, just as the other relations were.

11. It would be instructive to test different oils of similar surface tension but differing chemistry or density. In this way, interline contact angle, or slipping, and gravimetric data are accessible for independent investigation.
12. A standardized FI-AFM liquid cell also provides a new method for measuring the cantilever spring constant, which is already an arduous task necessary for quantitative force measurements. Establishing a new protocol, including the testing chemicals and conditions, may take a substantial amount of trial and error. The most useful system would not contaminate the tip with anything difficult to remove. This might constrain the test to non-wetting fluids or high surfactant concentrations levels. The benefits in such a development lay in removing the need to model the dynamic mechanics of a non-ideal cantilever geometry and in providing an equilibrium calibration method for extremely weak cantilevers.
13. Finally, another concept of technological miniaturization that would be feasible for FI-AFM is a nano-fiber balance. The surface or interfacial tension force exerted along the wetted perimeter of a fiber attached to a cantilever could be measured with sensitivities at least a few orders of magnitude below electrobalance capabilities. The ultimate measurement would be with a bucky tube, or a small bundle, but the more practical test could use a micron-scale fiber on a stiffer cantilever for the simplest water contact angle/surface tension measurement.

**LIST OF REFERENCES**

1. Butt, H.-J. "A Technique for Measuring the Force between a Colloidal Particle in Water and a Bubble." *J. Colloid Interface Sci.* 1994, 166(1): 109.
2. Ducker, W. A.; Xu, Z.; Israelachvili, J. N. "Measurements of Hydrophobic and DLVO Forces in Bubble-Surface Interactions in Aqueous Solutions." *Langmuir* 1994, 10(9): 3279.
3. Fielden, M. L.; Hayes, R. A.; Ralston, J. "Surface and Capillary Forces Affecting Air Bubble-Particle Interactions in Aqueous Electrolyte." *Langmuir* 1996, 12(15): 3721.
4. Mulvaney, P.; Perera, J. M.; Biggs, S.; Grieser, F.; Stevens, G. W. "The Direct Measurement of the Forces of Interaction between a Colloid Particle and an Oil Droplet." *J. Colloid Interface Sci.* 1996, 183(2): 614.
5. Snyder, B. A.; Aston, D. E.; Berg, J. C. "Particle-Drop Interactions Measured with Atomic Force Microscopy." *Langmuir* 1997, 13(3): 590.
6. Hartley, P. G.; Grieser, F.; Mulvaney, P.; Stevens, G. W. "Surface Forces and Deformation at the Oil-Water Interface Probed Using AFM Force Measurement." *Langmuir* 1999, 15(21): 7282.
7. Preuss, M.; Butt, H.-J. "Measuring the Contact Angle of Individual Colloidal Particles." *J Colloid Interface Sci* 1998, 208(2): 468.
8. Ecke, S.; Preuss, M.; Butt, H.-J. "Microsphere Tensiometry to Measure Advancing and Receding Contact Angles on Individual Particles." *J. Adhesion Sci. Technol.* 1999, 13(10): 1181.
9. Preuss, M.; Butt, H.-J. "Direct Measurement of Particle-Bubble Interactions in Aqueous Electrolyte: Dependence on Surfactant." *Langmuir* 1998, 14(12): 3164.
10. Wiesendanger, R. *Scanning Probe Microscopy and Spectroscopy: Methods and Applications*; Cambridge University Press: Great Britain, 1994.
11. Hunter, R. J. *Foundations of Colloid Science*; Oxford University Press: New York, 1987; Vol. 1.
12. Vogler, E. A. "Structure and Reactivity of Water at Biomaterial Surfaces." *Adv. Colloid Interface Sci.* 1998, 74: 69.
13. Aston, D. E.; Berg, J. C. "Fluid Interfacial Separations for Secondary Fiber Recovery as Probed with Atomic Force Microscopy." *J. Pulp Paper Sci.* 1998, 24(4): 121.

14. Aston, D. E.; Berg, J. C. "Long-Range Attraction between Silanated Silica Materials Studies by an Electrolyte Titration with AFM." *Colloids Surf. A* **2000**, *163(2-3)*: 247.
15. Aston, D. E.; Berg, J. C. "Quantitative Analysis of Fluid Interface Atomic Force Microscopy." *J. Colloid Interface Sci.* **2001**, *235(1)*: 162.
16. Aston, D. E.; Berg, J. C. "Thin-Film Hydrodynamics in Fluid Interface-Atomic Force Microscopy." *Ind. Eng. Chem. Res.* **2001**, *in review*: .
17. Ducker, W. A.; Senden, T. J.; Pashley, R. M. "Direct Measurement of Colloidal Forces Using an Atomic Force Microscope." *Nature* **1991**, *353(6341)*: 239.
18. He, M.; Szuchmacher-Blum, A.; Aston, D. E.; Buenviaje, C.; Overney, R. M.; Luginbühl, R. "Critical Phenomena of Water Bridges in Nanoasperity Contact." *J. Chem. Phys.* **2001**, *114(3)*: 1355.
19. Thibaut, A.; Misselyn-Bauduin, A.; Grandjean, J.; Broze, G.; Jérôme, R. "Adsorption of an Aqueous Mixture of Surfactants on Silica." *Langmuir* **2000**, *16(24)*: 9192.
20. Preuss, M.; Butt, H.-J. "Direct Measurement of Forces between Particles and Bubbles." *Int. J. Miner. Process.* **1999**, *56(1-4)*: 99.
21. Yakubov, G. E.; Vinogradova, O. I.; Butt, H.-J. "Contact Angles on Hydrophobic Microparticles at Water-Air and Water-Hexadecane Interfaces." *J. Adhesion Sci. technol.* **2000**, *14(14)*: 1783.
22. Basu, S.; Sharma, M. M. "Measurement of Critical Disjoining Pressure for Dewetting of Solid Surfaces." *J. Colloid Interface Sci.* **1996**, *181(2)*: 443.
23. Aveyard, R.; Binks, B. P.; Cho, W.-G.; Fisher, L. R.; Fletcher, P. D.; Klinkhammer, F. "Investigation of the Force-Distance Relationship for a Small Liquid Drop Approaching a Liquid-Liquid Interface." *Langmuir* **1996**, *12(26)*: 6561.
24. Snyder, B. A.; Berg, J. C. "Liquid Bridge Agglomeration: A Fundamental Approach to Toner Deinking." *Tappi J* **1994**, *77(5)*: 79.
25. Snyder, B. A.; Berg, J. C. "Deinking Toner-Printed Paper by Selective Agglomeration." *Pulp Paper Can.* **1996**, *97(9)*: 38.
26. Israelachvili, J. N. *Intermolecular and Surface Forces*. 2nd ed.; Harcourt Brace & Co.: London, 1992.
27. Hato, M. "Attractive Forces between Surfaces of Controlled "Hydrophobicity" across Water: A Possible Range of "Hydrophobic Interactions" between Macroscopic Hydrophobic Surfaces across Water." *J. Phys. Chem.* **1996**, *100(47)*: 18530.

28. Craig, V. S. J.; Ninham, B. W.; Pashley, R. M. "Study of the Long-Range Hydrophobic Attraction in Concentrated Salt Solution and Its Implications for Electrostatic Models." *Langmuir* **1998**, *14*(12): 326.
29. Kokkoli, E.; Zukoski, C. F. "Effect of Solvents on Interaction between Hydrophobic Self-Assembled Monolayers." *J. Colloid Interface Sci.* **1999**, *209*(1): 60.
30. Ninham, B. W. "On Progress in Forces since the DLVO Theory." *Adv. Colloid Interface Sci.* **1999**, *83*(1-3): 1.
31. Claesson, P. M.; Blom, C. E.; Herder, P. C.; Ninham, B. W. "Interactions between Water-Stable Hydrophobic Langmuir-Blodgett Monolayers on Mica." *J. Colloid Interface Sci.* **1986**, *114*(1): 234.
32. Pashley, R. M.; McGuiggan, P. M.; Ninham, B. W.; Evans, D. F. "Attractive Forces between Uncharged Hydrophobic Surfaces - Direct Measurements in Aqueous Solution." *Science* **1985**, *229*(4718): 1088.
33. Attard, P. "Long-Range Attraction between Hydrophobic Surfaces." *J. Phys. Chem.* **1989**, *93*(17): 6441.
34. Kékicheff, P.; Spalla, O. "Long-Range Electrostatic Attraction between Similar, Charge-Neutral Walls." *Phys. Rev. Lett.* **1995**, *75*(9): 1851.
35. Podgornik, R. "Electrostatic Correlation Forces between Surfaces with Surface Specific Ionic Interactions." *J. Chem. Phys.* **1989**, *91*(9): 5840.
36. Miklavcic, S. J.; Chan, D. Y. C.; White, L. R.; Healy, T. W. "Double Layer Forces between Heterogeneous Charged Surfaces." *J. Phys. Chem.* **1994**, *98*(36): 9022.
37. Tsao, Y.-H.; Evans, D. F.; Wennerström, H. "Long-Range Attractive Force between Hydrophobic Surfaces Observed by Atomic Force Microscopy." *Science* **1993**, *262*(5133): 547.
38. Carambassis, A.; Jonker, L. C.; Attard, P.; Rutland, M. W. "Forces Measured between Hydrophobic Surfaces Due to a Submicroscopic Bridging Bubble." *Phys. Rev. Lett.* **1998**, *80*(24): 5357.
39. Yakubov, G. E.; Butt, H.-J.; Vinogradova, O. I. "Interaction Forces between Hydrophobic Surfaces. Attractive Jump as an Indication of Formation of "Stable" Submicrocavities." *J. Phys. Chem. B* **2000**, *104*(15): 3407.
40. Christenson, H. K.; Claesson, P. M. "Cavitation and the Interaction between Macroscopic Hydrophobic Surfaces." *Science* **1988**, *239*(4838): 390.

41. Parker, J. L.; Claesson, P. M.; Attard, P. "Bubbles, Cavities, and the Long-Ranged Attraction between Hydrophobic Surfaces." *J. Phys. Chem.* 1994, 98(34): 8468.
42. Craig, V. S. J.; Ninham, B. W.; Paskley, R. M. "Direct Measurement of Hydrophobic Forces: A Study of Dissolved Gas, Approach Rate, and Neutron Irradiation." *Langmuir* 1999, 15(4): 1562.
43. Yaminsky, V. V. "Cavitation, Polywater and Hydrophobic Attraction by Bridging by Flimsy Shells." *Colloids Surf. A* 1997, 130(Nov 30): 415.
44. Yoon, R.-H.; Flinn, D. H.; Rabinovich, Y. I. "Hydrophobic Interactions between Dissimilar Surfaces." *J. Colloid Interface Sci.* 1997, 185(2): 363.
45. Parker, J. L.; Claesson, P. M. "Direct Measurements of the Attraction Between Solvophobic Surfaces in Ethylene-Glycol and Mixtures With Water." *Langmuir* 1992, 8(3): 757.
46. Wood, J.; Sharma, R. "How Long Is the Long-Range Hydrophobic Attraction?" *Langmuir* 1995, 11(12): 4797.
47. Christenson, H. K.; Yaminsky, V. V. "Is the Long-Range Hydrophobic Attraction Related to the Mobility of Hydrophobic Surface Groups?" *Colloids Surf. A* 1997, 130: 67.
48. Kurihara, K.; Kato, S.; Kunitake, T. "Very Strong Long Range Attractive Forces between Stable Hydrophobic Monolayers of a Polymerized Ammonium Surfactant." *Chem. Lett.* 1990, 9: 1555.
49. Kurihara, K.; Kunitake, T. "Submicron-Range Attraction between Hydrophobic Surfaces of Monolayer-Modified Mica in Water." *J. Am. Chem. Soc.* 1992, 114(27): 10927.
50. Kokkoli, E.; Zukoski, C. F. "Interactions between Hydrophobic Self-Assembled Monolayers. Effect of Salt and the Chemical Potential of Water on Adhesion." *Langmuir* 1998, 14(5): 1189.
51. Christenson, H. K.; Claesson, P. M.; Parker, J. L. "Hydrophobic Attraction: A Reexamination of Electrolyte Effects." *J. Phys. Chem.* 1992, 96(16): 6725.
52. Christenson, H. K.; Fang, J.; Ninham, B. W.; Parker, J. L. "Effect of Divalent Electrolyte on the Hydrophobic Attraction." *J. Phys. Chem.* 1990, 94(21): 8004.
53. Christenson, H. K.; Claesson, P. M.; Berg, J.; Herder, P. C. "Forces between Fluorocarbon Surfactant Monolayers: Salt Effects on the Hydrophobic Interaction." *J. Phys. Chem.* 1989, 93(4): 1472.
54. Toikka, G.; Hayes, R. A.; Ralston, J. "Surface Forces between Spherical ZnS Particles in Aqueous Electrolyte." *Langmuir* 1996, 12(16): 3783.

55. Israelachvili, J. N.; Pashley, R. M. "The Hydrophobic Interaction Is Long-Range, Decaying Exponentially with Distance." *Nature* 1982, 300(5890): 341.
56. Israelachvili, J. N.; Pashley, R. M. "Measurement of the Hydrophobic Interaction between Two Hydrophobic Surfaces in Aqueous Electrolyte Solutions." *J. Colloid Interface Sci.* 1984, 98(2): 500.
57. Karaman, M. E.; Meagher, L.; Pashley, R. M. "Surface Chemistry of Emulsion Polymerization." *Langmuir* 1993, 9(5): 1220.
58. Meagher, L.; Craig, V. S. J. "Effect of Dissolved Gas and Salt on the Hydrophobic Force between Polypropylene Surfaces." *Langmuir* 1994, 10(8): 2736.
59. Tsao, Y.-H.; Evans, D. F.; Wennerström, H. "Long-Range Attraction between a Hydrophobic Surface and a Polar Surface Is Stronger Than That between Two Hydrophobic Surfaces." *Langmuir* 1993, 9(3): 779.
60. Parker, J. L.; Claesson, P. M. "Forces between Hydrophobic Silanated Glass Surfaces." *Langmuir* 1994, 10(3): 635.
61. Claesson, P. M.; Christenson, H. K. "Very Long Range Attractive Forces between Uncharged Hydrocarbon and Fluorocarbon Surfaces in Water." *J. Phys. Chem.* 1988, 92(6): 1650.
62. Claesson, P. M.; Herder, P. C.; Blom, C. E.; Ninham, B. W. "Interactions between a Positively Charged Hydrophobic Surface and a Negatively Charged Bare Mica Surface." *J. Colloid Interface Sci.* 1987, 118(1): 68.
63. Rabinovich, Y. I.; Derjaguin, B. V. "Interaction of Hydrophobic Filaments in Aqueous Electrolyte Solutions." *Colloids Surf.* 1988, 30(3-4): 243.
64. Parker, J. L.; Cho, D. L.; Claesson, P. M. "Plasma Modification of Mica: Forces between Fluorocarbon Surfaces in Water and a Nonpolar Liquid." *J. Phys. Chem.* 1989, 93(16): 6121.
65. Rabinovich, Y. I.; Yoon, R.-H. "Use of Atomic Force Microscope for the Measurements of Hydrophobic Forces between Silanated Silica Plate and Glass Sphere." *Langmuir* 1994, 10(6): 1903.
66. Rabinovich, Y. I.; Yoon, R.-H. "Use of Atomic Force Microscope for the Measurements of Hydrophobic Forces." *Colloids Surf. A* 1994, 93: 263.
67. Ljunggren, S.; Eriksson, J. C. "The Lifetime of a Colloid-Sized Gas Bubble in Water and the Cause of the Hydrophobic Attraction." *Colloids Surf. A* 1997, 130: 151.

68. Berg, S. R.; Paulsen, F. G.; Hassler, J. C.; Thompson, E. V. "Force-Distance Measurements of Bubble/Particle Interactions." 4th Research Forum on Recycling, 1997, Quebec, Qc, Canada.
69. Horn, R. G.; Bachmann, D. J.; Connor, J. N.; Miklavcic, S. J. "The Effect of Surface and Hydrodynamic Forces on the Shape of a Fluid Drop Approaching a Solid Surface." *J. Phys. Condens. Mat.* 1996, 8(47): 9483.
70. Miklavcic, S. J.; Horn, R. G.; Bachmann, D. J. "Colloidal Interaction between a Rigid Solid and a Fluid Drop." *J. Phys. Chem.* 1995, 99(44): 16357.
71. Bachmann, D. J.; Miklavcic, S. J. "Deformation of Fluid Interfaces Induced by Electrical Double-Layer Forces and Its Effect on Fluid-Solid Interactions." *Langmuir* 1996, 12(17): 4197.
72. Miklavcic, S. J. "Deformation of Fluid Interfaces under Double-Layer Forces Stabilizes Bubble Dispersions." *Phys. Rev. E* 1996, 54(6): 6551.
73. Joyce, S. A.; Houston, J. E. "A New Force Sensor Incorporating Force-Feedback Control for Interfacial Force Microscopy." *Rev. Sci. Instrum.* 1991, 62(3): 710.
74. Chan, D. Y. C.; Horn, R. G. "The Drainage of Thin Liquid Films between Solid Surfaces." *J. Chem. Phys.* 1985, 83(10): 5311.
75. Clark, H. M.; Burmeister, L. C. "The Influence of the Squeeze Film on Particle Impact Velocities in Erosion." *Int. J. Impact Engng.* 1992, 12(3): 415.
76. Rajagopalan, R. "Atomic Force and Optical Force Microscopy: Applications to Interfacial Microhydrodynamics." *Colloids Surf. A* 2000, 174(1-2): 253.
77. Ma, H.; Jimenez, J.; Rajagopalan, R. "Brownian Fluctuation Spectroscopy Using Atomic Force Microscopy." *Langmuir* 2000, 16(5): 2254.
78. Vinogradova, O. I. "Drainage of the Thin Liquid Film Confined between Hydrophobic Surfaces." *Langmuir* 1995, 11(4): 2213.
79. Vinogradova, O. I. "Hydrodynamic Interaction of Curved Bodies Allowing Slip on Their Surfaces." *Langmuir* 1996, 12(24): 5963.
80. Vinogradova, O. I. "Implications of Hydrophobic Slippage for the Dynamic Measurements of Hydrophobic Forces." *Langmuir* 1998, 14(10): 2827.
81. Vinogradova, O. I. "Slippage of Water over Hydrophobic Surfaces." *Int. J. Miner. Process.* 1999, 56(1-4): 31.

82. McCormack, D.; Carnie, S. L.; Chan, D. Y. C. "Calculations of Electric Double-Layer Force and Interaction Free Energy between Dissimilar Surfaces." *J. Colloid Interface Sci.* 1995, 169(1): 177.
83. Kar, G.; Chander, S.; Mika, T. S. "The Potential Energy of Interaction between Dissimilar Electrical Double Layers." *J. Colloid Interface Sci.* 1973, 44(2): 347.
84. Snyder, B. A.; Berg, J. C. "Oil-Assisted Agglomeration for Toner Deinking: Population Balance Model and Experiments." *AIChE J* 1997, 43(6): 1480.
85. Schulze, H. J. *Physico-chemical Elementary Processes in Flotation*; Elsevier: Amsterdam, 1984.
86. Luttrell, G. H.; Yoon, R.-H. "Production and Processing of Fine Particles." International Symposium on the Production and Processing of Fine Particles, 1988, Montreal, QC, Canada.
87. Yoon, R.-H.; Yordan, J. L. "Induction Time Measurements for the Quartz-Amine Flotation System." *J. Colloid Interface Sci.* 1991, 141(2): 374.
88. Fisher, L. R.; Mitchell, E. E.; Hewitt, D.; Ralston, J.; Wolfe, J. "The Drainage of a Thin Aqueous Film between a Solid Surface and an Approaching Gas Bubble." *Colloids Surf.* 1991, 52(1-2): 163.
89. Hewitt, D.; Fornasiero, D.; Ralston, J.; Fisher, F. R. "Aqueous Film Drainage at the Quartz/Water/Air Interface." *J. Chem. Soc. Faraday Trans.* 1993, 89(5): 817.
90. Paulsen, F. G.; Pan, R.; Bousfield, D. W.; Thompson, E. V. "The Dynamics of Bubble/Particle Attachment and the Application of Two Disjoining Film Rupture Models to Flotation." *J. Colloid Interface Sci.* 1996, 178(2): 400.
91. Snyder, B. A. *De-Inking Toner-Printed Paper by Selective Agglomeration*. Thesis, University of Washington, 1996.
92. Claesson, P. M.; Ederth, T.; Bergeron, V.; Rutland, M. W. "Techniques for Measuring Surface Forces." *Adv. Colloid Interface Sci.* 1996, 67: 119.
93. Fröberg, J. C.; Rojas, O. J.; M., C. P. "Surface Forces and Measuring Techniques." *Int. J. Miner. Process.* 1999, 56(1-4): 1.
94. Gauthier, S.; Aimé, J. P.; Bouhacina, T.; Attias, A. J.; Desbat, B. "Study of Grafted Silane Molecules on Silica Surface with an Atomic Force Microscope." *Langmuir* 1996, 12(21): 5126.

95. Laskowski, J.; Kitchener, J. A. "The Hydrophilic--Hydrophobic Transition on Silica." *J. Colloid Interface Sci.* 1969, 29(4): 670.
96. Flinn, D. H.; Guzonas, D. A.; Yoon, R.-H. "Characterization of Silica Surfaces Hydrophobized by Octadecyltrichlorosilane." *Colloids Surf. A* 1994, 87(3): 163.
97. Cleveland, J. P.; Manne, S.; Bocek, D.; Hansma, P. K. "A Nondestructive Method for Determining the Spring Constant for Scanning Force Microscopy." *Rev. Sci. Instrum.* 1993, 64(2): 403.
98. Johnson, K. L.; Kendall, K.; Roberts, A. D. "Surface Energy and the Contact of Elastic Solids." *Proc. R. Soc. Lond. A* 1971, 324: 301.
99. Vinogradova, O. I.; Horn, R. G. "Attractive Forces between Surfaces: What Can and Cannot Be Learned from a Jump-in Study with the Surface Forces Apparatus?" *Langmuir* 2001, 17(5): 1604.
100. Podgornik, R.; Parsegian, V. A. "An Electrostatic-Surface Stability Interpretation of the "Hydrophobic" Force Inferred to Occur between Mica Plates in Solutions of Soluble Surfactants." *Chem. Phys.* 1991, 154(3): 477.
101. Prausnitz, J. M.; Lichtenthaler, R. N.; de Azevedo, E. G. *Molecular Thermodynamics of Fluid-Phase Equilibria*. 2nd ed.; Prentice Hall: Englewood Cliffs, NJ, 1986.
102. Wiese, G. R.; Healy, T. W. "Effect of Particle Size on Colloid Stability." *Trans. Faraday Soc.* 1970, 66(2): 490.
103. Barnocky, G.; Davis, R. H. "The Lubrication Force between Spherical Drops, Bubbles, and Rigid Particles in a Viscous Fluid." *Int. J. Multiphase Flow* 1989, 15(4): 627.
104. Considine, R. F.; Drummond, C. J. "Long-Range Force of Attraction between Solvophobic Surfaces in Water and Organic Liquids Containing Dissolved Air." *Langmuir* 2000, 16(2): 631.
105. Bhatt, D.; Newman, J.; Radke, C. J. "Equilibrium Force Isotherms of a Deformable Bubble/Drop Interacting with a Solid Particle Across a Thin Liquid Film." *Langmuir* 2001, 17(1): 116.
106. Chan, D. Y. C.; Dagastine, R. R.; White, L. R. "Force between a Rigid Probe Particle and a Liquid Interface (I) The Repulsive Case." *J. Colloid Interface Sci.* 2001, 236(1): 141.
107. Hartland, S. "The Approach of a Rigid Sphere to a Deformable Liquid/Liquid Interface." *J. Colloid Interface Sci.* 1967, 26(4): 383.

108. Rosen, M. J. *Surfactants and Interfacial Phenomena*. 2nd ed.; John Wiley & Sons: New York, 1989.
109. Hutter, J. L.; Bechhoefer, J. "Calibration of Atomic Force Microscope Tips." *Rev. Sci. Instrum.* **1993**, *64*(7): 1868.
110. Li, Y. Q.; Tao, N. J.; Pan, J.; Garcia, A. A.; Lindsay, S. M. "Direct Measurement of Interaction Forces between Colloidal Particles Using the Scanning Force Microscope." *Langmuir* **1993**, *9*(3): 637.
111. Torii, A.; Sasaki, M.; Hane, K.; Okuma, S. "A Method for Determining the Spring Constant of Cantilevers for Atomic Force Microscopy." *Meas. Sci. Technol.* **1996**, *7*(2): 179.
112. Senden, T. J.; Ducker, W. A. "Experimental Determination of Spring Constants in Atomic Force Microscopy." *Langmuir* **1994**, *10*(4): 1003.
113. Butt, H.-J., et al. "Scan Speed Limit in Atomic Force Microscopy." *J. Microscopy* **1993**, *169*(1): 75.
114. Sader, J. E.; White, L. "Theoretical Analysis of the Static Deflection of Plates for Atomic Force Microscope Applications." *J. Appl. Phys.* **1993**, *74*(1): 1.
115. Gibson, C. T.; Watson, G. S.; Myhra, S. "Scanning Force Microscopy - Calibration Procedures for 'Best Practice'." *Scanning* **1997**, *19*(8): 564.
116. *Perry's Chemical Engineers' Handbook*; 6th ed.; Green, D. W., Ed.; McGraw-Hill Inc.: New York, 1984.

## APPENDIX A:

## FORCE CONSTANT CALIBRATION OF AFM CANTILEVERS

Determination of the normal spring constant, or stiffness, of a cantilever used for measuring forces in atomic force microscopy (AFM) is accomplished by a variety of methods. Most manufacturers of AFM cantilevers give only a rough estimate of the force constant ( $\pm 100\%$ ) making it necessary to calibrate them for quantitative force profiling experiments. Dynamic cantilever response is the most prominent, where the cantilever vibrations are related directly to its stiffness. The method implemented in the present studies relate added mass,  $m_{add}$ , to  $\nu$ , the primary free resonance frequency:<sup>97</sup>

$$m_{add} = \frac{k}{(2\pi\nu)^2} - m_{eff}. \quad (\text{A.1})$$

The slope of a plot added mass against  $(2\pi\nu)^2$  is the normal spring constant  $k$ . The addition of well-characterized spheres, i.e. know density and volume, to the very tip of the cantilever lowers the resonance frequency. In this way, the effective mass of the cantilever, which is not easily quantifiable, may be eliminated from the procedure. For a beam of rectangular cross-section,  $m_{eff} \approx 0.24m$ ; yet the more common cantilever geometry is triangular.

Two measurements alone—one unloaded, one with added mass—are sufficient to find the spring constant with some certainty. Since the micron-size particles are neither available in an exactly known dimension nor quickly measured, it is desirable to conduct multiple frequencies measurements for a number of particles and total added masses. The example presented here attached NIST standard glass beads ( $8.2 \pm 0.8 \mu\text{m}$  diameter) which remained on the cantilever through capillary action alone, allowing them to be removed without permanent cantilever alteration. Figure A.1 plots the data generally

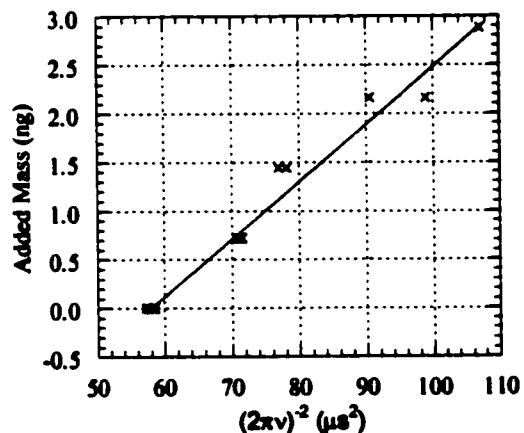


Figure A.1: Linear fit of added tip mass to an AFM cantilever as a function of the scaled resonance frequency.

represented by Eq. A.1 taken for a Microlever™ of nominal stiffness 0.05 N/m from Park Scientific Instruments. A linear fit of all points up to four added glass spheres ( $v_0-v_4$ ) gives  $0.059\pm 0.004$  N/m, but a more precise fit of  $v_0$  and  $v_1$  only gives  $0.054\pm 0.002$  N/m. Nevertheless, which is the better accuracy is indeterminate from this type of examination alone, though it is visually obvious that more scatter occurs as multiple spheres are added. This is primarily due to the fact that they cannot all hang from exactly the same location on the tip as is required by the assuming of the model. Further, considering the deviations of the AFM detector and scanner over multiple compliance scans shows an equivalent error of  $\pm 0.002$  N/m, assuming linear deflections. Thus, the average reported stiffness for this particular cantilever is  $0.056\pm 0.002$  N/m.

Another dynamic way to measure the spring constant is through a power spectrum analysis of the thermal vibrations of a cantilever. The thermal energy unit  $k_B T$  is proportional to the mean-square displacement of the cantilever by its stiffness:<sup>109</sup>

$$k_B T = k \langle d^2 \rangle. \quad (\text{A.2})$$

This can often be more difficult than it appears, especially for the triangular cantilevers that do not have a well-characterized power spectrum.

Static methods can also be implemented to determine the force constant, such as through calibration against another beam of known stiffness<sup>110,111</sup> or by force balance with gravity when a sufficiently large particle may be attached for accurate static deflection to be detected<sup>112</sup> or by displacing a pendulum.<sup>113</sup> It is possible, however time-consuming, to calculate the stiffness from first principles, even for a cantilever of arbitrary geometry. Evaluation of the expressions are not readily accomplished even for a triangular cantilever;<sup>114</sup> but this has been found to be well-approximated by two parallel rectangular beams of the same length, width, and thickness.<sup>112</sup> These and other methods for determining the spring constant are further discussed and referenced in a recent publication.<sup>115</sup>

## APPENDIX B:

### EXACT SOLUTIONS TO THE POISSON-BOLTZMANN EQUATION FOR CONSTANT POTENTIAL SURFACES

#### B.1 Background

The following program written for MATLAB 5.0 determines the DLVO interaction energy ( $V$ ) of two spheres (radii  $a_1$  and  $a_2$ ) using the nonlinear Poisson-Boltzmann equation solution for constant surface potentials ( $Y_0$  and  $Y_d$ ) between parallel plates with the Derjaguin approximation. An iterative procedure is implemented as outlined by McCormack *et al.*<sup>82</sup> Their notation has been used wherever possible. Extensive commenting within the program code has been left to provide a guide for understanding the calculation.

#### B.2 Overview of Program Subroutines

The main program (Section B.2.1) declares the constant and variable parameters in accordance with McCormack *et al.*,<sup>82</sup> calling functions, or m-files, for equations listed in Table 1 of their paper (Section B.2.2) and for common elliptic functions implemented in the solutions (Section B.2.3). Data for nondimensionalized surface potentials ( $Y$ ), surface charge densities ( $S$ ), interaction energies ( $V$ ), and separation at closest approach ( $d$ ) are saved to arrays, plotted to the screen, and can be saved to a data file. The backbone of the routine is sufficient for any electrostatic boundary conditions described by McCromack *et al.*, given appropriate functions and redefined surface charges and/or potentials ( $Y_0$ ,  $Y_d$ ,  $S_0$ ,  $S_d$ ,  $Y_{0ini}$ ,  $Y_{dini}$ ,  $S_{0ini}$ ; and  $S_{dini}$ ).

##### ***B.2.1 Main Program Code for Poisson-Boltzmann Equation***

```
clear
global Yo Yd So Sd d kappa Ymin PhiO PhiD k L

%%%%%% When constant surface potentials Yo, Yd are used.
m=1; % counting index for Ydfunc3(b) to estimate b
i=1; % index for 1D arrays containing values for d, Y, S, V, W, etc.
j=0; % index for array rem(j,5)
kb=1.380662e-23; % Boltzmann constant, [J/K]
```

```

T=295; % T = absolute temperature, [K]
a1=1; % radius of body 1, e.g. plate, [m]
a2=4.1e-6; % radius of body 2, e.g. sphere, [m]
A=8.3e-21; % Hamaker constant, [J]
conc=0.001; % ion concentration, [M]
no=2*conc*1000*6.022e23; % no = ion concentration, [molecules/cu.m.]
kappa=(conc^0.5)/0.3043*1e9; % kappa = Debye parameter, [1/m]

%% Surface 1 (x=0) always positive in Yo or So, surface 2 (x=d) always lower pot'l or charge density
Yo=1.157; % isolated surface potential at x = 0 for surface 1, [dimensionless]
Yd=0.5; % isolated surface potential at x = d for surface 2, [dimensionless]
So=2*sinh(Yo/2); % isolated surface charge density for surface 1, [dimensionless]
Sd=2*sinh(Yd/2); % isolated surface charge density for surface 2, [dimensionless]
Yoini=Yo;
Ydini=Yd;
Soini=So;
Sdini=Sd;

% C = Poisson-Boltzmann eq. integration factor, b >=1, variable from MCC Table 1 eqs. (IIIc)
if Yo/Yd <= 0
    C = -1.9999999; % Poisson-Boltzmann eqn integration factor.
else
    C=-2.00001;
end

b = 1.02; % b >=1, variable from McCormack et al (MCC) Table 1 eqs. (IIIc).
d = 10/kappa; % d = separation, [m]. Arbitrary factors 10 & 500 below.
Vnew=0; % At very large separation, the min pot'l is at d/2.
DeltaX=d/500; % Step-size for separation.

% V = sphere-plate interaction energies, DeltaX = separation step size
%% 1st loop starts here, continues while separation, d > 0.4 nm, calculates the energy V.
while d > 4e-10

%% 5th loop starts here, repeats 3 times, determines the value of C for given d.
for p=1:3

% MCC Table 1 (IVa) when C = -2, repulsive regime switch
if Yd > 0
Xswitch=(log(tanh(Yo/4)/tanh(Yd/4)))/kappa;
end

% MCC Table 1 (Va) when C = 2, attractive regime switch
Xswitch2=2*(atan(exp(Yo/2))-atan(exp(Yd/2)))/kappa;

%% For repulsive case MCC Table 1 Eqns (I). The min pot'l is never greater than the lower surf pot'l
if C <= -2
Ymin=acosh(-C/2);
if Ymin > Yd
Ymin=Yd;
end
end
end

```

```

if d >= Xswitch & Yd > 0 & C <= -2
    C=fsolve('Ydfunc1',C,[0 1e-8 1e-8]);
end

%%%%%%%%%% Next two if loops calculate near the critical separation C=-2
if C < -1.99999;
    while C > -2
        Ymin=acosh(-C/2);
        if Ymin > Yd
            Ymin=Yd;
        end
        d=Xswitch-DeltaX/2;
        C=fsolve('Ydfunc2',C,[0 1e-8 1e-8]);
        Xswitch=(log(tanh(Yo/4)/tanh(Yd/4)))/kappa;
    end
end

if d <= Xswitch & Yd > 0 & C <= -2
    C=-1.9999
    C=fsolve('Ydfunc2',C,[0 1e-8 1e-8]);
end

%%%%%%%%%% Attractive regime, MCC Table 1 (II)
% Fo = evaluated incomplete elliptic integral of 1st kind. L = k^2
% K = complete elliptic integral of 1st kind. E = complete elliptic integral of 2nd kind

if (C < 2 & C > -2)
    C=fsolve('Ydfunc2',C,[0 1e-8 1e-8]);
    % Fo=quad8('ellip1st',0,PhiO,[1e-8]);
    % [K,E]=ellipke(L);
end

%%%%%%%%%% Switch regimes
if C >= 1.99 & d >= Xswitch2
    C=(b^2)+(b^(-2));
    d=Xswitch2-DeltaX;
end

%%%%%%%%%% I'm not sure why this would only be for Yd > 0
if C < 2.01 & C > 2 & d > Xswitch2 & Yd > 0
    C=2.015;
    d=Xswitch2-DeltaX/4;
end

%%%%%%%%%% Attractive regime, MCC Table 1 (III)
if C >= 2
    b=fsolve('Ydfunc3',b,[0 1e-8 1e-8]);
    while b < 1
        b=1+0.005*m;
        b=fsolve('Ydfunc3',b,[0 1e-8]);
        m=m+1;
    end
end

```

```

        C=(b^2)+(b^(-2));
end

Fo=quad8('ellip1st',0,PhiO,[1e-8]);
[K,E]=ellipke(L);
So=(2*cosh(Yo)+C)^(1/2);
Sd=(2*cosh(Yd)+C)^(1/2);

end
%%%%%%%%% 5th loop ends here, C is determined

if C <= -2
Ymin=acosh(-C/2);
    if Ymin > Yd
        Ymin=Yd;
    end
end

%%%%%%%%% Vpp = parallel plate double-layer interaction energy
%%%%%%%%% Repulsive regime, MCC Table 2 Eqs (I)
% MCC Table 1 Eq 1a always applicable for X=Xmin, C<=-2; when Y=Ymin, Phi=pi/2 then F(k,Phi)=K
if C <= -2

    Fo=quad8('ellip1st',0,PhiO,[1e-8]);
    [K,E]=ellipke(L); % Complete elliptic integrals of 1st and 2nd Kinds
    Eo=quad8('ellip2nd',0,PhiO,[1e-8]);
    Ed=quad8('ellip2nd',0,PhiD,[1e-8]);
    Xmin=2*sqrt(k)*(K-Fo)/kappa;

    if Xmin >= d
        Vpp=-2*no*kb*T/kappa*(0.5*kappa*d*(3*exp(Ymin)-2*exp(-Ymin))+2*(2*cosh(Yo)-
        2*cosh(Ymin))^(1/2)-(2*(2*cosh(Yd)-2*cosh(Ymin))^(1/2))+4*exp(Ymin/2)*(Eo-Ed))-
        (4*(cosh(Yo/2)+cosh(Yd/2)-2)));
    end

    if Xmin < d
        ans=C
        ans=d
        ans=Xmin
        Vpp=-2*no*kb*T/kappa*(0.5*kappa*d*(3*exp(Ymin)-2*exp(-Ymin))+2*(2*cosh(Yo)-
        2*cosh(Ymin))^(1/2)+2*(2*cosh(Yd)-2*cosh(Ymin))^(1/2)+4*exp(Ymin/2)*(Eo+Ed-2*E)-
        4*(cosh(Yo/2)+cosh(Yd/2)-2)));
        ans=V
    end

end

%%%%%%%%% Attractive regime, MCC Table 2 Eqs (II)
if C >= -2 & C <= 2
    Eo=quad8('ellip2nd',0,PhiO,[1e-7]);
    Ed=quad8('ellip2nd',0,PhiD,[1e-7]);
    [K,E]=ellipke(L); % Complete elliptic integrals of 1st and 2nd Kinds

```

```

    if Yd > 0
        Vpp=2*no*kb*T/kappa*(-0.5*kappa*d*(C+2)+((8*(cosh(Yd)-
1)*(cosh(Yd)+(C/2)))/(cosh(Yd)+1))^(1/2)-((8*(cosh(Yo)-
1)*(cosh(Yo)+(C/2)))/(cosh(Yo)+1))^(1/2)+4*(Eo-Ed)+4*(cosh(Yo/2)+cosh(Yd/2)-2));
    end

    if Yd < 0
        Vpp=2*no*kb*T/kappa*(-0.5*kappa*d*(C+2)-((8*(cosh(Yd)-
1)*(cosh(Yd)+(C/2)))/(cosh(Yd)+1))^(1/2)-((8*(cosh(Yo)-
1)*(cosh(Yo)+(C/2)))/(cosh(Yo)+1))^(1/2)+8*E-4*(Eo+Ed)+4*(cosh(Yo/2)+cosh(Yd/2)-2));
    end

end

% Attractive regime, MCC Table 2 Eqn (III)
if C >= 2

    PhiO=atan(b*exp(-Yo/2));
    PhiD=atan(b*exp(-Yd/2));
    Eo=quad8('ellip2nd',0,PhiO,[1e-7]);
    Ed=quad8('ellip2nd',0,PhiD,[1e-7]);
    Vpp=2*no*kb*T/kappa*(0.5*kappa*d*(2-C)-
2*((2*cosh(Yd)+C)^(1/2))+2*((2*cosh(Yo)+C)^(1/2))-4*exp(Yo/2)*(((b^(
2))+exp(Yo))/(b^2+exp(Yo)))^(1/2)+4*exp(Yd/2)*(((b^(
2))+exp(Yd))/(b^2+exp(Yd)))^(1/2)+4*b*(Ed-Eo)+4*(cosh(Yo/2)+cosh(Yd/2)-2));
end

V=Vpp

%Energy for mixed const surf pot'l and charge density bodies.
%V=Vpp+2*no*kb*T/kappa*(Sd*(Yd-Ydini)-4*(cosh(Yd/2)-cosh(Ydini/2)));

% Sums energy incrementally with each complete cycle instead of integrating each time from infinity to d.

Vold=Vnew;
Vr=2*a1*a2*pi*V*DeltaX/(a1+a2);      % Vr = incremental step in double-layer energy.
Vnew=Vold+Vr;
%van der Waals energy with Born repulsion term
Va=-(A/6)*(a1*a2)/(a1+a2)*(1/d-((1.6e-10)^6)/(7*d^7))
Vt=Va+Vnew;

% Solutions assign to the i position in given arrays
X3(i,1)=d*10e9; % separation, [nm]
C3(i,1)=C;      % integration constant
So3(i,1)=So;   % surf charge density of body 1 at x=0
Sd3(i,1)=Sd;   % surf charge density of body 2 at x=d
Yo3(i,1)=Yo;   % surf pot'l of body 1 at x=0
Yd3(i,1)=Yd;   % surf pot'l of body 2 at x=d
Va3(i,1)=Va;   % attractive van der Waals energy
Vnew3(i,1)=Vnew; % double-layer energy

```

```

Vt3(i,1)=Vt;    % total interaction energy, Va+Vnew
V3(i,1)=V;

% Saves arrays every 5th loop except the 1st cycle of 6 loops, every pass when d < 5 nm.
if rem(j,5) == 0 | d < 5e-9
save conc X3 C3 So3 Sd3 Va3 Vnew3 Vt3 V3
ans=C
ans=d
i=i+1;
end
j=j+1; %Starts with j = 0
Cold=C;

% Optimizes discrete step size, "DeltaX", according to C error
% Original DeltaX is 10/(500*kappa). Factors for DeltaX calculation are somewhat arbitrary

if abs(Cold-C) > 0.0001
DeltaX=DeltaX/5;
elseif abs(Cold-C) < 0.000005
DeltaX=DeltaX*2;
else
DeltaX=DeltaX*1.25;
end

% Steps 1 Angstrom while in repulsive regime
if C < -2
DeltaX=1e-10;
end

d=d-DeltaX;

end
%%%%%%%%%%%%%%%%%%%%%%%%%%%%%%%%%%%%%%%%%%%%%%%%%%%%%%%%%%%%%%%%%%%%%%%% 1st loop ends, the "while" statement, here

%Simply plots results
subplot(2,2,1)
plot(X3,Va3,'o',X3,Vnew3,'+',X3,Vt3,'-'),xlabel('Separation (nm)'),ylabel('Interaction
Potential'),legend('van der Waals','electrostatic','total')
subplot(2,2,2)
plot(X3,So3,'*'),xlabel('Separation (nm)'),ylabel('Surface Charge Density (So)')
subplot(2,2,3)
plot(X3,Sd3,'#'),xlabel('Separation (nm)'),ylabel('Surface Charge Density (Sd)')
subplot(2,2,4)
plot(X3,V3,'+'),xlabel('Plate Separation (nm)'),ylabel('Interaction Potential (Velec)'),legend('parallel flat
plates')

```

### ***B.2.2 Function Program Codes for Solving Surface Potential***

```

%%%%%%%%%%%%%%%%%%%%%%%%%%%%%%%%%%%%%%%%%%%%%%%%%%%%%%%%%%%%%%%%%%%%%%%% The function codes used by *nPB.m programs are listed below.
function f=Ydfuncl(C);
% Saved as Ydfuncl.m based on MCC Table 1 Eq (I) (c-d), repulsive interactions.

```

**% Function valid for the  $C \leq -2$  in nonlinear Poisson-Boltzmann solution.**

```

global Yo Yd So Sd d kappa Ymin PhiO PhiD k L
Ymin=real(acosh(-C/2));
    if Ymin >= Yd
        Ymin=Yd;
    end
k=exp(-Ymin);
PhiD=asin(exp((Ymin-Yd)/2));
PhiO=asin(exp((Ymin-Yo)/2));
z=kappa*d/(2*k.^(1/2));
L=k.^2;
[sn,cn,dn]=ellipj(z,L); % Jacobi elliptic functions
f(1)=-Yd+Ymin-2*log((sin(PhiO)*cn*dn+cos(PhiO)*(1-k.^2*(sin(PhiO)).^2).^(1/2)*sn)/(1-
k.^2*(sin(PhiO)).^2*(sn).^2));

```

```

%-----
function g=Ydfunc2(C);
% Saved as Ydfunc2.m based on MCC Table 1 Eq (II) (c-d), attractive interactions.
% Function valid for  $-2 \leq C \leq 2$  in nonlinear Poisson-Boltzmann solution.
% Most commented lines are needed for mixed const pot'l/charge

```

```

global Yo Yd So Sd d kappa PhiO PhiD k L
if Yd > 0
    k=((2-C)/4).^(1/2);
    PhiD=asin((cosh(Yd/2)).^(-1));
    PhiO=asin((cosh(Yo/2)).^(-1));
    z=d*kappa;
    L=(k.^2);
    [sn,cn,dn]=ellipj(z,L); % Jacobi elliptic functions
    g(1)=-Yd+2*acosh((1-(k.^2)*((sin(PhiO)).^2)*(sn).^2)/((sin(PhiO)*cn*dn)+(cos(PhiO)*((1-
(k.^2)*(sin(PhiO)).^2).^(1/2))*sn)));
end

```

```

If Yd < 0
k=((2-C)/4).^(1/2);
PhiD=asin((cosh(Yd/2)).^(-1));
PhiO=asin((cosh(Yo/2)).^(-1));
z=d*kappa;
L=(k.^2);
[sn,cn,dn]=ellipj(z,L); % Jacobi elliptic functions
g(1)=-Yd-(2*acosh((1-(k.^2)*((sin(PhiO)).^2)*(sn).^2)/((sin(PhiO)*cn*dn)+(cos(PhiO)*((1-
(k.^2)*(sin(PhiO)).^2).^(1/2))*sn)));
end

```

```

%-----
function h=Ydfunc3(b);
% Saved as Ydfunc3.m based on MCC Table 1 Eq (III) (b-c), attractive interactions
% Function valid for  $C \geq 2$  in nonlinear Poisson-Boltzmann solution.

```

```

global Yo Yd So Sd d kappa PhiO PhiD k L
k=(1-(b.^(-4))).^(1/2);

```

```

PhiD=atan(b*exp(Yd/2));
PhiO=atan(b*exp(Yo/2));
z=b*d*kappa/2;
L=k.^2;
[sn,cn,dn]=ellipj(z,L); % Jacobi elliptic functions
h(1)=-Yd+2*log((1/b)*tan(asin((sin(PhiO)*cn*dn-cos(PhiO)*(1-k.^2*(sin(PhiO)).^2).^(1/2)*sn)/(1-
k.^2*(sin(PhiO)).^2*(sn).^2)))));
v=(sqrt(1-(k*sin(Phi)).^2)).^(-1);

```

### ***B.2.3 Elliptical Functions***

```

function v=ellip1st(Phi);
% Function inside elliptic integrals of the 1st kind. Saved as m-file "ellips1st.m"
global k
v=(sqrt(1-(k*sin(Phi)).^2)).^(-1);
%-----
function o=ellip2nd(Phi);
% Function inside elliptic integrals of the 2nd kind. Saved as m-file "ellips2nd.m"
global k
o=sqrt(1-(k*sin(Phi)).^2);

```

## APPENDIX C:

### DETERMINING DROP PROFILE DEFORMATION DUE TO AN IMPINGING SPHERE

#### C.1 The 4<sup>th</sup> Order Runge-Kutta Procedure for the Young-Laplace Equation

A numerical solution is found for the profile of a liquid drop being deformed by an axially symmetric pressure distribution applied via a much smaller sphere using equations from Chapter 5. In general, the pressure difference,  $\Delta P$ , may include components other than the internal drop pressure,  $P_o$ , and the disjoining pressure,  $\Pi(D)$ , the most common being gravity which is insignificant for the microscale. The disjoining pressure is a function of interfacial separation,  $D$ , strictly speaking, but is written in terms of the function of the drop profile,  $z(r)$ , height measured from the apex down as a function of radius. Thus, the problem may be recast in a simplified 2-dimensional rectilinear coordinate system with the  $z$ -axis as the axis of symmetry for the drop and  $r$  as the perpendicular distance from it.

Following the standard 4<sup>th</sup> order Runge-Kutta procedure,<sup>116</sup> the Young-Laplace Equation (Eq. 5.1) is rearranged to isolate the second-order derivative:

$$\frac{d^2 z}{dr^2} = \frac{\Delta P(z)}{\sigma} \left[ 1 + \left( \frac{dz}{dr} \right)^2 \right]^{\frac{3}{2}} - \frac{1}{r} \frac{dz}{dr} \left[ 1 + \left( \frac{dz}{dr} \right)^2 \right]. \quad (\text{C.1})$$

Equation C.1 is then reduced to a first-order differential equation with the declaration of a new variable,  $y$ :

$$\frac{dz}{dr} = y, \quad (\text{C.2})$$

$$\frac{dy}{dr} = \frac{d^2 z}{dr^2} = g(r, z, y). \quad (\text{C.3})$$

The initial conditions will be defined at the apex of the drop,  $r = 0$ ,  $z = 0$ ,  $y = 0$ :

$$\frac{dy}{dr} = \frac{\Delta P}{2\sigma}. \quad (\text{C.4})$$

The set of equations used in each iteration,  $i$ , are then defined with any step size,  $h$ , of the independent variable,  $r$ :

$$\begin{aligned} k_0 &= hy_i & l_0 &= hg_i(r_i, z_i, y_i) \\ k_1 &= h\left(y_i + \frac{l_0}{2}\right) & l_1 &= hg_i\left(r_i + \frac{h}{2}, z_i + \frac{k_0}{2}, y_i + \frac{l_0}{2}\right) \\ k_2 &= h\left(y_i + \frac{l_1}{2}\right) & l_2 &= hg_i\left(r_i + \frac{h}{2}, z_i + \frac{k_1}{2}, y_i + \frac{l_1}{2}\right) \\ k_3 &= h(y_i + l_2) & l_3 &= hg_i(r_i + h, z_i + k_2, y_i + l_2) \end{aligned} \quad (\text{C.5})$$

Starting with the initial conditions,  $i = 0$ , the calculations within a given iteration are accomplished consecutively,  $k_0, l_0, k_1, \dots, l_3$ . The magnitude of  $h$  may be varied for the best conversion between iterations. The new values for the drop profile are then as follows:

$$r_{i+1} = r_i + h, \quad (\text{C.6})$$

$$z_{i+1} = z_i + (k_0 + 2k_1 + 2k_2 + k_3)/6, \quad (\text{C.7})$$

$$y_{i+1} = y_i + (l_0 + 2l_1 + 2l_2 + l_3)/6. \quad (\text{C.8})$$

The routine can be easily setup in a spreadsheet, but the number of iterations quickly becomes too large to handle efficiently in this forum for an AFM model. However, this might be quite sufficient for cases that do not require the same level of accuracy, like a sessile drop. Instead, a program should be written with this routine that can adjust the step size as needed and save the  $r, z$  data to a file of any size. The program code written for MATLAB to accomplish this is given in Section C.2 with appropriate comments.

The above procedure suffers a singularity when  $r$  approaches the undisturbed drop radius,  $R_0$ ; that is, the slope rising to infinity in this coordinate system. This is only a real difficulty if the exact total change in drop height is required, as in the case of determining linear drop deformation for comparison and interpretation of AFM force-distance data. Many

situations will allow a good estimate of the drop profile as  $r$  approaches  $R_d$  simply by assuming constant curvature for this segment until the slope again becomes defined below the equator. A simple parameterization of the Young-Laplace Equation may also be implemented which is only valid as long as the interfacial curvature does not invert. Consequently, this cannot be used for the entire drop profile calculation for sphere-drop configurations since the curvature does invert for some pressures within the impinging zone as seen in Chapter 5.

To remove the slope singularity, the parameterization  $dz/dr = \tan\phi$  is substituted into Eq. 5.1 to give two first-order ordinary differential equations:

$$\frac{dr}{d\phi} = \frac{-r\sigma \cos\phi}{-r\Delta P + \sigma \sin\phi} = f_1(\phi, r, z), \quad (\text{C.9})$$

$$\frac{dz}{d\phi} = \frac{-r\sigma \sin\phi}{-r\Delta P + \sigma \sin\phi} = f_2(\phi, r, z). \quad (\text{C.10})$$

These are similar to those presented by Miklavcic<sup>72</sup> with an inverted  $z$ -coordinate and the same boundary conditions at the apex,  $z(\phi) = 0$  for  $\phi = 0$ :

$$\frac{dr}{d\phi} = \frac{2\sigma}{\Delta P}, \quad (\text{C.11})$$

$$\frac{dz}{d\phi} = 0. \quad (\text{C.12})$$

This set of equations (Eqs. C.9-C.12) is well-behaved for the entire range of  $\phi$  from 0 to  $\pi$  for a uniform pressure field or for the drop-plate geometry to describe a complete free body. It is not adequate when the sign of  $dz/d\phi$  changes, e.g. interfacial curvature inverting from convex to concave.

The set of equations (Eqs. C.13-C.16) used in each iteration,  $i$ , are again defined with any step size,  $h$ , of the independent variable,  $\phi$ , where the functions to be evaluated,  $f_1$  and  $f_2$ , refer to Eqs. C.9 and C.10, respectively:

$$\begin{aligned}
k_0 &= hf_1(\phi_i, r_i, z_i) & l_0 &= hf_2(\phi_i, r_i, z_i) \\
k_1 &= hf_1\left(\phi_i + \frac{h}{2}, r_i + \frac{k_0}{2}, z_i + \frac{l_0}{2}\right) & l_1 &= hf_2\left(\phi_i + \frac{h}{2}, r_i + \frac{k_0}{2}, z_i + \frac{l_0}{2}\right) \\
k_2 &= hf_1\left(\phi_i + \frac{h}{2}, r_i + \frac{k_1}{2}, z_i + \frac{l_1}{2}\right) & l_2 &= hf_2\left(\phi_i + \frac{h}{2}, r_i + \frac{k_1}{2}, z_i + \frac{l_1}{2}\right) \\
k_3 &= hf_1(\phi_i + h, r_i + k_2, z_i + l_2) & l_3 &= hf_2(\phi_i + h, r_i + k_2, z_i + l_2)
\end{aligned} \tag{C.13}$$

$$\phi_{i+1} = \phi_i + h, \tag{C.14}$$

$$r_{i+1} = r_i + (k_0 + 2k_1 + 2k_2 + k_3)/6, \tag{C.15}$$

$$z_{i+1} = z_i + (l_0 + 2l_1 + 2l_2 + l_3)/6. \tag{C.16}$$

## C.2 The MATLAB Program Code for Parameterized Young-Laplace Equation

The following code is executed in MATLAB 5 and saved under the appropriate m-files for solving the Young-Laplace Equation as parameterized for  $dz/dr = \tan\phi$  as above (Eqs. C.9-C.16). The main program calls functions  $k$ ,  $l$ , and  $\Delta P$  to calculate the Runge-Kutta parameters (Eq. C.13) and the pressure drop across the interface (Eq. 5.1). Since the code only supports standard characters, the usual symbols—Greek letters, subscripts, and others—have been renamed to avoid confusion and appropriate comments within the program are designated by % to define each. For convenience, these changes are compiled below:

$\epsilon_0$	=	epso	$P_0$	=	Po
$\epsilon$	=	eps	$\phi$	=	phi
$R_d$	=	a1	$dz/d\phi$	=	dz
$R_s$	=	a2	$dr/d\phi$	=	dr
$r_0$	=	ro	$D_0$	=	Do
$\psi_1$	=	Y1	$\Pi$	=	CapPi
$\psi_2$	=	Y2	$\Delta P$	=	DeltaP
$\kappa$	=	kappa	$r_i$	=	roid
$C_1$	=	C1	$z_i$	=	zoid
$\lambda_1$	=	lambda1	$k_1, k_2, \text{etc.}$	=	k1, k2, etc.
$\sigma$	=	sigma	$l_1, l_2, \text{etc.}$	=	l1, l2, etc.

### C.2.1 Main Program Code for Calculating Drop Profile

```

clear
global a2 Do A ro eps eps0 kappa Y1 Y2 C1 lambda l Po sigma CapPi h
i=1;          % index for 1D arrays of r1, z1, P1.
j=1;          % index for remainder function rem(j,n)
n=5;          % index for remainder function
eps0=8.8542e-12; % permittivity of free space, [sqC/(N-sqm)]
eps=78.54;    % dielectric constant, [unitless]
a1=200; % radius of body 1—droplet, [um]
a2=8.877;    % radius of body 2—sphere, [um]
A=5e-21;    % Hamaker constant, [J]
ro=0.16;    % universal atomic spacing, [nm]
Y1=-18;     % droplet isolated surface potential, [mV]
Y2=-18;     % sphere isolated surface potential, [mV]
conc=0.0001; % ion concentration, [M]
kappa=(conc^0.5)/0.3043; % Debye parameter, [1/nm]
C1=0;       % hydrophobic strength, [mN/m]
lambda l=3; % hydrophobic decay length, [nm]
sigma=52;   % surface tension, [mN/m]
Po=2*sigma*1000/a1; % Laplace pressure, [Pa]
phi=0;      % angular independent parameter, [radians]
r=0;        % initial drop profile radius from z-axis, [nm]
z=0;        % initial drop profile height/depth, [nm]
dz=0;       % BC1, slope at apex, r=0, z=0, [nm]
Do = 200;   % Do = closest approach separation, r=0 [nm]
dr=1e6*2*sigma/DeltaP(r,z); % initial condition, derivative of r w.r.t. phi, [nm]
CapPi=Po-DeltaP(r,z); %  $\Pi(z)$ , i.e. surface pressure, [Pa]
h=0.00001; % h = initial step size for phi, [radians]

%%%%%Iteration loop starts here, calculates drop profile r,z and pressure
while phi < pi+h % continues until phi > pi = 3.14159
%%%%%Step size is varied to optimize solution time and accuracy
if r < 1000 & r > 10
    h = 0.0001; % for 10 nm < r < 1000 nm
end
if r > 1000
    h = 0.001; % for r > 1000 nm
end
if r > 10000
    h = 0.005; % for r > 10000 nm
end
if r > a1*999
    h = 0.001; % for r approaching a1, the drop radius
end
if r > a1*999.9
    h = 0.0001; % further, for r approaching a1
end
if rem(j,n) == 0 | r < 1000 % executes every nth value of j

```

```

r1(i,1)=r;      % assigns radius value to ith array position, [nm]
z1(i,1)=z;     % assigns height value ", [nm]
P1(i,1)=CapPi; % assigns surface pressure ", [Pa]
i=i+1;
end
rold=r;        %holds value of r from previous iteration
zold=z;        %holds value of z from previous iteration
phipass=phi;
rpass=r;
zpass=z;
ko=k(phipass,rpass,zpass);% first Runge-Kutta estimator for "r".
lo=l(phipass,rpass,zpass); % first Runge-Kutta estimator for "z".
if j == 1
    ko=h*dr;    % initial conditions for apex
    lo=0;      % " " "
end
phipass=phi+h/2;
rpass=r+ko/2;
zpass=z+lo/2;
k1=k(phipass,rpass,zpass); % second Runge-Kutta estimator for "r", etc.
l1=l(phipass,rpass,zpass);
phipass=phi+h/2;
rpass=r+k1/2;
zpass=z+l1/2;
k2=k(phipass,rpass,zpass);
l2=l(phipass,rpass,zpass);
phipass=phi+h;
rpass=r+k2;
zpass=z+l2;
k3=k(phipass,rpass,zpass);
l3=l(phipass,rpass,zpass);
r=rold+(ko+2*k1+2*k2+k3)/6; % next value of radius
z=zold+(lo+2*l1+2*l2+l3)/6; % next value of height
phi=phipass; % next value of angle, phi + h
CapPi=Po-DeltaP(r,z); % surface pressure at location r,z.
j=j+1;
end
%%%%%%%%%% Iteration loop ends here and last values for r, z, and Π are stored.

r1(i,1)=r;      % profile radius, [nm]
z1(i,1)=z;     % profile height, [nm]
P1(i,1)=CapPi; % surface pressure, Π(z), [Pa]
save data1.dat r1 z1 P1 -ASCII; % Saves matrices to 8-bit ASCII file

%%%%%%%%%% Simply plots results to the screen
subplot(2,2,1)
plot(r1,z1,'+'),xlabel('Drop Radius (nm)'),ylabel('Drop Height (nm)'),legend('Drop Profile')
subplot(2,2,2)
plot(r1,P1,'*'),xlabel('Drop Radius (nm)'),ylabel('Surface Pressure (Pa)')

```

### ***C.2.2 Function Program Code for Calculating Pressure***

```

%Function for calculating  $\Delta P$  saved in m-file format called "DeltaP.m".
function P=DeltaP(xr,xz)
global a2 Do A ro eps epso kappa Y1 Y2 C1 lambda1 Po sigma CapPi
D = Do + a2*1000-((a2*1000)^2-xr^2)^(1/2)+xz; % sphere-drop separation
if xr > a2*1000
D = 2*a2*1000; % restrains separation from infinity
end

% van der Waals surface pressure
Pvdw=-A/(6*3.14159)*(1/D^3-4*ro^6/D^9)*1e21;

% double-layer surface pressure for constant surface charge density
Pcc=1e6*eps*epso*kappa^2*(Y1+Y2)^2*exp(-kappa*D)*(1+exp(-2*kappa*D))/(1-exp(-2*kappa*D))^2;

Ph=C1/(2*3.14159*lambda1)*exp(-D/lambda1); % hydrophobic interaction, if needed for fitting
Pdrain=0; % hydrodynamic drainage can be included for high velocity approaches

CapPi=(Pvdw+Pcc+Ph+Pdrain)*1e6; % parallel plate surface pressure, [Pa]
P=Po-CapPi; % DeltaP =  $\Delta P$ , [Pa]

```

### ***C.2.3 Function Program Codes for Calculating 4<sup>th</sup> Order Runge-Kutta Estimators***

```

%Function for calculating  $k_0$ ,  $k_1$ ,  $k_2$ , or  $k_3$  saved in m-file format called "k.m".
function v=k(xphi,xr,xz)
global h sigma
v=-h*xr*cos(xphi)/(-(1e-6*xr*DeltaP(xr,xz)/sigma)+sin(xphi));

%Function for calculating  $l_0$ ,  $l_1$ ,  $l_2$ , or  $l_3$  saved in m-file format called "l.m".
function w=l(xphi,xr,xz)
global h sigma
w=-h*xr*sin(xphi)/(-(1e-6*xr*DeltaP(xr,xz)/sigma)+sin(xphi));

```

## APPENDIX D:

### VISUAL BASIC PROGRAM FOR CALCULATING DROP PROFILES DEFORMED BY A RIGID SPHERE

#### D.1 Drop Profiles and Force vs. Vertical Drop Deformation

The following program and subroutines were composed in the Visual Basic to be executed in a Microsoft Excel worksheet for calculating an oil-drop profile ( $r,z$ ) as deformed by an impinging microsphere (Chapter 5). The rudimentary program can calculate and print out a single interfacial profile for a given separation ( $D_{zero}$ ) as read from the spreadsheet, or automatically compute the net applied force as a function of the separation. The user may chose to run quick calculations base an initial estimate of the film drainage rate,  $dD/dt$ , or to iterate on each drop profile to find the exact relative approach velocity. The augmented Young-Laplace equation (Eq. 5.1) is solved using a 4<sup>th</sup> order Runge-Kutta technique as outlined in Appendix C. The total drop height, system radius of curvature at the drop apex, applied force at the apex, and normalized drainage rate are all printed by column to a worksheet.

#### D.2 Overview of Program and Subroutines

The main program *Profile* runs two large loops: one for the approach to closest separation from long range, the second after closest limiting approach has been attained and the film drains at constant separation with increasing film area. Each of these loops has two inner loops, one with and one without the angular parameterization of the augmented Young-Laplace equation (see Section C.2). The unparameterized routine works more efficiently in the near apaxial region where surface forces are strongest (Section D.2.3). The parameterized equations (Section D.2.4) are better when the slope of the interface becomes large ( $\gg 1$ ). The program actively reads previous and current data from the Excel worksheet by selecting cells at the appropriate time.

The initial drop geometry is defined by the pinned interline radius ( $R_{pin}$ ), the height ( $h_1$ ), and radius of curvature ( $a_1$ ) in a gravity field ( $g$ ). The internal drop pressure ( $P_o$ ) is assumed to be effectively constant as well as the drop volume. The pressure drop across the

interface in the Young-Laplace equation (Eq. 5.1) is computed in the subroutine *DeltaP* (Section D.2.2), including van der Waals (Pvdw), electrostatic double-layer (Pvv, Pcc, or Pcv), hydrophobic (Ph) and hydrodynamic (Pdrain) interfacial pressures. Interactions parameters are declared in the main program. Equations for constant surface potential, charge density (Eq. 5.5), or mixed boundary conditions (Eq. 6.1) are included for the Debye-Hückel limit. The Reynolds equation (Eq. 5.6) or that of Hartland (Eq. 6.2) may be chosen for inclusion, with the latter being much more computationally intensive. There is no user-interface for these options, so the code must be edited to comment out the undesired relations. Thus, there is some degree of familiarity required to run this program.

### ***D.2.1 Main Program Code***

```
Public a1, a2, Dzero, vel, eta, A, ro, eps, epso, kappa, Y1, Y2, C1, lambda1, Po, sigma, CapPi, h, h1, Reff,
Rinterf, InitVol As Double
Public CalcScheme
```

```
Sub Profile()
Dim I, P As Integer
Dim Default, VoidVol, Volume As Double
Dim Message, Title, Parametric
Message = "Clear data? Type 'yes' or 'no'."
Default = "no" ' Defaults to looping calculations for a row of Dzero values.
ClearData = InputBox(Message, Title, Default)
If ClearData = "yes" Then
  Sheets("Sheet1").Select
  Range("e5:j210").Select
  Selection.ClearContents
  Range("E2:e5").Select
  Selection.ClearContents
  Range("g2:h5").Select
  Selection.ClearContents
End If
Message = "Iteration or Quick Calculation? Type 'i' for iteration and 'q' for quick calculation."
Default = "q"
CalcScheme = InputBox(Message, Title, Default)

eps0 = 8.8542E-12 ' [sqC/(N-sqm)] permittivity of free space
eps = 78.54 ' dielectric constant
a1 = 5000 ' [um] radius of interface
h1 = 128.2 ' [nm] height of drop
Rpin = 1125000 ' [nm] pinned interline
Pinning = 1 ' 0 for pinned, 1 for slipping interline
InitVol = 3.14159 / 3 * (h1) ^ 2 * (3 * a1 - h1) ' Cap volume
a2 = 4 ' [um] radius of microsphere
A = 5E-21 ' Hamaker constant, [J]
```

```

ro = 0.16      ' universal atomic spacing, [nm]
Y1 = -35      ' droplet isolated surface potential, [mV]
Y2 = -16      ' sphere isolated surface potential, [mV]
conc = 0.007  ' ion concentration, [M]
kappa = (conc ^ 0.5) / 0.3043      ' Debye parameter, [1/nm]
vel = 40000   ' [nm/s] drainage velocity
eta = 0.001   ' [N-s/m^2] viscosity
C1 = 0        ' hydrophobic strength, [mN/m]
lambda1 = 3   ' hydrophobic decay length, [nm]
sigma = 8     ' interfacial tension, [mN/m]
Po = 2 * sigma * 1000 / a1      ' Laplace pressure, [Pa]
Reff = 1 / (1 / a1 + 1 / a2) ' approx. system radius of curvature, recalculate [um]
v = vel
Message = "Enter the separation to calculate drop profile; Return 0 for the entire S row:"
Default = 0   ' Default: looping calculations for a row of Dzero values.
Dzero = InputBox(Message, Title, Default) ' separation at apex, [nm]
Parametric = "no"
Message = "Start at line (2-??):"
Default = 2   ' Default: looping calculations for a row of Dzero values.
P = InputBox(Message, Title, Default)
If P < 2 Then
P = 2
End If
Cells(2, 7).Value = Reff
Cells(2, 10).Value = vel

If P > 2 And Dzero > 0 Then      ' Made for explicit single profile calculations
Parametric = "continue"
Cells(P, 4).Value = Dzero
Dzero = Cells(P, 4).Value
Cells(P - 1, 6).Select
Selection.Copy
Cells(P, 6).Select
ActiveSheet.Paste
Reff = 1 / (DeltaP(0, 0) / (2 * sigma * 1000) + 1 / a2)
Cells(P, 7).Value = Reff
Cells(P - 1, 9).Select
Selection.Copy
Cells(P, 9).Select
ActiveSheet.Paste
Elseif P = 2 Then
Cells(P, 9).Select
End If
If Dzero = 0 Then
Parametric = "yes"
Dzero = Cells(P, 4).Value
End If
If Parametric = "no" Then
TestOne = Dzero
Cells(P + 1, 4).Value = TestOne
Dzero = 10000
End If

```

```

If P > 2 Then      ' Starting after some calculations
  ContinueCalc = "yes"
  ZeroF = Cells(2, 8).Value * 1000000000 * a2
  Rpin = Rpin * (1 - Pinning * Cells(P - 1, 8).Value * 0.000000000001)
  Reff = Cells(P - 1, 7).Value
  Rinterf = 1 / (-1 / Reff + 1 / a2)      ' [um] interfacial radius of curvature
  If CalcScheme = "i" Then
    Cells(P, 5).Value = 2 * Cells(P - 1, 5).Value - Cells(P - 2, 5).Value
    Cells(P, 10).Value = 2 * Cells(P - 1, 10).Value - Cells(P - 2, 10).Value
    Cells(P, 10).Select
  End If
End If

*****Beginning of Major Loop
Do While Reff > 0 ' And I <= ntot And dl > 0
  *****This block calculates the steps in r for programmer-defined consistency
  rrun = Rpin
  rmin = 1
  ntot = 1000
  AFold = 0#
  AF = (rrun / rmin) ^ (1 / (ntot - 2))
  While Abs(AF - AFold) > 0.00000001
    AFold = AF
    AF = (1 + (rrun / rmin) * (AF - 1)) ^ (1 / (ntot - 1))
  Wend

  phi = 0          ' [radians] angle step by h
  r = 0            ' drop profile radius, [nm]
  z = 0            ' relative drop profile height/depth, [nm]
  y = 0            ' Slope at r = 0 is always flat, [unitless]
  dy = 0.000001 * DeltaP(r, z) / (2 * sigma)      ' [1/nm] curvature at apex
  VoidVol = 0
  Volume = 0
  CapPi = Po - DeltaP(r, z)
  Force = 0
  h = a2           ' step size for Runge-Kutta r, [nm]
  I = 1

  ***** 1st Loop starts here, calculates drop profile for inner radii.
  While y < 1 And Volume < InitVol      ' May need to vary routine to keep calculations down
    If r > a2 * 100 Then
      h = 5 * a2
    End If
    If r > a2 * 1000 Then
      h = 1000
    End If
    If r > a1 * 950 Then
      h = 50
    End If

    rold = r
    If Parametric = "continue" Or (Parametric = "no" And P = 3) Then

```

```

If I <= ntot Then
  h = (AF ^ (I - 1) - 1) / (AF - 1) * rmin - rold
End If
Cells(I + 1, 1).Value = r ' profile radius, [nm]
Cells(I + 1, 2).Value = z ' profile height, [nm]
Cells(I + 1, 3).Select
Cells(I + 1, 3).Value = 2 * sigma * 1000 / DeltaP(r, z) ' local radius of curvature
I = I + 1
End If

zold = z
CapPiOld = CapPi
Call RKN(r, z, y)
If z < zold Then ' For calculating Volume
  VoidVol = VoidVol + 3.14159 * ((r + rold) / 2000) ^ 2 * Abs(z - zold) / 1000
  zmin = z
End If
If r > 0 Then
  If zmin = zold Then ' Satisfied only once when zmin is reached
    Volume = 0 ' Resets Volume to zero at the zmin value
  End If
  If zold / z < 0 Then ' Satisfied when z goes from - to +
    Volume = Volume - VoidVol
  End If
End If
Volume = Volume + 3.14159 * ((r + rold) / 2000) ^ 2 * Abs(z - zold) / 1000
If r < a2 * 1000 Then
  Force = Force + (CapPi + CapPiOld) / 2 * 3.14159 * (r ^ 2 - rold ^ 2)
End If
CapPi = Po - DeltaP(r, z)
Wend

*****2nd Loop, Parameterized Young-Laplace begins here
h = 0.1 ' h = initial step size for phi, [radians]
phi = Atn(y) ' parameterization dz/dr=tan(phi)
While Volume < InitVol And r < Rpin
  If r > a1 * 999 Then
    h = 0.001
  End If
  If r > a1 * 999.9 Then
    h = 0.00001
  End If

  If Parametric = "no" And P = 3 Then
    Cells(I + 1, 1).Value = r ' profile radius, [nm]
    Cells(I + 1, 2).Value = z ' profile height, [nm]
    Cells(I + 1, 3).Select
    Cells(I + 1, 3).Value = 2 * sigma * 1000 / DeltaP(r, z) ' Radius of curvature, [um]
    I = I + 1
  End If

  rold = r

```

126

```
zold = z
CapPiOld = CapPi
Call RKS(phi, r, z)
Volume = Volume + 3.14159 * ((r + rold) / 2000) ^ 2 * Abs(z - zold) / 1000
If r < a2 * 1000 Then
  Force = Force + (CapPi + CapPiOld) / 2 * 3.14159 * (r ^ 2 - rold ^ 2)
End If
CapPi = Po - DeltaP(r, z)
Wend

If Parametric = "no" And P = 3 Then
Cells(I + 1, 1).Value = r ' profile radius, [nm]
Cells(I + 1, 2).Value = z ' profile height, [nm]
Cells(I + 1, 3).Select
Cells(I + 1, 3).Value = 2 * sigma * 1000 / DeltaP(r, z) ' Radius of curvature, [um]
I = I + 1
End If

zEnd = (z - zold) / (r - rold) * (Rpin - r) + z ' [nm]
Cells(P, 5).Value = zEnd 'Last value of z
Volume = Volume + 3.14159 * ((r + rold) / 2000) ^ 2 * zEnd
Cells(P, 8).Value = (Force - ZeroF) * 0.000000001 / a2 ' Force in [mN/m]
If P = 2 Then
  ZeroF = Force
  Cells(P, 8).Value = Force * 0.000000001 / a2 ' Force in [mN/m]
End If
*****Empirical adjustment for interline slipping
Rpin = 1125000 * (1 - Pinning * (Force - ZeroF) * 0.000000000001)

If Parametric = "no" And P = 3 Then
Cells(I + 1, 1).Value = Rpin ' profile radius, [nm]
Cells(I + 1, 2).Value = zEnd ' profile height, [nm]
Cells(I + 1, 3).Select
Cells(I + 1, 3).Value = 2 * sigma * 1000 / DeltaP(Rpin, zEnd) ' Radius of curvature, [um]
I = I + 1
End If

If P > 2 Then
If CalcScheme = "i" Then
*****Addition for velocity variable approach routine
Vold = Cells(P, 10).Value
Vnew = Cells(P, 9).Value
VError = (Vnew - Vold) / Vold
If VError = 1 Then
  Cells(P, 10).Value = Vnew
  Cells(P, 10).Select ' Iterative scalar for velocity
  P = P
Elseif Abs(VError) < 0.01 Then
If Vnew < 0 Then
  Vnew = 2 * Cells(P - 1, 9).Value - Cells(P - 2, 9).Value
End If
```

```

Cells(P, 6).Select
Selection.Copy
Cells(P + 1, 6).Select
ActiveSheet.Paste
Cells(P, 9).Select
Selection.Copy
Cells(P + 1, 9).Select
ActiveSheet.Paste
P = P + 1
Cells(P, 5).Value = 2 * Cells(P - 1, 5).Value - Cells(P - 2, 5).Value
Cells(P, 10).Value = 2 * Cells(P - 1, 9) - Cells(P - 2, 9).Value
Cells(P, 10).Select
Else
  If Vold < 0 Then
    Vold = -Vold
  End If
  If Vnew < 0 Then
    VError = 0.01 * Vold
  End If
  Cells(P, 10).Value = Vold * (1 + 0.02 * VError / Abs(VError))
  Cells(P, 10).Select
  P = P
End If
End If
If CalcScheme = "q" Then .....End of velocity variable approach routine
Cells(P - 1, 6).Select
Selection.Copy
Cells(P, 6).Select
ActiveSheet.Paste
Cells(P, 9).Select
Selection.Copy
Cells(P + 1, 9).Select
ActiveSheet.Paste
P = P + 1
End If .....End of constant velocity routine
Else
  P = P + 1
  Cells(P, 10).Value = Cells(P - 1, 9).Value
End If
Dzero = Cells(P, 4).Value
Rinterf = -2 * sigma * 1000 / DeltaP(0, 0)
Reff = 1 / (-1 / Rinterf + 1 / a2)
Cells(P, 7).Value = Reff
If Parametric = "no" Then
  If P = 4 Then ' Stops after calculating one profile for TestOne
    Reff = -1
  End If
End If
Loop

.....Sets up for compression curves at the limiting separation, Dzero
P = P - 2

```

128

```
Dzero = Cells(P, 4).Value
Reff = Cells(P, 7).Value
Cells(2, 6).Select ' Reset sheet to top
Sheets("Sheet2").Select
Range("d4:h500").Select
Selection.ClearContents
P = 2
d1 = 0.001 ' v scalar, some small, nonzero value at the apex
Cells(P, 9).Value = d1
Cells(P, 9).Select
rinit = 0
l = 1

*****Compression Loop Begins
Do While FofR < 5
phi = 0 ' New parameter steps by h
Cells(P, 4).Value = rinit ' point of film thickening, [nm]
r = rinit
z = -a2 * 1000 + ((a2 * 1000) ^ 2 - r ^ 2) ^ 0.5 ' [nm], indented sphere
y = -r / Sqr((a2 * 1000) ^ 2 - r ^ 2) ' slope at film edge [unitless]
dy = 0
VoidVol = 3.14159 / 3 * (z / 1000) ^ 2 * (3 * a2 - Abs(z) / 1000) ' spherical cap
Volume = 0
CapPi = Po + 2 * sigma * 1000 / (a2 + 0.001 * Dzero)
Force = CapPi * 3.14159 * r ^ 2
h = a2 ' [unitless] step size for Runge-Kutta r

rrun = Rpin
rmin = l
ntot = 1000
AFold = 0#
AF = (rrun / rmin) ^ (1 / (ntot - 2))
While Abs(AF - AFold) > 0.00000001
AFold = AF
AF = (1 + (rrun / rmin) * (AF - 1)) ^ (1 / (ntot - 1))
Wend

*****1st Loop start: calculates profile for inner radii.
While y < 1 And Volume < InitVol
If r > a2 * 100 Then
h = 5 * a2
End If
If r > a2 * 1000 Then
h = 1000
End If
If r > a1 * 950 Then
h = 50
End If

zold = z
rold = r
If rinit = 2000 Then
```

```

If I <= ntot Then
  h = (AF ^ (I - 1) - 1) / (AF - 1) * rmin - rold + rinit
Else
  Stop
End If
Cells(I + 1, 1).Value = r
Cells(I + 1, 2).Value = z
Cells(I + 1, 3).Select
Cells(I + 1, 3).Value = CapPi
I = I + 1
End If
CapPiOld = CapPi
Call RKN(r, z, y)
CapPi = Po - DeltaP(r, z)
If z < zold Then
  VoidVol = VoidVol + 3.14159 * ((r + rold) / 2000) ^ 2 * Abs(z - zold) / 1000
  zmin = z
End If

If r > 0 Then
  If zmin = zold Then
    Volume = 0
  End If
  If zold / z < 0 Then
    Volume = Volume - VoidVol
  End If
End If
Volume = Volume + 3.14159 * ((r + rold) / 2000) ^ 2 * Abs(z - zold) / 1000
If r < a2 * 1000 Then
  Force = Force + (CapPi + CapPiOld) / 2 * 3.14159 * (r ^ 2 - rold ^ 2)
End If
Wend

.....2nd Loop, Parameterized Young-Laplace begins here
h = 0.1
phi = Atn(y)
While Volume < InitVol
  If r > a1 * 999 Then
    h = 0.001
  End If
  If r > a1 * 999.9 Then
    h = 0.00001
  End If

  rold = r
  zold = z
  CapPiOld = CapPi
  Call RKS(phi, r, z)
  CapPi = Po - DeltaP(r, z)
  Volume = Volume + 3.14159 * ((r + rold) / 2000) ^ 2 * Abs(z - zold) / 1000
  If r < a2 * 1000 Then
    Force = Force + (CapPi + CapPiOld) / 2 * 3.14159 * (r ^ 2 - rold ^ 2)
  End If
End While

```

130

End If

Wend

```
zError = (InitVol - Volume) / (3.14159 * (r / 1000) ^ 2)
Cells(P, 5).Value = z + zError * 1000      'Last value of z, at pi/2
Volume = Volume + 3.14159 * ((r + rold) / 2000) ^ 2 * zError
FofR = Force * 0.000000001 / a2
Cells(P, 8).Value = Force * 0.000000001 / a2
If P = 2 Then
  Cells(3, 6).Select
  Selection.Copy
  Cells(P, 6).Select
  ActiveSheet.Paste
End If
If P > 2 Then
  Cells(P - 1, 6).Select
  Selection.Copy
  Cells(P, 6).Select
  ActiveSheet.Paste
  Cells(P - 1, 9).Select
  Cells(P, 9).Select
  ActiveSheet.Paste
End If
P = P + 1
rinit = rinit + 5 * a2
Cells(P - 1, 7).Value = Reff
If Parametric = "no" Then
  Reff = -1
End If
Loop
Cells(2, 6).Select
Sheets("Sheet1").Select
End Sub
```

### ***D.2.2 The Pressure Distribution***

```
Function DeltaP(xr, xz) As Double
Dim Pdrain, Pvdw, Ph, Pcc, CosAngC As Double
If xr > 10000000# Then
  Stop
Elseif xz > 10000000# Then
  Stop
End If
If xr >= a2 * 1000 Then
  If xr < 20000 Then      ' Approximate cantilever width
    D = a2 * 2000
    'D = 4000      '[nm] ~ minimum for bare cantilever tip
  Else
    D = 100000      ' 100 microns for the assembly hydrodynamic effects
  End If
```

```

Else
  Rise = ((a2 * 1000) ^ 2 - xr ^ 2) ^ (1 / 2) ' [nm]
  D = (Dzero + a2 * 1000 - Rise + xz) * a2 * 1000 / Rise ' [nm] Film thickness
End If
If D < Dzero Then
  D = Dzero
End If
*****Densities: n-hexadecane = 0.774, 1-bromohexadecane = 0.9991, cyclohexanol = 0.963
Pg = -9.81 * (0.998 - 0.774) * (1000 * h1 - xz) * 0.000000000001 ' [MPa] gravity
Pvdw = -A / (6 * 3.14159) * (1 / D ^ 3 - 4 * ro ^ 6 / D ^ 9) * 1E+21
'Pcc = 1000000 * 2 * eps * epso * kappa ^ 2 * ((Y1 ^ 2 + Y2 ^ 2) * Exp(-2 * kappa * D) + Y1 * Y2 *
(Exp(-kappa * D) + Exp(-3 * kappa * D))) / (1 - Exp(-2 * kappa * D)) ^ 2
'Pvv = 1000000 * 2 * eps * epso * kappa ^ 2 * (-(Y1 ^ 2 + Y2 ^ 2) * Exp(-2 * kappa * D) + Y1 * Y2 *
(Exp(-kappa * D) + Exp(-3 * kappa * D))) / (1 - Exp(-2 * kappa * D)) ^ 2
Pcv = 1000000 * 2 * eps * epso * kappa ^ 2 * ((Y1 ^ 2 - Y2 ^ 2) * Exp(-2 * kappa * D) + Y1 * Y2 *
(Exp(-kappa * D) - Exp(-3 * kappa * D))) / (1 + Exp(-2 * kappa * D)) ^ 2
Ph = C1 / (2 * 3.14159 * lambda1) * Exp(-D / lambda1)

If CalcScheme = "i" Then
  d1 = ActiveCell.Value
  v = d1 * vel
Else
  v = vel
End If

*****Hartland's equation implemented: Dgap film thickness from Chan & White
Dgap = ((a2 + (Dzero + xz) / 1000) ^ 2 + (xr / 1000) ^ 2) ^ (1 / 2) - a2 ' [um]
If Reff > a2 And xr < a2 * 1000 And Dgap < 10 Then 'Constraint
  Gaplimit = 4 * Dzero / 1000 'Film extent
  CosAngC = ((Rinterf - a2 - Dzero / 1000) ^ 2 + Rinterf ^ 2 - (a2 + Gaplimit) ^ 2) / (2 * (Rinterf - a2 -
Dzero / 1000) * Rinterf)
  AngC = Atn(-CosAngC / Sqr(1 - CosAngC ^ 2)) + 2 * Atn(1) 'Angle swept by Rinterf
  ChordS = Rinterf * Sin(AngC) / Sin((3.14159 - AngC) / 2) ' Chord length from Dzero to GapLimit
  CosPhiC = ((a2 + Gaplimit) ^ 2 + (a2 + Dzero / 1000) ^ 2 - ChordS ^ 2) / (2 * (a2 + Gaplimit) * (a2 +
Dzero / 1000))

  CosAngC = ((Rinterf - a2 - Dzero / 1000) ^ 2 + Rinterf ^ 2 - (a2 + Dgap) ^ 2) / (2 * (Rinterf - a2 - Dzero /
1000) * Rinterf)
  If CosAngC > 1 Then
    CosAngC = 1
  ElseIf CosAngC < 0 Then
    CosAngC = 0
  End If
  If CosAngC = 1 Then
    AngC = 0
  Else
    AngC = Atn(-CosAngC / Sqr(1 - CosAngC ^ 2)) + 2 * Atn(1) 'Arc cosine = Angle swept by
Rinterf
  End If
  ChordS = Rinterf * Sin(AngC) / Sin((3.14159 - AngC) / 2) ' Chord length from Dzero to GapLimit
  CosPhiH = ((a2 + Dgap) ^ 2 + (a2 + Dzero / 1000) ^ 2 - ChordS ^ 2) / (2 * (a2 + Dgap) * (a2 + Dzero /
1000))

```

132

```
If CosPhiH < CosPhiC Then
  CosPhiH = CosPhiC
End If
Pdrain = 12 * eta * v * a2 ^ 2 / D ^ 3 * Log((1 + CosPhiH) / (1 + CosPhiC)) / Log(10)
Else
  Pdrain = 3 * eta * v * a2 * 0.001 / (D ^ 2) 'Reynolds drainage [MPa] Reff ~ a2
End If
CapPi = (Pg + Pvdw + Pcv + Ph + Pdrain) * 1000000 ' surface pressure [Pa]
'CapPi = (Pg + Pvdw + Pcc + Ph + Pdrain) * 1000000 ' surface pressure [Pa]
'CapPi = (Pg + Pvdw + Pvv + Ph + Pdrain) * 1000000 ' surface pressure [Pa]
DeltaP = Po - CapPi '[Pa]
End Function
```

### ***D.2.3 Subroutines for 4<sup>th</sup>-Order Runge-Kutta Procedure***

#### ***Runge-Kutta Procedure***

```
Sub RKN(r, z, y)
  zold = z
  yold = y
  rpass = r
  zpass = z
  ypass = y
  ko = h * ypass
  lo = h * g(rpass, zpass, ypass)
  rpass = r + h / 2
  zpass = z + ko / 2
  ypass = y + lo / 2
  k1 = h * ypass
  l1 = h * g(rpass, zpass, ypass)
  rpass = r + h / 2
  zpass = z + k1 / 2
  ypass = y + l1 / 2
  k2 = h * ypass
  l2 = h * g(rpass, zpass, ypass)
  rpass = r + h
  zpass = z + k2
  ypass = y + l2
  k3 = h * ypass
  l3 = h * g(rpass, zpass, ypass)
  z = zold + (ko + 2 * k1 + 2 * k2 + k3) / 6
  y = yold + (lo + 2 * l1 + 2 * l2 + l3) / 6
  r = rpass
End Sub
```

#### ***Function for Augmented Young-Laplace Equation***

Function g(xr, xz, xy) As Double

```

If xr = 0 Then
  g = 0.000001 * DeltaP(xr, xz) / (2 * sigma)
Else
  g = (0.000001 * DeltaP(xr, xz) / sigma) * (1 + xy ^ 2) ^ (3 / 2) - xy * (1 + xy ^ 2) / xr
End If
End Function

```

#### ***D.2.4 Subroutines for Parameterized Young-Laplace Equation***

##### ***Runge-Kutta Procedure***

```

Sub RKS(phi, r, z)
  rold = r
  zold = z
  phipass = phi
  rpass = r
  zpass = z
  ko = k(phipass, rpass, zpass)
  lo = l(phipass, rpass, zpass)
  phipass = phi + h / 2
  rpass = r + ko / 2
  zpass = z + lo / 2
  k1 = k(phipass, rpass, zpass)
  l1 = l(phipass, rpass, zpass)
  phipass = phi + h / 2
  rpass = r + k1 / 2
  zpass = z + l1 / 2
  k2 = k(phipass, rpass, zpass)
  l2 = l(phipass, rpass, zpass)
  phipass = phi + h
  rpass = r + k2
  zpass = z + l2
  k3 = k(phipass, rpass, zpass)
  l3 = l(phipass, rpass, zpass)
  r = rold + (ko + 2 * k1 + 2 * k2 + k3) / 6
  z = zold + (lo + 2 * l1 + 2 * l2 + l3) / 6
  phi = phipass
End Sub

```

##### ***Functions for Parameterized Young-Laplace Equations***

```

Function l(xphi, xr, xz) As Double
  If xr = 0 Then
    l = 1000000 * h * sigma * Sin(xphi) / DeltaP(xr, xz)
  Else
    l = -h * xr * Sin(xphi) / (-0.000001 * xr * DeltaP(xr, xz) / sigma + Sin(xphi))
  End If
End Function

```

134

**Function k(xphi, xr, xz) As Double**

**If xr = 0 Then**

**k = 1000000 \* h \* sigma \* Cos(xphi) / DeltaP(xr, xz)**

**Else**

**k = -h \* xr \* Cos(xphi) / (-(0.000001 \* xr \* DeltaP(xr, xz) / sigma) + Sin(xphi))**

**End If**

**End Function**

**VITA**

**Name:** David Eric Aston

**Date of Birth:** December 6, 1972

**Place of Birth:** San Angelo, TX

**Education:** Ph.D. in Chemical Engineering, University of Washington, June 2001

M.S. in Physics, University of Washington, August 2000

B.S. in Chemical Engineering, University of Idaho, May 1995

**Publications:**

Aston, D. E.; Berg, J. C. "Thin-Film Hydrodynamics in Fluid Interface-Atomic Force Microscopy." *Ind. Eng. Chem. Res.* (submitted Feb. 2001).

Aston, D. E.; Berg, J. C. "Quantitative Analysis of Fluid Interface-Atomic Force Microscopy." *J. Colloid Interface Sci.* **235**(1): 162-69 (2001).

He, M.; Szuchmacher-Blum, A.; Aston, D. E.; Buenviaje, C.; Overney, R. M.; Luginbühl, R. "Critical Phenomena of Water Bridges in Nanoasperity Contacts." *J. Chem. Phys.* **114**(3): 1355-60 (2001).

Aston, D. E.; Berg, J. C. "Long-Range Attraction between Silanated Silica Materials Studied by an Electrolyte Titration with Atomic Force Microscopy." *Colloids and Surfaces A* **163**(2-3): 247-63 (2000).

Irvine, J. A.; Aston, D. E.; Berg, J. C. "The Use of Atomic Force Microscopy (AFM) to Measure the Adhesive Properties of Sized and Unsized Papers." *Tappi J.* **82**(5): 172-74 (1999).

Aston, D. E.; Berg, J. C. "Fluid Interfacial Separations for Secondary Fiber Recovery as Probed with Atomic Force Microscopy." *J. Pulp Paper Sci.* **24**(4): 121-25 (1998).

Snyder, B. A.; Aston, D. E.; Berg, J. C. "Particle-Drop Interactions Measured with Atomic Force Microscopy." *Langmuir* **13**(3): 590-93 (1997).